

**Synthesis and Characterization of $\text{Li}_7\text{La}_3\text{Zr}_2\text{O}_{12}$ Thin Films
for Solid-State Lithium Ion Batteries**

A thesis submitted to attain the degree of
DOCTOR OF SCIENCES of ETH ZURICH

(Dr. sc. ETH Zurich)

Presented by

MICHAEL JAE-SEUNG RAWLENCE

MSc Nanoscience, University of Nottingham
BSc Chemistry and Molecular Physics, University of Nottingham

Born on 02.02.1989

Citizen of
United Kingdom

Accepted on the recommendation of:

Prof. Dr. J. L. M. Rupp, examiner
Dr. Stephan Buecheler, co-examiner
Prof. Dr. V. Wood, co-examiner
Prof. Dr. W. Jaegermann, co-examiner

Acknowledgements

First of all, I would like to thank both of my supervisors Prof. Dr. Jennifer Rupp and Dr. Stephan Buecheler who have given me the opportunity to pursue my doctoral research in both of their groups. I am particularly privileged to have both patient and understanding supervisors who have guided me through the often challenging work which has helped me mature as a scientist and broaden my horizons.

I thank Prof. Dr. Wolfram Jaegermann from the Technische Universität Darmstadt, and Prof. Vanessa Wood from the ETH Zürich department of Nanoelectronics for being the co-examiners of this thesis and for carefully reading the manuscript.

Prof. Corsin Battaglia from the Laboratory Materials for Energy Conversion is acknowledged for providing access to many of their facilities, particularly the high temperature stage for XRD measurements, which was crucial to the research. Thanks also to Dr. Arndt Remhof and Dr. Eduardo Cuervo-Reyes who always took the time for scientific discussions with many fruitful outcomes.

During this time I have worked with many exceptional people and would like to warmly thank my colleagues Nico Filippin and Inigo Garbayo for their great contributions to this body of work. To my fellow PhD student Reto Pfenninger, I am grateful for all the support, the shared journey and all the great and terrible jokes. Also from the Electrochemical Materials group a shout out to Michal Stružik, Yanuo Shi, Semih Afyon, Markus Kubicek, and the other members of the group who helped create a great team spirit, which played a pivotal role in the first year of the project.

To all my colleagues at the Laboratory for Thin Films and Photovoltaics, I thank you all for the years spent together with many good times in and out of the laboratory. To Timo Jaegar and Benjamin Bissig who taught me to use the Orion. To Harald Hagendorfer and Alexander Uhl for their kindness and generosity. To Georgi Bodurov, Christian Andres, Lukas Greuter and Lukas Zortea for helping blow off some steam. To Christina Gretener and Martina Lingg for all the delicious cakes. To Julian Perrenoud, Thomas Feurer, Aneliia Wäckerlin, Romain Carron, Stefan Hass, Enrico Avancini, Johannes Löckinger, Kostia Kravchyk, Benjamin Kunz, Ruben Roldan-Molinero and Tzu-Ying Lin for their great help with laboratory work and scientific discussions. And finally to group leaders Romanyuk Yaroslav and Prof. Ayodhya Tiwari, and to all other lab members another huge thank you for the inspiring and enjoyable atmosphere which was upheld at all times.

Finally, a heartfelt thanks to my friends particularly Eman, Mike and Hunki for the de-stressing “Man Holidays”, my dear wife Gloria, and family, in England, in Switzerland and around the world without who’s support I would not have managed to get this far.

Zurich, 2017

Preface

This dissertation comprises a summary based on the following papers, which are referred to in the text:

1. Rawlence, M.; Garbayo, I.; Buecheler S.; Rupp, J.L.M.,
“On the chemical stability of post-lithiated garnet Al-stabilized $\text{Li}_7\text{La}_3\text{Zr}_2\text{O}_{12}$ solid-state electrolyte thin film”,
Nanoscale, **8**, 14746-14753 (2016) DOI: [10.1039/c6nr04162k](https://doi.org/10.1039/c6nr04162k)
2. Rawlence, M.; Filippin, A. N.; Wäckerlin, A.; Ling, T.-Y.; Cuervo-Reyes, E.; Remhof, A.; Battaglia, C.; Rupp, J.L.M., Buecheler S.
“The Effect of Gallium Substitution on Lithium Ion Conductivity and Phase Evolution in Sputtered $\text{Li}_{7-3x}\text{Ga}_x\text{La}_3\text{Zr}_2\text{O}_{12}$ Thin Films”,
ACS Applied Materials & Interfaces, **10**, (16), 13720-13728 (2018)
DOI: [10.1021/acsami.8b03163](https://doi.org/10.1021/acsami.8b03163)
3. Filippin, A. N.‡; Rawlence, M.‡; Wäckerlin, A.; Feurer, T.; Zünd, T.; Kravchyk, K.; Kovalenko, M. V.; Romanyuk, Y. E.; Tiwari, A. N.; Buecheler S.,
“Chromium nitride as a stable cathode current collector for all-solid-state thin film Li-ion batteries”
RSC Advances, **7**, 26960-26967 (2016) DOI: [10.1039/c7ra03580b](https://doi.org/10.1039/c7ra03580b)

‡ signifies co-first author

Summary

The realization of a high performance thin film solid-state battery relies on the development of a suitable solid-state electrolyte with high lithium ion conductivity. Such batteries are able to overcome many of the limitations associated with their liquid electrolyte counterparts, enabling batteries with better energy densities, higher voltages and reduced risk of combustion.

Since the development of several new candidates for solid electrolytes in the last decade, research into realizing the potential of solid-state batteries has increased dramatically. The ceramic garnet $\text{Li}_7\text{La}_3\text{Zr}_2\text{O}_{12}$ has been proposed as a good solid-state electrolyte candidate with a high reported ionic conductivity and good electrochemical and mechanical stability. Recent research has been focused largely on bulk electrolyte materials, often in the form of pellets on which electrode materials are deposited. However, being able to produce $\text{Li}_7\text{La}_3\text{Zr}_2\text{O}_{12}$ in thin film form is widely regarded as the most promising approach for increasing energy density of the resulting cells. In this context, the work presented here investigates methods for forming thin films of $\text{Li}_7\text{La}_3\text{Zr}_2\text{O}_{12}$ with a detailed analysis of the resulting structural and electrochemical properties.

In the first chapter of this thesis, an overview on solid-state batteries and their materials is given through the *General Introduction*. Here, the underlying concepts of battery operation are explained and the advantages of moving to solid-state systems are given, as well as a brief summary of the properties of $\text{Li}_7\text{La}_3\text{Zr}_2\text{O}_{12}$.

In the second and third chapters the reader is introduced to investigations on pulsed laser deposited, and sputtered thin films of $\text{Li}_7\text{La}_3\text{Zr}_2\text{O}_{12}$ with a focus on forming the desired, cubic phase with high lithium ion conductivity. First, a study on the effect of film thickness during a lithium enrichment-annealing step was undertaken to understand how the degree of lithiation can affect the film structure, and how lithium loss during this process can be circumvented.

The influence of annealing temperature and time on phase formation in thin films with various levels of lithium and gallium is discussed, particularly from the point of view of X-ray diffraction. X-ray Photoelectron Spectroscopy furthers the understanding of how the chemical environments of the gallium change with respect to the resulting phase formation. Importantly, the chemical and structural analysis is always related back to the lithium ion conductivity to understand how these films would perform in a cell.

When building a thin film cell with a planar configuration, each layer must survive all subsequent processing steps. Due to the high processing temperatures of many electrode and electrolyte materials, above 600°C, the bottom current collector must have exceptional corrosion resistance in the presence of both lithium and oxygen contained in the electrode. In another study, Cr_xN was explored as a possible bottom current collector for the cathode. Thin films were deposited and characterized then half-cells using thin film $\text{LiMn}_{1.5}\text{Ni}_{0.5}\text{O}_4$ and a liquid electrolyte were constructed to determine the effectiveness of the layer during cycling.

We were able to demonstrate excellent corrosion resistance at high temperature and subsequent successful cycling of the cell.

This work constitutes important progress towards the development of solid-state batteries with high energy density and safety. Such devices will be of high importance in the fast developing industries of “Internet of Things” (IoT), drones and space technology among others.

Zusammenfassung

Die Realisierung von Hochleistungsfestkörperbatterien bedingt die Entwicklung eines passenden Festkörperelektrolyts mit hoher ionischer Leitfähigkeit. Im Gegensatz zu herkömmlichen Flüssigelektrolytbatterien sind solche Batterien in der Lage viele Limitierungen wie hohe Energiedichte, hohe Spannungen sowie Explosionsgefahr zu überwinden.

Seit der Entwicklung von mehreren neuen Materialien für Festkörperelektrolyte im letzten Jahrzehnt hat sich die Forschung bezüglich der Realisierung von Festkörperbatterien stark intensiviert. Der keramische Granat $\text{Li}_7\text{La}_3\text{Zr}_2\text{O}_{12}$ gilt als guter Kandidat für ein Festkörperelektrolyt mit hoher ionischer Leitfähigkeit sowie guter elektrochemischer und mechanischer Stabilität. Kürzlich hat sich die Forschung grösstenteils auf Elektrolyten in Form von Pellets, auf welche Elektrodenmaterialien abgeschieden werden, fokussiert. Um jedoch die Energiedichte der resultierenden Zellen zu erhöhen, gilt $\text{Li}_7\text{La}_3\text{Zr}_2\text{O}_{12}$ in Form eines Dünnsfilms als vielversprechendster Kandidat. In diesem Kontext untersucht diese Arbeit Methoden für die Herstellung von Dünnschichten aus $\text{Li}_7\text{La}_3\text{Zr}_2\text{O}_{12}$ sowie einer detaillierten Analyse der resultierenden strukturellen und elektrochemischen Eigenschaften.

Im ersten Kapitel der Dissertation *General Introduction* wird ein Überblick über Festkörperbatterien und dessen Materialien gegeben. Hier werden die grundlegenden Konzepte des Betriebs von Batterien erklärt und die Vorteile des Übergangs zu Festkörperbatterien sowie eine kurze Zusammenfassung der Materialeigenschaften von $\text{Li}_7\text{La}_3\text{Zr}_2\text{O}_{12}$ präsentiert.

Im zweiten und dritten Kapitel wird der Leser in die Untersuchung von $\text{Li}_7\text{La}_3\text{Zr}_2\text{O}_{12}$ Dünnschichten, hergestellt durch gepulste Laserabscheidung sowie Magnetronspitzen, eingeführt, wobei der Fokus auf der Herstellung der kubischen Phase mit hoher ionischer Leitfähigkeit liegt. Zunächst wurde eine Studie zur Lithiumanreicherung nach Schichtwachstum durchgeführt, um zu verstehen wie der Lithiumanteil die Schichtstruktur beeinflusst und wie der Verlust von Lithium während des Prozesses umgangen werden kann.

Der Einfluss der Prozesstemperatur und -zeit auf die Phasenbildung in Dünnschichten mit verschiedenem Lithium- und Galliumanteilen wird im dritten Kapitel diskutiert. Röntgenphotoelektronenspektroskopie zeigt, wie sich die chemische Umgebung von Gallium mit Hinblick auf die Phasenformung ändert. Von hoher Bedeutung ist vor allem die Korrelation der chemischen und strukturellen Analyse mit der ionischen Leitfähigkeit, um zu verstehen wie diese Filme in einer Zelle funktionieren.

Wird eine Dünnschichtzelle in planarer Konfiguration gebaut, muss jede Schicht jegliche darauffolgenden Prozessschritte überstehen. Da viel vielversprechende Elektroden- und Elektrolytmaterialien hohen Prozesstemperaturen bedingen, welche über 600°C liegen können, muss der untere Stromkollektor eine ausgezeichnete Korrosionsbeständigkeit gegenüber dem in den Elektroden enthaltenen Lithium und Sauerstoff vorweisen. In einer anderen Studie wurde Cr_xN als möglicher Stromsammler für die Kathode untersucht. Zunächst wurden Cr_xN Schichten abgeschieden und charakterisiert, und anschließend in Kombination mit $\text{LiMn}_{1.5}\text{Ni}_{0.5}\text{O}_4$ Kathoden und einem flüssig Elektrolyt in Halbzellen getestet. Wir waren in

der Lage eine exzellente Korrosionsbeständigkeit bei hohen Temperaturen und mehrfachen erfolgreichen Zyklen der Zelle zu demonstrieren.

Diese Arbeit stellt einen wichtigen Fortschritt mit Hinblick auf die Entwicklung von Festkörperbatterien mit hoher Energiedichte und Sicherheit dar. Solche Bauteile werden unter anderem in sich schnell entwickelnden Anwendungsbereichen wie „Internet of Things“ (IoT), Dronen und Raumfahrttechnik von grosser Bedeutung sein.

Table of Contents

Acknowledgements	i
Preface	ii
Summary.....	iv
Zusammenfassung	vi
Table of Contents	vi
1 General Introduction	10
1.1 Short history of the battery	10
1.2 Technological Relevance.....	10
1.3 Working principles of the battery	11
1.4 Solid-state Batteries	12
1.5 The $\text{Li}_7\text{La}_3\text{Zr}_2\text{O}_{12}$ Ceramic Electrolyte.....	17
1.6 Thin Film Processing of $\text{Li}_7\text{La}_3\text{Zr}_2\text{O}_{12}$	19
1.7 Aims of the thesis	20
2 On the Chemical Stability of Post-Lithiated Garnet Al-Stabilized LLZO Solid-state Electrolyte Thin Films	22
2.1 Introduction	22
2.2 Experimental.....	22
2.3 Results and Discussion	24
2.4 Conclusion.....	30
3 The Effect of Gallium Substitution on Lithium Ion Conductivity and Phase Evolution in Sputtered $\text{Li}_{7-3x}\text{La}_3\text{Zr}_2\text{Ga}_x\text{O}_{12}$ Thin Films	32
3.1 Introduction	32
3.2 Experimental.....	32
3.3 Results and Discussion	35
3.4 Conclusion.....	52
4 Chromium Nitride as Stable Cathode Current Collector for All-solid-state Thin Film Li^+ ion Batteries	53
4.1 Introduction	53
4.2 Experimental.....	53
4.3 Results and Discussion	55
4.4 Conclusion.....	74
4.5 Personal Contribution.....	75

5	Summary and Outlook	76
5.1	General Conclusion	76
5.2	Outlook	77
6	References	79
7	Appendix	89
7.1	Chapter 3 Supporting Information.....	89
7.2	Chapter 4 Supporting Information.....	92
7.3	Financial Support.....	94
7.4	List of Figures.....	94
7.5	List of Tables.....	98
7.6	Nomenclature	98
7.7	Publications	100
7.8	Patents.....	100
7.9	Conference Contributions.....	101

1 General Introduction

1.1 Short history of the battery

The first battery was invented in the year 1799 by Alessandro Volta.¹ Known as the voltaic pile, it consisted of a stack of alternating metal plates of copper and zinc separated by cardboard or felt spacers soaked in a salt water electrolyte. The chemical potential between the two metals was powerful enough to cause an electrical current to flow when connecting wires to each end of the stack. This invention sparked a wave of discovery an innovation which eventually led human beings to master one of the cornerstones of modern day society, electricity.

Through carefully study of the stable flow of electrons generated by batteries, scientists such as André-Marie Ampère, Michael Faraday and James Clerk Maxwell could begin to understand the basic principles of electromagnetism. Continued improvements to battery efficiency and energy capacity led to mainstream adoption of electricity for powering telegraph communication and electroplating metals. By exploring the potential of new materials for storing energy the first rechargeable battery was invented by Gaston Planté, 60 years after the voltaic pile. The Planté battery was based on a lead-acid system, and after some fine tuning of the design demonstrated stable performance over many cycles. Lead-acid batteries are still one of the most widespread types of battery today due to their durability, reliability and lifetime.

By exploring more and more material systems, advancements in performance continued to be made. The nickel-cadmium battery came about at the end of the 1800s and was stable at high and low states of charge for longer periods of time as well as having larger capacities. Other alkaline batteries utilizing the same potassium hydroxide electrolyte but changing the electrodes led to further improvements through the 1900s. More recently, nickel metal hydride batteries were introduced with improved capacity at high current. Finally, in the 1970s the lithium ion battery was developed with far superior energy density and lifetimes than their predecessors. Li chemistry has several fundamental advantages over other types for the following reasons: Li has the lowest reduction potential of any element meaning that higher voltages can be achieved between the electrodes. It is also one of the lightest elements and has a small ionic radius meaning energy density of Li containing materials is high. In conjunction with these properties, the single charge of the Li^+ ion gives it a relatively high mobility through crystal structures vs. other multivalent or larger ions such as Na^+ , Mg^{2+} and Al^{3+} which can also be used in batteries.

1.2 Technological Relevance

The demand for Li^+ ion batteries has been accelerated in the last few years due to the mass availability of cheaper and more powerful electronic devices such as smartphones, laptops and other electronic gadgets. Moreover, the fast-growing market of Li^+ ion batteries is expected to expand even further owing to the introduction of fully electric vehicles, reaching a predicted market of more than 50 billion USD by 2018.² This growth has been accompanied by a strong

increase in research and development in the field, aiming for higher energy densities and faster charge rates.

1.3 Working principles of the battery

A battery cell contains three main components, positive and negative electrodes, also called the cathode and anode, and an electrolyte between them as depicted in Fig. 1.1. An inherent electrochemical potential exists between the electrode materials, which produces an electromotive force, namely the cell voltage, pulling positive ions from the anode to the cathode through the electrolyte. The electrolyte is composed of lithium salts typically LiPF_6 dissolved in organic solvents of ethylene carbonate and dimethyl carbonate. This liquid is conductive to lithium ions, but insulates against electrons, therefore, as the lithium ions travel through the cell the electrons cannot follow resulting in a charge imbalance. In order to restore neutral charge distribution the electrons are forced to travel to the other side through the external circuit, doing work along the way. By inserting a separator into the electrolyte region the cathode and anode are prevented from touching, preventing a short-circuit. If the external circuit is not closed there is no other way for the electrons to travel to the cathode, a capacitive charge quickly accumulates which blocks the influence of the voltage and prevents battery discharge. On the other hand, when an alternative route is provided through an external circuit there is no build-up of charge and a free-flowing current is released until all the available ions have migrated to the cathode or there is no capacity for more ions.

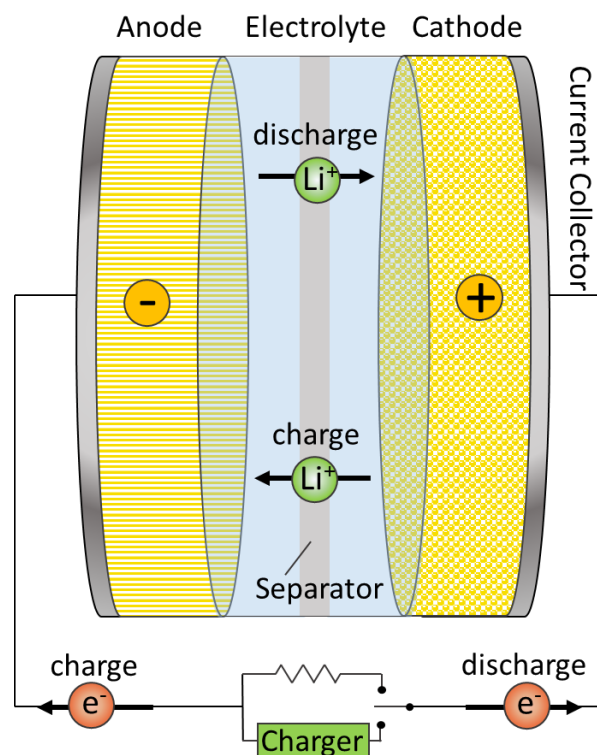


Fig. 1.1 Schematic of a typical battery with liquid electrolyte

For this process to work smoothly the transport of ions through the three main components, and the interfaces between them, is of critical importance. Electrons must also be extracted and reinserted efficiently through current collectors so they can recombine with the

Li^+ ions as they enter the electrode and preserve the neutral charge distribution of the system. The electrolyte/separator component must have the properties of being highly conductive for lithium ions, highly resistive for electrons and chemically stable in contact with the anode and cathode during operation over the full voltage range, and over long periods of inactivity.

The typical ionic conductivity of liquid electrolytes is around $10^{-2} \text{ S cm}^{-1}$ which is high enough to have a negligible influence on the total resistance of the system.³ The limiting factors to performance are often due to chemical instabilities at the solid-electrolyte interface on the cathode or anode surfaces. Although such a layer is often required to increase the stability of the system,⁴ the gradual build-up of insulating species at this surface reduces the performance of the battery by preventing the extraction of the available lithium and lowering the current. The liquid electrolytes are typically flammable, reacting when exposed to air at high temperatures. They are also susceptible to low temperatures where freezing can occur, damaging the separation layer and possibly leading to a short circuit.⁵ The requirements for robust, leak-proof packaging as a countermeasure for these issues increases the battery weight significantly. Other limitations relating to the liquid organic electrolyte are the limited electrochemical stability, preventing their use with lithium metal and high voltage cathodes.⁶ For these reasons conventional Li^+ ion technology relying on a liquid electrolyte seem to be reaching a technological limit, but there is still plenty of room for improvement in the emerging field of lithium-based solid-state batteries.⁷

1.4 Solid-state Batteries

By replacing the liquid electrolyte with a solid ionic conductor, several issues around the performance and safety of lithium ion batteries can be circumvented.⁸⁻¹⁰ The most obvious advantage is the removal of flammable and liquid substances which removes the tight restrictions on temperature, allows lighter packaging to be used, and dramatically increases the safety. Solid-state batteries can potentially offer a longer lifetime, higher charge/discharge rates, higher output voltage and higher energy density by implementing a suitable combination of materials and 3D (micro)architectures.¹⁰ Furthermore, all-solid-state batteries can be miniaturized for implementation in micro-devices and even made flexible, thus expanding their functionality.¹⁰⁻¹³ One example of the current state-of-the-art for solid-state batteries is shown in work by Wang et. al. using a LiPON electrolyte with Li metal.¹⁴

The solid-state battery was first conceived of in the 1960s when certain ionic conductors were identified, however the ionic conductivities of the first candidates for a solid electrolyte were too low to produce a battery with reasonable performance. A cell with basic planar geometry is shown in Fig. 1.2 which would be achieved through thin film sequential deposition of each component. The high energy density and flexibility of design of this approach would be well suited for microelectronic devices,¹⁵ solid-state electrolytes to be integrated into bulk batteries would have a larger capacity but use a composite electrode composition with lower energy density.¹⁶

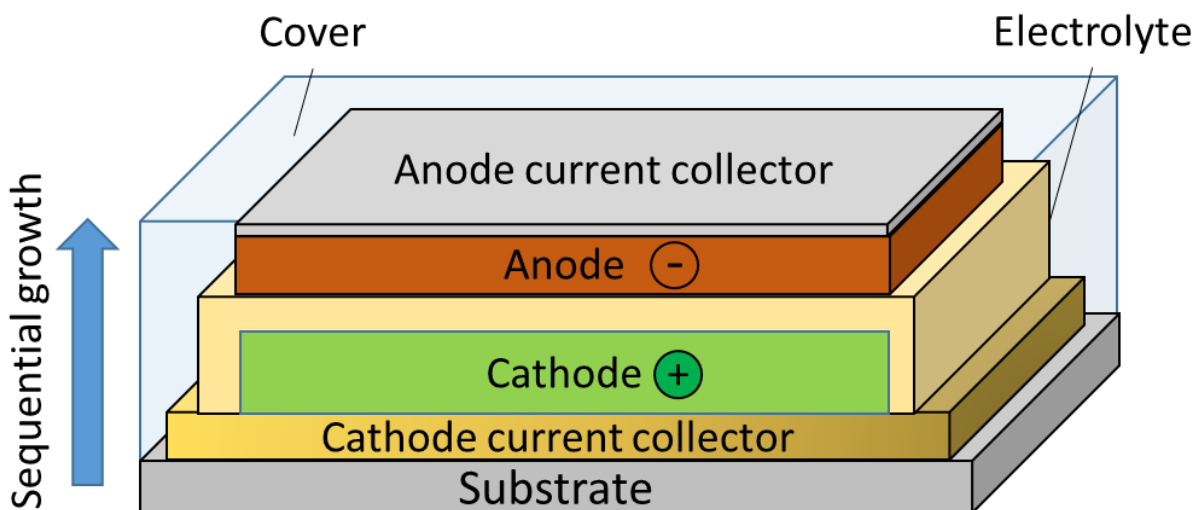


Fig. 1.2 Schematic of an all-solid-state thin film cell with planar geometry

Each component of the cell must fulfill certain requirements. Starting from the substrate, which can be composed of a wide range of materials, it must have a high chemical stability and be able to withstand the high processing temperatures required for the preparation of the thin film battery of up to 600-700°C.¹⁷⁻¹⁹ It should also be suitably flat so that uniform thin films can be deposited onto it without the emergence of pinholes. For commercial purposes it should ideally be lightweight and cheap. In the research of thin film batteries some examples of substrates which have been used are Si wafers, stainless steel and MgO.

Next, the cathode current collector must also withstand high processing temperatures. Therefore, aluminum, which is the first choice as cathode current collector in conventional liquid Li^+ ion cells, is not suitable because of its relatively low melting point of 660 °C and the formation of LiAlO_2 at temperatures as low as 450 °C, which is an electrical insulator.²⁰ Other alternatives like tungsten, nickel, chromium and several stainless steels have been investigated for this purpose, but either react in the potential range of 4-4.5 V vs. Li^+/Li or oxidize below 600 °C.²¹⁻²⁴ Standard stainless steel (grade 304) contains both Cr and Fe which can diffuse into the cathode when annealed at 600 °C or above even for short annealing times of 1 hour, degrading the overall cell performance.²⁵ Noble metals such as gold and platinum also alloy with lithium and have a prohibitive cost for use in mass produced batteries.^{26,27} TiN has been proposed as current collector for Li^+ ion microbatteries²⁸ although it shows poor stability in air at temperatures of 600°C and above,²⁹ and TiO_2 is vulnerable to reactions with lithium resulting in the formation of $\text{Li}_4\text{Ti}_5\text{O}_{12}$.³⁰

On the other hand, Cr_2N has good mechanical properties and high thermal stability in vacuum up to 1120°C .³¹⁻³³ Furthermore, reaction with lithium is only observed at temperatures above 850°C for long reaction times, while the oxidation of Cr_2N begins in the range 650°C - 700°C in air.³⁴⁻³⁶ It has so far not been investigated as a current collector despite its promising characteristics such as electrical conductivity which is around 10 times higher than CrN .

Improvements in battery performance have been mostly oriented around the development of electrode materials with higher rate capabilities, voltages, capacities and lifetimes. The commercially successful cathodes are all based on transition metal oxides in various crystal structures which intercalate Li^+ ions through 1D, 2D or 3D channels in the structure. These channels form due to presence of closely positioned lithium sites in the lattice which have a low activation energy between them. The known structures which have efficient intercalation properties are layered, spinel, olivine and tavorite. Examples of well-known cathodes with these structures are shown in Fig. 1.3 from work by Islam et. al.³⁷ Currently LiCoO_2 is the most widespread due to its good balance of high voltage (average 3.8 V) and capacity ($\sim 148 \text{ mAh g}^{-1}$)³⁸. However, due to unprecedented increases in demand for Li^+ ion batteries, the price of Co has increased leading to a demand for cheaper alternatives. Some examples of recently developed cathode materials with enhanced voltages and capacities are $\text{LiMn}_{1.5}\text{Ni}_{0.5}\text{O}_4$ (LMNO) (4.7 V and capacity 135 mAh g^{-1})³⁹, $\text{LiNi}_{0.8}\text{Co}_{0.15}\text{Al}_{0.05}\text{O}_2$ (NCA) (3.7 V and capacity 200 mAh g^{-1})⁴⁰ $\text{LiNi}_{0.33}\text{Co}_{0.33}\text{Mn}_{0.33}\text{O}_2$ (NMC) (3.7 V and 160 mAh g^{-1})⁴¹ and LiCoPO_4 (LCP) (4.2 V and 125 mAh g^{-1})⁴². Their higher performance and lower costs over LCO have led to the recent adoption of NMC and NCA for mass production.

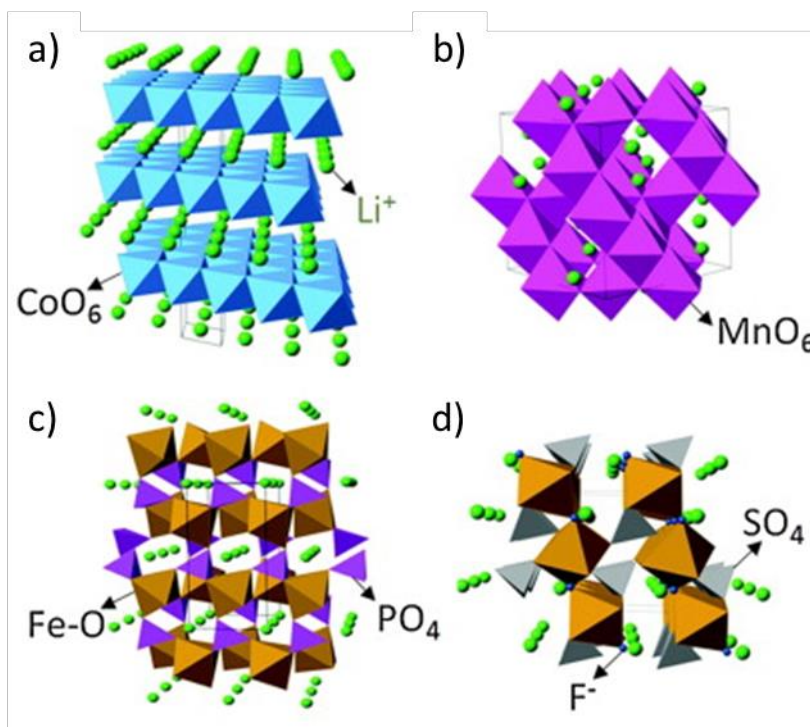


Fig. 1.3 Crystal structures of the 4 common crystal structures present in intercalation cathode materials. a) layered (LiCoO_2), b) spinel (LiMn_2O_4), c) olivine (LiFePO_4), and d) tavorite (LiFeSO_4F). Image reproduced from Islam et. al.³³

Depending on the material chosen for the anode, it can be used as the lower electrode with the cathode deposited above. There are however far more anode materials which are not thermally stable to the temperatures required for solid electrolyte processing. $\text{Li}_4\text{Ti}_5\text{O}_{12}$ is one exception which has a processing temperature of 500°C and other favorable properties of high rate capability and a high cycle life due to its low volumetric changes upon cycling.⁴³ The drawbacks are the low capacity compared to other anode materials (175 mAh g^{-1}) and the rather high voltage vs. Li of $\sim 1.55 \text{ V}$. Note that this would lower the overall voltage of the cell significantly when integrated. The most desirable anode material from the perspective of energy density and rate is definitely pure lithium metal with a capacity of 3860 mAh g^{-1} and the lowest cell potential.⁴⁴ However, there are several challenges to properly utilize it in a cell from its high reactivity to most electrolyte materials, which causes secondary phases to form at the interface, to its plating behavior which gradually reduces the surface area in contact with the electrolyte thereby raising the interfacial resistance greatly. As an alternative, silicon has also been widely researched due to its large capacity of up to 4200 mAh g^{-1} .⁴⁵ Thin film Si anodes have shown some success but the capacity is very limited due to the low thickness ($\sim 77 \text{ nm}$) required for good cycling stability.⁴⁶ Nanostructuring Si into nanowires has been demonstrated to increase the amount of Si per cm^2 while preserving cycling performance;⁴⁷ however the primary issue for Si anode continues to be the very large volume expansion of up to 300% upon full lithiation which causes cracking and loss of contact.

The solid electrolyte fulfils the roles of both the electrolyte and separator. As compared to conventional separators which are highly porous to allow the liquid electrolyte to flow through, solid electrolytes can be 100% dense, and therefore have a much greater mechanical stability. The mechanical stability enables the thickness of the electrolyte to be reduced to as low as 200 nm to minimize the internal resistance of the cell and further reduce the weight and size of the battery.

A large variety of solid electrolytes for Li^+ ions have been identified and are presented in terms of ionic conductivity in work by Bachman et. al.⁸ and electrochemical stability in work by Richards et. al.⁴⁸ in Fig. 1.4. In terms of ionic conductivity, solid electrolytes are generally lower than liquid electrolytes. With values ranging between 4×10^{-6} and $1 \times 10^{-2} \text{ S cm}^{-1}$. $\text{Li}_7\text{La}_3\text{Zr}_2\text{O}_{12}$,⁴⁹ LIPON,⁵⁰ $\text{Li}_{3x}\text{La}_{(2/3)-x}\text{TiO}_3$ ^{51,52} and $\text{Li}_{10}\text{GeP}_2\text{S}_{12}$ ⁵³ are some of the most researched electrolytes.

Interfacial layers between the solid electrolyte and electrodes have been shown to greatly improve Li^+ ion transport across the interface as well as easing the issue of chemical instabilities caused by high voltage materials. In the case of LLZO interlayers such as LiNbO_3 ⁵⁴ and LiAlO_2 ⁵⁵ prevent side reactions during synthesis and battery operation. The interface to Li metal can also be significantly improved with a silicon or Al_2O_3 interlayer which enables Li to properly wet the surface and plate more evenly during cycling.^{56,57}

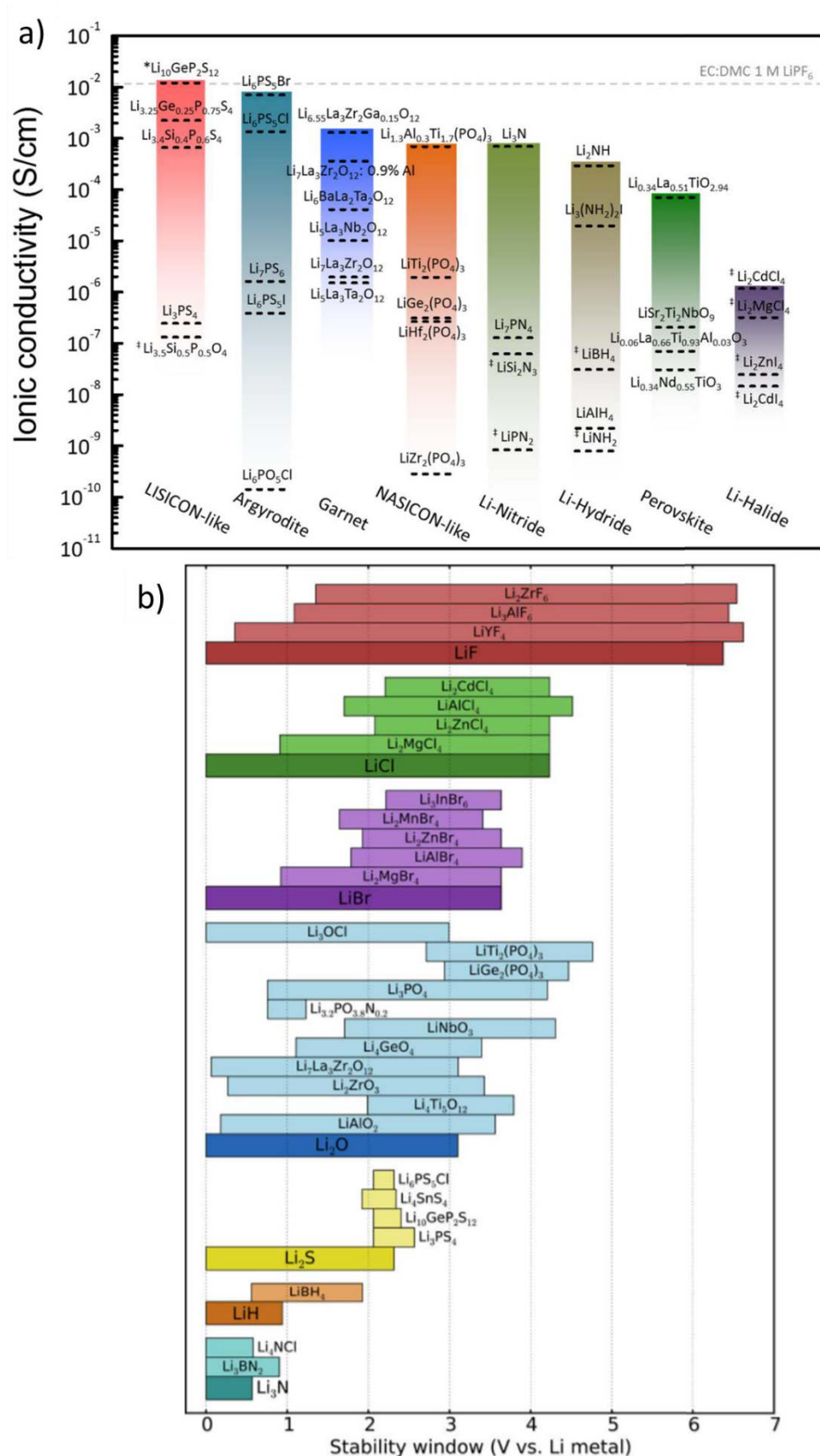


Fig. 1.4 a comparison of solid Li⁺ ion conductors in terms of a) ionic conductivity with groups determined by crystal structure from work by Bachman et. al.⁸ and b) electrochemical stability with groups determined by anion reproduced from work by Richards et. al.⁴⁸

1.5 The $\text{Li}_7\text{La}_3\text{Zr}_2\text{O}_{12}$ Ceramic Electrolyte

The focus of this work is on $\text{Li}_7\text{La}_3\text{Zr}_2\text{O}_{12}$, which was chosen due to its good balance of ionic conductivity and electrochemical stability. The ceramic $\text{Li}_7\text{La}_3\text{Zr}_2\text{O}_{12}$ (LLZO) garnet was first reported in 2007 by Murugan et. al.⁴⁹ A room temperature lithium ion conductivity of $\sim 1.90 \times 10^{-4} \text{ S cm}^{-1}$ was measured with electrochemical impedance spectroscopy. In addition to its relatively high ionic conductivity, its chemical stability when subjected to large voltage ranges is greater than solid electrolytes such as $\text{Li}_{3x}\text{La}_{(2/3-x)}\text{TiO}_3$ (with x between 0 and 0.16) and $\text{Li}_{10}\text{GeP}_2\text{S}_{12}$ which exhibit higher bulk conductivities, but are unstable in contact with Li metal.⁵⁸ Therefore, LLZO electrolytes offer a unique set of properties which can enable the development of cells with high voltage and energy densities for all solid-state microbatteries.⁵⁹

Structural characterization of LLZO revealed the existence of two primary polymorphs, cubic $Ia\bar{3}d$ (No. 230)⁶⁰ and tetragonal $I41/acd$ (No. 142)⁶¹ phases shown in Fig. 1.5. At room temperature the phase is tetragonal and a metastable transition to the cubic phase occurs at elevated temperature as low as 150°C .⁶² The cubic phase initially reported was found to remain stable at room temperature due to the inclusion of Al into the crystal structure, occurring during the high temperature annealing process in Al_2O_3 crucibles, commonly used to contain the powder.^{63,64} Therefore the calcination and sintering process for the Li-garnet materials strongly affects the phase present.

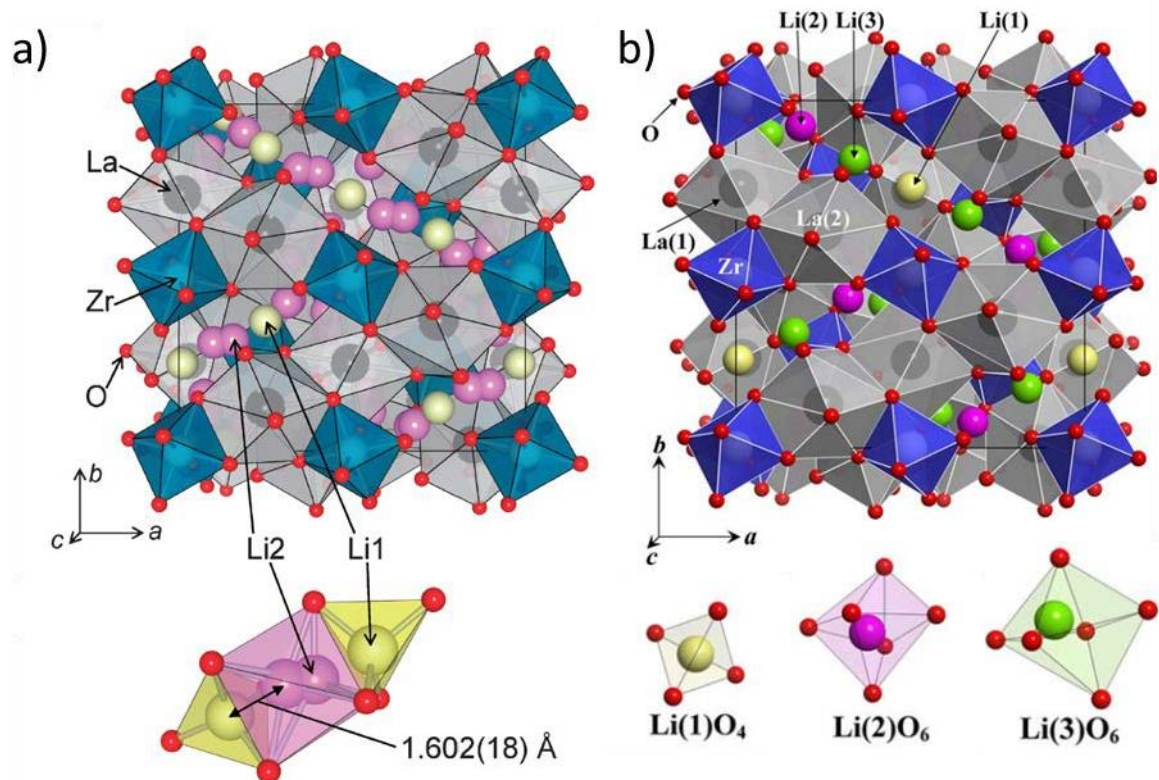


Fig. 1.5 crystal structure of a) cubic $\text{Li}_7\text{La}_3\text{Zr}_2\text{O}_{12}$ and b) tetragonal $\text{Li}_7\text{La}_3\text{Zr}_2\text{O}_{12}$ including Li^+ site co-ordinations with O^{2-} ions colored in red. Blue octahedra represent Zr units and grey polyhedra represent La units. Diagrams taken from work by Awaka et. al. in ref. 7(left) and 8(right).

In the solid-state processing method powders of $\text{LiOH}\cdot\text{H}_2\text{O}$, La_2O_3 , and ZrO_2 in stoichiometric quantities with 10wt% extra $\text{LiOH}\cdot\text{H}_2\text{O}$ are mixed *via* ball milling with isopropanol solvent. The resulting powder is dried then calcined at 800°C for at least 10h then pressed into pellets and sintered at temperatures up to 1250°C for times of up to 35h to achieve the cubic phase.^{65,66 67}

Aside from the solid-state processing method LLZO can also be processed *via* sol-gel synthesis. This is achieved by dissolving La_2O_3 , Li_2CO_3 and $\text{Zr}(\text{OC}_2\text{H}_5)_4$ into a solution of nitric acid, ethanol, citric acid and ethylene glycol. This mixture is dried and calcined then ball milled and put through several annealing processes from 200°C to 900°C to aid the incorporation of Al from the crucibles.⁶⁸ This method has the advantage of ensuring very good intermixing of the elements which results in lower sintering temperatures. The solid-state method however has become more popular due to its relative simplicity and the ability to reach higher densities.

As well as stabilizing the cubic phase, the lithium ion conductivity of LLZO can be improved through doping with a large variety of elements. The most common doping method is the original aliovalent substitution of Li^+ with Al^{3+} on the 24d and 96h sites which improves ionic conductivity by creating additional lithium vacancies in the lattice.^{60,62-64,66,69-76} There is a wide range of values quoted for the optimal Al concentration: between 0.15 and 0.35 per formula unit of LLZO. Using too little results in the formation of the tetragonal phase and too much causes Al-rich secondary phases to form. Another common doping strategy is the substitution of Zr with various cations, successful examples of these are Ta, Nb, and Y.⁷⁷⁻⁷⁹ Co-doping with two or more elements has also been explored usually by substituting Al^{3+} or Ga^{3+} on the Li^+ site in addition to a substitution on the La^{3+} or Zr^{4+} site for the garnet.⁸⁰⁻⁸⁶ Among the plethora of LLZO solid solutions gallium-doping on the lithium site with between 0.2 and 0.25 Ga per unit cell resulted in the highest conductivity of 1.2 mS cm^{-1} in experimental.⁸⁷⁻⁸⁹ and theoretical studies.⁹⁰ It has also been shown that adding Ga metal to pre-synthesized LLZO particles in an annealing process helps to reduce the sintering temperature and induces a phase change at temperatures as low as 600°C .⁹¹ Iron doped LLZO has recently been reported with a similar bulk ionic conductivity of $1.38 \times 10^{-3} \text{ S cm}^{-1}$.⁹²

The consistency of results for lithium ion conductivity between various research groups is poor, even for pellets with the same alloying element and concentration. There are several possible reasons for this but the most compelling is related to pellet density. It has been shown that there is a linear relationship between these parameters where lower densities lead to lower lithium ion conductivities.⁹³ For that reason, research into achieving pellet densities up to 99.8%, achieved through hot pressing methods, have yielded the highest lithium ion conductivities of up to $5.7 \times 10^{-4} \text{ S cm}^{-1}$ in undoped LLZO.⁹⁴ Other reasons for lower pellet lithium ion conductivity include the presence of varying amounts of impurity phases and under or over-stoichiometry of Li in the structure, which is also connected to the appearance of O^{2-} vacancies.⁹⁵

1.6 Thin Film Processing of $\text{Li}_7\text{La}_3\text{Zr}_2\text{O}_{12}$

By reducing the electrolyte thickness from pellet to thin films the proportion of electroactive material in the battery is increased. However, until now there has been little progress towards the integration of LLZO thin films into batteries. The primary reason for this has been the difficulty in processing dense, crack-free, and phase pure LLZO in the form of thin films with lithium ionic conductivity comparable to the bulk material. Several attempts have been made to deposit thin films of LLZO with various techniques such as pulsed laser deposition (PLD),⁹⁶⁻¹⁰⁰ magnetron sputtering,^{18,101} aerosol assisted deposition,¹⁰² sol-gel deposition,¹⁰³⁻¹⁰⁵ and metal-organic vapor deposition (MOCVD).¹⁰⁶ The type of method used has clear implications on the microstructure, phase-content and ultimately the Li-conductivity of the resulting film. For example, sol-gel deposition allows the stoichiometry to be controlled and therefore lithium loss, which occurs during high temperature processing, can be compensated for however, the density of the resultant film is often poor with a porous microstructure.^{107,108} Katsui and Goto achieved stabilized high purity thin films of cubic LLZO by actively controlling the lithium flow during deposition using MOCVD.¹⁰⁶ The granular growth and the required high substrate temperatures above 800°C making it challenging for integration into devices. Physical vapor deposition methods such as magnetron sputtering or PLD result in a higher film density, but lithium loss during deposition remains a challenge resulting in lithium deficient films which tend to form the non-conductive pyrochlore phase, $\text{La}_2\text{Zr}_2\text{O}_7$, more easily upon crystallization.

An explanation for the critical difference of two orders of magnitude between sintered pellet and thin film conductivities is still missing in the field and is required in order to develop a clear road map towards microbattery integration. Scrutinizing the literature reports, we conclude the following causes for the varied lithium ion conductivities for thin film LLZO electrolytes:

The first and most crucial point is the stabilization of the correct phase. For processing of the vacuum-based films ablation of sintered pellets is predominantly used. Although the pellet may have the desired chemistry and phase, transfer of the structures to thin films can result in lithium loss and subsequent phase-destabilization during thin film growth due to the volatility of lithium and the high laser energy required. This explains the challenges in growing cubic LLZO thin films by PLD according to references.^{96,97,99} On the other hand, turning to wet-chemical film depositions avoids using high laser energies and even sintering, but it is well known that classic wet-chemical oxide film depositions have several additional factors to consider such as the chain length and number of cations in the organic precursors which can influence the degree of crystallization and stabilization of the phases.¹⁰⁹ Despite this general knowledge, detailed parameter studies are still missing in the field of LLZO wet-chemical film processing.

Secondly, the morphology of the reported films vary from dense and crack free to highly porous, as in the case of sol-gel deposited films where outgassing organics can cause pores and cracks to form. Reviewing the current literature it can be concluded that there is a strong dependence of the morphology on the processing method used with vacuum deposition methods generally resulting in higher film densities and phase purities.^{30,31} The formation of cationic

segregates may also influence the surface morphology and porosity as evident for many other oxide-based thin films.^{110,111} To the best of our knowledge studies on surface segregations and its effect on surface film morphologies and chemistry have not been published for LLZO thin films.

Thirdly, the effect of lithium concentration on ionic conductivity is complex and depends on several parameters such as the effective doping level and structural lithium site occupancy ratios between tetragonally and octahedrally coordinated sites.⁷³ Other factors may also play a role in changing lithium concentrations such as the segregation of lithium and aluminium to the surface, thereby changing the active lithium concentration as observed in pellets of LLZO.¹¹² It is well known in literature that cationic surface segregation can also strongly affect the ionic conductivity of oxides.^{113,114} As lithium is highly volatile in nature and its loss is compensated by chemistry and phase changes, further studies are crucial to shed light on how to best process LLZO thin films for future garnet-electrolyte based microbatteries and to optimize electrolyte-electrode lithium transfer for large-scale battery systems. For thin films with nanoscaled grains the kinetics of lithium ion transport and thermodynamics of crystallization may be significantly different from the bulk, macrocrystalline ceramics. Knowledge on phase stability, fabrication and Li-characteristics of nanograined structures is key to improving future battery performances as highlighted in recent work by van den Broek demonstrating that a nanograined LLZO interface significantly reduced interfacial resistance and improved battery cycling.¹⁶ Thus far the extent of Li loss resulting from vacuum and high temperature processing of LLZO based thin films is unknown. The lack of this type of data in the field is most likely due to the difficulty of measuring Li particularly in thin films. Methods such as elastic recoil detection analysis (ERDA), inductively coupled plasma atomic emission spectroscopy (ICP-OES), and nuclear reaction analysis (NRA) could be utilized in this direction.

Lattice strain may also play a significant role, in other thin film systems strain can alter ionic conductivity by orders of magnitude.^{115,116} We summarize that the influence of lattice strain imposed by the substrate is still unknown for LLZO thin films and could alter the phase stability as well as cationic segregation. Finally we consider the importance of size-dependent phase transformations in which the reduction of particle size to the sub 100 nm scale increases the influence of the surface energy and induces a phase change. For the LLZO system one recent study exhibited this effect showing that the surface energy of cubic-LLZO is greater than tetragonal-LLZO and therefore a reduction in particle size led to the stabilization of cubic-LLZO.¹¹⁷ This phenomenon is also demonstrated in other phase polymorphous ceramics such as titania¹¹⁸ and zirconia.¹¹⁹⁻¹²²

1.7 Aims of the thesis

Solid-state batteries have several advantages over their liquid counterparts. Device safety is greatly improved by removing flammable components. Energy density is raised by dispensing with thick separator layers of 20 microns and by changing the porous electrode structure to a dense one with no inactive carbon or polymer components. Moreover, high power outputs are possible at raised temperatures. However, research into thin film solid-state

electrolytes is still at an early stage, and several questions about the influence of film processing on the final phase formation and lithium ion conductivity remain unanswered.

Taking this into consideration, the objective of this work is divided in two parts: first, to study the deposition of thin films of the solid electrolyte $\text{Li}_7\text{La}_3\text{Zr}_2\text{O}_{12}$ and its post processing towards the formation of the highly conductive cubic phase and strategies to maintain the lithiation level. Second, to tackle the challenge of thin film all-solid-state batteries based on $\text{Li}_7\text{La}_3\text{Zr}_2\text{O}_{12}$ through the development of a highly stable current collector which can withstand the subsequent processing of all layers of the thin film battery, enabling multi-layered structures with low interfacial resistances to be produced.

2 On the Chemical Stability of Post-Lithiated Garnet Al-Stabilized LLZO Solid-state Electrolyte Thin Films

This chapter is based on the following paper:

M. Rawlence, I. Garbayo, S. Buecheler, J.L.M. Rupp, *Nanoscale*, **8**, 14746-14753, 2016

2.1 Introduction

The goal of the work presented in this chapter is to develop a method for enhancing the lithium content of amorphous Al doped LLZO thin films and crystallizing them into cubic phase LLZO in a single annealing process. Findings are presented and discussed with regard to the phase stabilization and microstructural development of a series of four films with thicknesses between 90 and 380 nm. The impact of the post-lithiation treatment on ionic conductivity is determined using electrochemical impedance spectroscopy, which is an important step towards integrating these solid electrolyte films in future microbatteries.

2.2 Experimental

2.2.1 Thin film preparation by pulsed laser deposition and post-lithiation-annealing for Al doped lithium lanthanum zirconate electrolytes

To create a target for ablation in pulsed laser deposition, a pellet with the target composition $\text{Li}_{6.22}\text{La}_3\text{Zr}_2\text{Al}_{0.26}\text{O}_{12}$, henceforth referred to as Al : LLZO, was synthesised using a sol-gel Pechini synthesis route. Precursor salts were measured in stoichiometric quantities with an additional molar 10% of lithium: for this, Li_2CO_3 (Alfa Aesar, 99%), $\text{La}(\text{NO}_3)_3 \cdot 6\text{H}_2\text{O}$ (Alfa Aesar, >99.9%), $\text{Zr}(\text{C}_5\text{H}_7\text{O}_2)_4$ (Alfa Aesar), and $\text{Al}(\text{NO}_3)_3 \cdot 9\text{H}_2\text{O}$ (Fluka, >99%) were dissolved into water with added HNO_3 to keep the cations in solution. Citric acid and ethylene glycol were added to the solution to act as the complexing and polymerising agents, respectively. The solution was left to polymerise for 6 hours at 110 °C then fired at 900 °C for 10 hours in dry O_2 to burn off the organic components and form tetragonal Al : LLZO. The resulting powder was ground by hand then isostatically pressed with an additional 10 mol% of Li_2O (Alfa Aesar, 99.9%) at 1000 MPa. Finally, the pellet was covered in parent powder and sintered at 1050 °C for 10 hours in dry O_2 to form the cubic phase. Pellets were 25 mm in diameter and had a theoretical density of 90% (5.022 g cm^{-3} is the maximum). Alumina crucibles and plates were used for high temperature processes, which may slightly alter the final Al content in the pellet. However, this effect was considered to be negligible as the cubic garnet phase was successfully stabilized with no significant secondary phases according to XRD shown in Fig. 2.1. Grinding and handling of powders was done within a custom designed glovebox set up for solid-state battery cells (Inert, USA, and Electrochemical Materials, ETH) under Ar gas with <2 ppm water and O_2 levels to limit exposure to moisture.

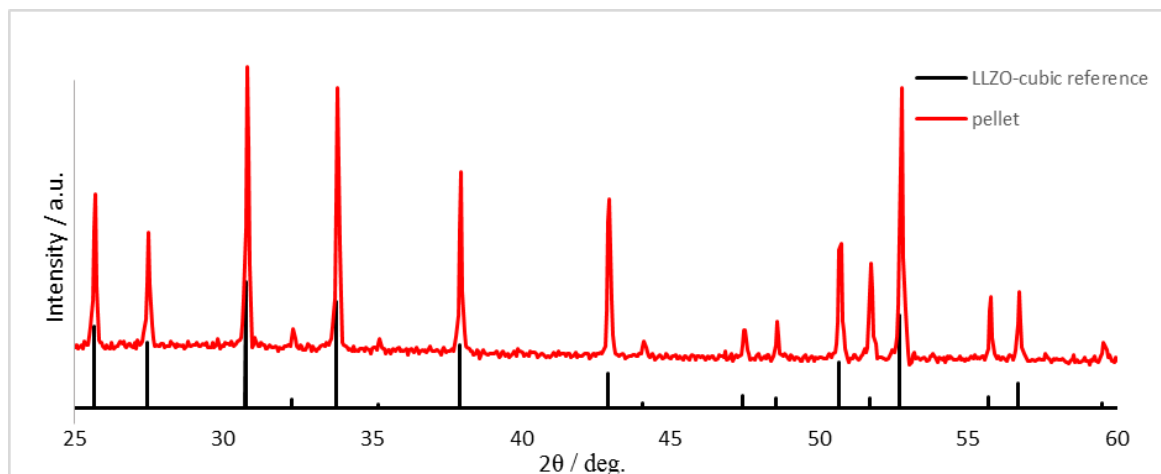


Fig. 2.1 XRD pattern of the sol-gel synthesized pellet with reference data for cubic phase $\text{Li}_7\text{La}_3\text{Zr}_2\text{O}_{12}$: ICSD No. 422259. All thin films were deposited from this pellet via PLD.

Thin films were deposited by pulsed laser deposition (PLD, Surface Technologies, Germany; KrF laser, 248 nm) with a laser energy of 0.54 J cm^{-2} per pulse and a pulse frequency of 10 Hz. Additionally an O_2 partial pressure of 10 mTorr and substrate temperature of 50°C were maintained. Films were deposited onto square, single crystal, (100)-oriented, double-side polished, MgO (Crystec, Germany) kept at a target-substrate distance of 65 mm. Film thicknesses were estimated based on a calibration connecting the number of shots based on fixed laser conditions with resultant film thickness observed *via* SEM cross-section analyses.

The method used for post-annealing the films under a lithium partial pressure to avoid lithium losses or segregation at temperature is shown schematically in Fig. 2.2. An alumina crucible with a 20 mm diameter contains the film and 100 mg of Li_2O powder which readily converts to LiOH in air. The crucible was then sealed in air with ceramic glue (Thermokitt Roth, Carl Roth GmbH, Germany) and annealed at 600°C for 24 h under a flow of oxygen. During this time, the LiOH melts and creates lithium rich atmosphere.

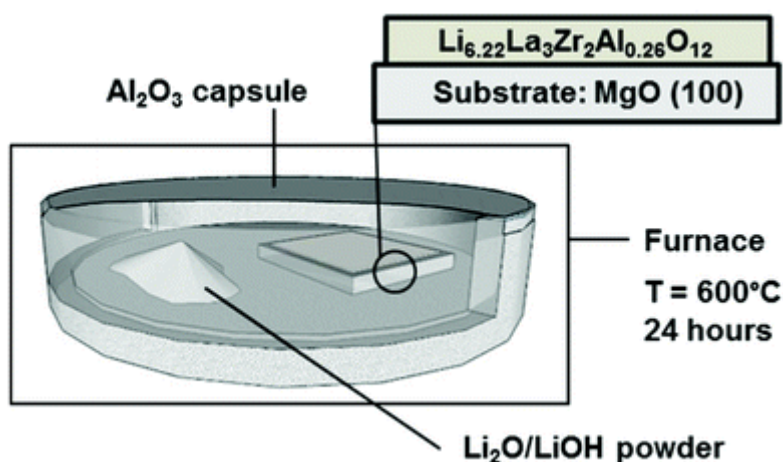


Fig. 2.2 Schematic of thin film annealing setup. The Al_2O_3 capsule is shown partly transparent to reveal the Li source powder and thin film inside.

2.2.2 Structural and electrochemical investigation of Al doped lithium lanthanum zirconate thin films

In order to identify the crystallographic phase, X-ray diffraction (XRD) was carried out using a Bruker D8-diffractometer using a Cu source with $K_{\alpha 1}$ wavelength at an accelerating voltage of 40 keV with Bragg–Brentano geometry for pellets and grazing incidence geometry for thin films with an incidence angle of 2° . Scanning Electron Microscopy using an FEI Nova NanoSEM 230 at 2 to 5 keV was conducted on thin films using a 5 nm sputtered platinum coating to mitigate charging effects.

For electrochemical studies 100 nm thick gold contacts were deposited onto the film using thermal evaporation (Plassys II, France) through a custom made, laser cut, stainless steel shadow mask with a minimum electrode separation of 250 μm . A 2-point electrode geometry was used for electrochemical impedance spectroscopy (EIS) (Zahner, Germany) to probe the AC ionic conductivity over a range of temperatures, during both heating and cooling, with an alternating voltage of ± 50 mV and frequency range between $1 \times 10^6 - 0.1$ Hz. The sample was measured on a Linkam stage (HFS-600E, UK) with Au-coated tungsten microprobes and electric measurements were carried out in a constant synthetic air gas flow of 40 sccm. Temperature was directly measured on the sample surface with a K-type thermocouple.

2.3 Results and Discussion

2.3.1 Al doped lithium lanthanum zirconia thin film electrolytes without post-lithiation: as-deposited PLD film

The microstructure and morphology of $\text{Li}_7\text{La}_3\text{Zr}_2\text{O}_{12}$ based thin films processed by pulsed laser deposition at 50°C were investigated directly after deposition, Fig. 2.3. Here, the examination of the as-deposited $\text{Li}_7\text{La}_3\text{Zr}_2\text{O}_{12}$ thin film microstructure by SEM reveals the successful deposition of a dense and crack-free thin film with an indication of particulate ejection during processing, common in PLD depositions,¹²³ Fig. 2.3a The cross section of the same film confirms the dense microstructure, Fig. 2.3b. We conclude based on the SEM cross-section an average film thickness in the range of 320 ± 15 nm with a slight tendency for columnar grain growth in its microstructure. We investigate the crystallinity of the as-deposited PLD film *via* grazing incidence XRD, Fig. 2.3c. Here, we measure a single broadened diffraction peak ranging from 21° to 35° for the film as deposited at 50°C . There are also some low intensity peaks besides the broadened peak which can be assigned to the (211), (321), (420), (422), (532), and (642) miller indices of the bulk polycrystalline cubic- $\text{Li}_7\text{La}_3\text{Zr}_2\text{O}_{12}$ (c-LLZO) phase, in accordance with literature.⁶³ The results are in agreement with earlier PLD studies on LLZO film formation by Park *et al.*⁹⁹ who also used an O_2 pressure of 10 mTorr during deposition but three times the laser fluence at 1.5 J cm^{-2} .

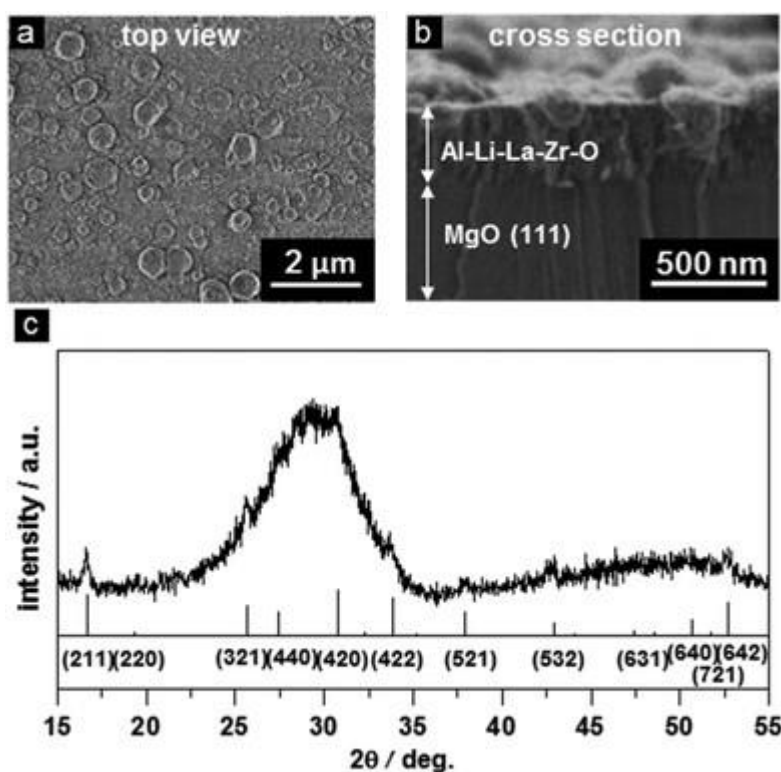


Fig. 2.3 An as-deposited $\text{Li}_7\text{La}_3\text{Zr}_2\text{O}_{12}$ based thin film deposited on a single crystal MgO substrate at 50 °C by PLD (a) top view SEM micrograph and (b) cross-sectional SEM micrograph. (c) XRD pattern of amorphous thin film structure and comparison to reference $\text{Li}_7\text{La}_3\text{Zr}_2\text{O}_{12}$ cubic structure.

2.3.2 Post-lithiated and annealed PLD films of Al-doped lithium lanthanum zirconate films: structural and morphological analysis

As PLD deposition is a technique which can cause a lower relative yield of lithium due to its high volatility in a vacuum,¹²⁴ and a high proportion of lithium is essential for crystallization of the garnet LLZO (see Afyon⁹¹ and Rettenwander¹²⁵ for detailed discussions) we subject the films to a lithium post-annealing step after PLD deposition. The films are annealed on the one hand to ensure sufficient crystallization to switch from amorphous to long range order, and on the other hand to ensure enough lithium is present for LLZO to form without lithium free secondary phases by providing excess lithium powder in the closed crucible at high temperatures. Thus far for thin film processing of LLZO films this route was not considered and standard annealing often lead to the formation of lithium free phases at higher temperatures.^{96,99}

We study a series of films with increasing thickness from 90 to 380 nm, which were subjected to the lithium post-annealing treatment after PLD, and analyse the microstructures with SEM shown in Fig. 2.4 and X-ray diffraction in Fig. 2.5. All films were annealed under the same conditions of 600 °C for 24 h in the presence of a $\text{Li}_2\text{O}/\text{LiOH}$ reservoir.

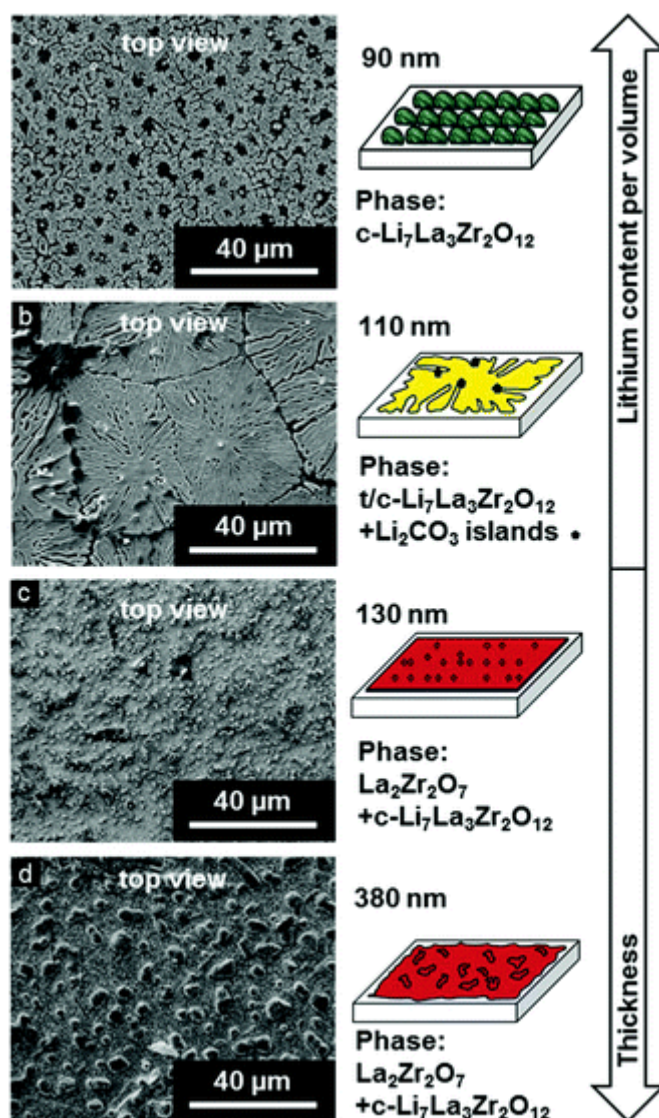


Fig. 2.4 SEM micrographs of $\text{Li}_7\text{La}_3\text{Zr}_2\text{O}_{12}$ thin film series of increasing thickness (a) 90 nm (b) 110 nm (c) 130 nm (d) 380 nm. Accompanying schematics combine information from Fig. 3.3 and 3.4 to show the progression of phase and morphology as the thickness is increased. All films are deposited on MgO and post annealed with the lithium treatment.

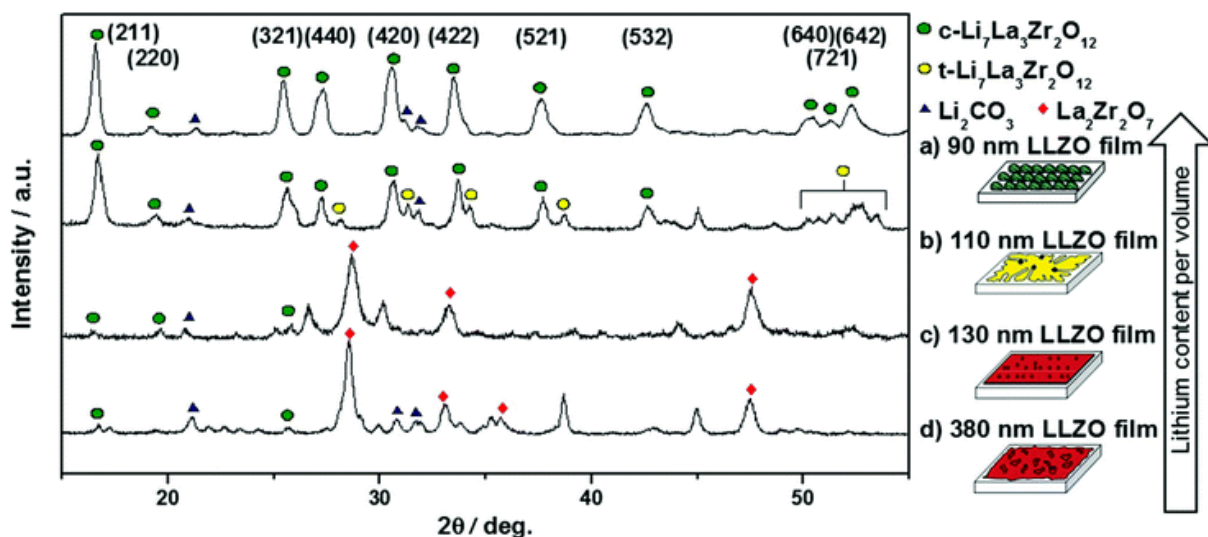


Fig. 2.5 XRD of $\text{Li}_7\text{La}_3\text{Zr}_2\text{O}_{12}$ film series of increasing thickness. Miller indices are of the $\text{c-Li}_7\text{La}_3\text{Zr}_2\text{O}_{12}$ phase. Other symbols denote impurity phases present in the films.

In Fig. 2.4 the scanning electron micrographs show a clear progression in the microstructure from the formation of separate islands for the film of 90 nm thickness, Fig. 2.4a, to more continuous patches of de-wetted material for the 110 nm thick film, Fig. 2.4b. Moving to 130 nm thickness results in a fully continuous film microstructure of more dense material with nano-sized crystallites on the surface, Fig. 2.4c. At 380 nm the film is continuous and has similar density to the 130 nm film, however, a roughened surface is observable with features several microns across on the film surface.

The crystallinity and formation of phases is now assessed for films of varying thicknesses via X-ray diffraction, Fig. 2.5. The 90 nm thick film is of cubic LLZO phase, indicated by the presence of all diffraction indices of (211), (220), (321), (440), (420), (422), (211), (521), (640), (721), and (642), Fig. 2.5a. This single c-LLZO phase is in good agreement with literature for polycrystalline pellets.⁶³ In addition, a small amount of Li_2CO_3 formed during the processing is measurable, in agreement with earlier reports on bulk pellet surface reactions.¹²⁶ We attribute this to the reaction of excess LiOH on the surface of the film reacting with CO_2 in the air during post-process characterization and can observe this in some of the following microstructures as well. A slight increase in film thickness to the 110 nm thick structure, results in the formation of a mixed phase including both tetragonal and cubic LLZO, Fig. 2.5b. For the 130 nm thick film, one observes the cubic LLZO phase in combination with the lithium deficient $\text{La}_2\text{Zr}_2\text{O}_7$ (LZO) pyrochlore phase.¹²⁷ The increase in LZO phase coupled with the reduction in LLZO suggests that the pyrochlore phase forms at the expense of the tetragonal/cubic LLZO phases, Fig. 2.5c. At 380 nm film thickness the majority of the film has formed into LZO while a small quantity of cubic LLZO is noted, Fig. 2.5d. Additional surface impurity phases of Li_2CO_3 are also measurable. By analyzing the FWHM, it is apparent that the crystal size in all the films is on the nanoscale. Furthermore, the LLZO majority films appear to have a smaller grain size than the thicker LZO containing films.

We interpret the morphological and phase changes in the Al–Li–La–Zr–O thin film microstructure as follows in light of the post-lithiation annealing treatment and effective lithiated film volumes:

Firstly, at small film thickness up to 90 nm a pure bulk c-LLZO film prevails. In this state the film reveals a degree of lithiation per film volume in the correct range for stabilizing the cubic-LLZO phase, Fig. 2.4a and 2.5a. Too little lithium would result in the formation of the LZO whereas a lithium excess would cause the formation of other lithium rich phases such as AlLiO_2 and LaAlO_3 .¹²⁸ Here, the films appear to have a high surface tension due to the surface energy difference between the MgO substrate and film. Island formation, shown in the scanning electron micrographs in Fig. 2.4a, is the result of the minimization of the surface energy during annealing which is dependent on key parameters such as film thickness, surface defects and stress-driven changes during crystallization.¹²⁹

Secondly, we observe an intermediate state at which both the tetragonal and cubic phases co-exist for the film thickness of 110 nm, Fig. 2.4b and 2.5b. One hypothesis could be that change in surface energy during a phase transformation from cubic to tetragonal would reduce the tendency for sub-micron island structures to form resulting in the formation of more connected film patches.

Thirdly, for larger film thicknesses above 110 nm the post-lithiation step is not sufficient to lithiate the whole bulk volume consistently, Fig. 2.4c and d and 2.5c and d. The trend shows that as the thickness increases, the transition from a largely amorphous film to co-existing tetragonal and cubic LLZO phases, instead forms the lithium deficient $\text{La}_2\text{Zr}_2\text{O}_7$ (LZO) phase, Fig. 2.5c and d. In this phase transition the film maintains a much higher density and a continuous film microstructure is displayed, Fig. 2.4c and d. This finding of lower lithium contents for film above the threshold of 110 nm has also been noted in a paper by Park *et al.* where small quantities of LLZO were observed on the surface of a thicker film synthesized at a temperature of 700 °C which was otherwise mainly composed of LZO.⁹⁹

In summary, we report that there is currently a compromise between forming a higher density film microstructure and achieving thermodynamic stability of the c-LLZO phase, which depends crucially on the degree of lithiation per volume in the chemistry of the film structure. We demonstrate a range of thermodynamic transitions from single bulk phase c-LLZO with disconnected and de-wetted islands forming on an MgO substrate, to an intermediate mixed t/c-LLZO phase, leading to a c-LLZO and lithium deficient LZO phase mixture with a continuous and crack-free morphology and a lower lithium content to volume ratio. We observe a fine balance between the formation of each phase and their surface energies, exhibited by de-wetting of the film microstructures. Importantly the results suggest that during the post-lithiation synthesis step lithium incorporation into the film is inhibited since the largest film thicknesses are the ones revealing the lowest incorporation of structural lithium. Both the increase in surface area and the smaller grain size in the 90 nm and 110 nm films could have affected the ability of the films to absorb lithium. A larger surface area would result in a higher surface reaction rate and the presence of more grain boundary interfaces exposed to the surface could improve the lithium in-diffusion. Judging from these experiments it is evident that stabilizing pure c-LLZO in dense thin film microstructures is challenging on the MgO substrate. Hence, we have chosen the mixture of c-LLZO/LZO for electrochemical characterization as it is dense and could

therefore be realistically integrated into a microbattery. We compare this model experiment showing the range of phase changes to a second report on Al : LLZO PLD films mostly discussing polycrystalline films with phase mixtures of c-LLZO/LZO see Park *et al.*⁹⁹

2.3.3 Electrical conductivity of Al doped lithium lanthanum zirconia thin films: effect of lithiation and phase

To measure the effectiveness of the lithiation treatment post-PLD, we measure the electrochemical properties of the 380 nm film and compare to literature. We utilize the classic 2-probe geometry with gold electrodes for in-plane electrochemical impedance spectroscopy measurements. An example of the electrochemical impedance response obtained for the 380 nm thick c-LLZO/LZO film is given in Fig. 2.6a, in a Nyquist plot representation measured at 240 °C and 450 °C in dry synthetic air. In general, a clear impedance arc is measured at higher frequencies, which is attributed to the bulk resistance of the film. A second semicircle is also generally observed towards the lower frequencies, most probably associated to the grain boundary contribution. Finally, at high temperatures the blocking Au electrode contribution is clearly differentiated as a linear capacitive feature at a $\sim 45^\circ$ angle, as seen in the 450°C measurement in the Fig. 2.6a inset. The impedance data was fitted using an equivalent circuit with a single RC component for the high frequency part, denoting the bulk resistance of the film. At 325 °C this resulted in a lithium ion bulk conductivity of $1.2 \times 10^{-3} \pm 0.05 \times 10^{-3} \text{ S cm}^{-1}$ as compared to $\sim 1.7 \times 10^{-3} \text{ S cm}^{-1}$ for Park *et al.* in the same temperature range.⁹⁹

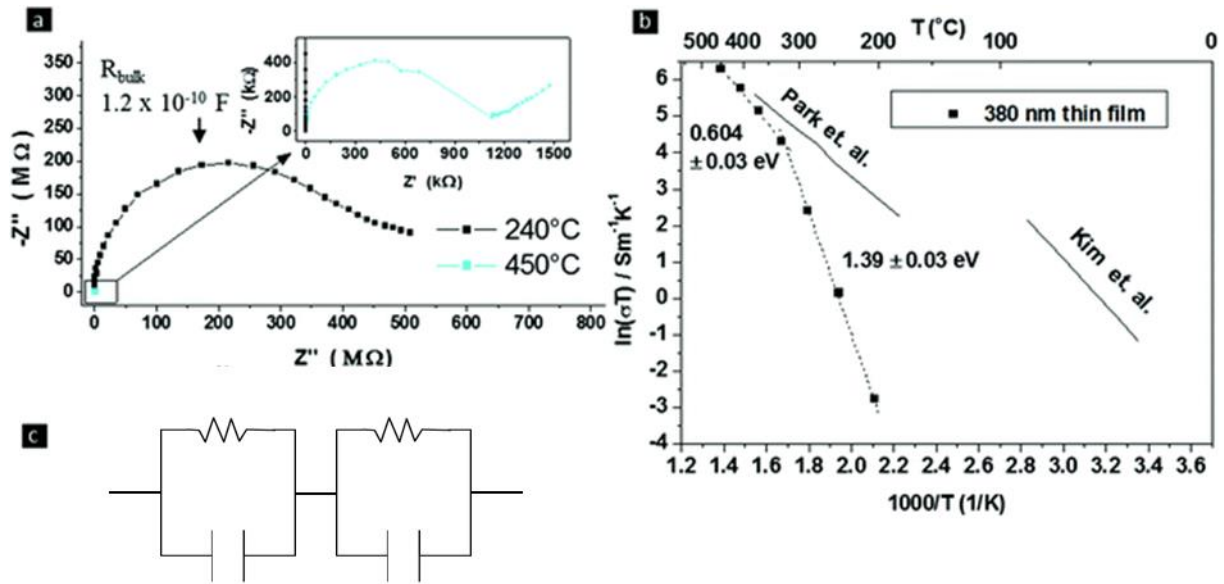


Fig. 2.6 (a) Electrochemical impedance spectroscopy measured at 240 °C and an inset at 450 °C for 380 nm lithium post treated film. (b) Arrhenius type plot of 380 nm films with activation energies included. References are provided for comparison. (c) Circuit model used to describe the trend seen in the Arrhenius plot. 2 RC elements which could represent the oxygen ion conductivity of the $\text{La}_2\text{Zr}_2\text{O}_7$ phase and the lithium ion conductivity in the $\text{Li}_7\text{La}_3\text{Zr}_2\text{O}_{12}$.

In an Arrhenius type plot we compare the films of c-LLZO/LZO synthesized *via* PLD and post-lithiation in this work to literature, Fig. 2.6b. The 380 nm thick film reveals two activation energies for ionic conductivity of 1.39 ± 0.05 eV for the temperatures range of 25 to 300 °C and a lowered one of 0.6 ± 0.05 eV for temperatures up to 400 °C. Upon cooling, the activation energy returns to the lower value demonstrating reversible behavior. The sudden change in activation energy indicates that a different mechanism for ionic transport is dominant in the higher temperature regime. In Fig. 2.6c a proposed circuit model is presented for interpreting the impedance data. One hypothesis for this behavior is that at lower temperatures the high activation energy originates from the lithium deficient LZO phase¹³⁰⁻¹³² and lithium ion pathways through the bulk of the film become more dominant at temperatures above 300 °C. Alternatively a metastable phase with a higher lithium ion conductivity may form at higher temperatures.

The activation energies seen here compare closely to 0.67 eV for polycrystalline c-LLZO/LZO films synthesized by PLD without post-lithiation treatment by Park *et al.*,⁹⁹ and are slightly higher than the PLD-grown epitaxial LLZO reported by Kim *et al.* (0.52 eV).⁹⁶ We attribute the small differences in bulk conductivity at high temperatures measured between the here synthesized 380 nm thick film and Park's work to slight difference in the quantity of c-LLZO over the non-lithiated LZO phase. Moreover, the greater performance reported by Kim *et al.* might come from the different film morphology, *i.e.* polycrystalline films *vs.* epitaxially grown films.

It is to be noted that based on this impedance study we demonstrate that reasonable conductivities of 1.2×10^{-3} S cm⁻¹ can be achieved at 325 °C, which may be used for operation of microbattery architectures in a mid-to-elevated temperature regime.

2.4 Conclusion

We have presented this model experiment on garnet based Li₇La₃Zr₂O₁₂ thin films to study the interplay of phase formation, microstructural evolution, and chemical stability for Li₇La₃Zr₂O₁₂ thin films on MgO substrates processed by pulsed laser deposition and a post-lithiation step. For these we investigated the changes in film microstructures relative to film thickness (whereby the effective lithiation per volume is manipulated).

Dense and crack-free amorphous thin film microstructures are synthesized directly after pulsed laser deposition at 50 °C. Through annealing at the relatively low temperature of 600 °C in the presence of a LiOH partial pressure the films were lithiated to varying degrees. We observe that at low film thicknesses of 90 nm (high lithiation degree per volume) an inhomogeneous film of de-wetted islands on MgO forms, but is composed of the desired highly lithium ion conducting c-LLZO phase. Increasing thickness to 110 nm results in an intermediate combination of cubic and tetragonal LLZO phases still with a large degree of de-wetting. Finally, we conclude that for film thicknesses of 130 nm and above a phase mixture of c-LLZO and LZO prevails coupled with a sufficiently dense film microstructure for electrochemical operation. Interestingly, there exists a fine balance between the thermodynamic phase stability, degree of lithiation, and degree of de-wetting for the Al–Li–La–Zr–O material in the form of

thin films. The large increase in surface area of the thinner films caused by the de-wetting is a strong indication that lithium incorporation is dependent on a surface reaction followed by a lithium diffusion processes on the nanoscale. The challenge is clearly to keep the lithium integrated into the structure, but also to avoid potential inhomogeneities in the film microstructures. Through this work the clear additional challenges of processing and establishment of stable phases and microstructures are revealed when comparing to classic bulk ceramic pellet processing.

Based on our results from the model experiment presented we conclude that for films of thicknesses larger than 130 nm processed by the post-lithiation treatment after pulsed laser deposition, stable and dense structures can be formed suited for conductivity studies in a 2-point geometry with microelectrodes. Electrochemical studies showed a high activation energy of 1.39 eV for the 380 nm film at temperatures below 300 °C. Above 300 °C a different mechanism for lithium transport emerged with an activation energy of 0.6 eV which was comparable to other LLZO thin films in literature with a phase mixture of c-LLZO/LZO. Here, future work on lithium ion conduction mechanisms in thin films may elucidate further on what we observe in our experiments.

We demonstrate here a systematic transition of the phase formation relative to film thickness which reveals key information on the stability of c-LLZO in thin films. These first reported trends lead the way for further improvement in the processing of LLZO for electrolytes in micro-batteries.

3 The Effect of Gallium Substitution on Lithium Ion Conductivity and Phase Evolution in Sputtered $\text{Li}_{7-3x}\text{La}_3\text{Zr}_2\text{Ga}_x\text{O}_{12}$ Thin Films

This chapter is based on the following manuscript that is submitted for publication:

M. Rawlence, A. N. Filippin, A. Wäckerlin, T.-Y. Lin, E. Cuervo-Reyes, A. Remhof, C. Battaglia, J.L.M. Rupp, S. Buecheler, Submitted, 2017

3.1 Introduction

In this chapter we present a radio-frequency magnetron co-sputtering approach that allows Li losses to be actively compensated for and the addition of phase stabilizing elements to be controlled. With simultaneous co-sputtering from ceramic LLZO and Li_2O targets we obtain Li stuffed LLZO thin films. To stabilize the highly conductive cubic LLZO phase, lithium was partially substituted by gallium atoms through multilayer depositions of LLZO + Li_2O / Ga_2O_3 followed by annealing in controlled ambient temperature. In-situ XRD during the post deposition annealing on thin films with a range of varied Ga concentrations provides a detailed view of the crystallization processes from amorphous state in the as-deposited film into cubic-phase polycrystalline LLZO. Here, we contribute to the fundamental understanding of how Ga concentration affects phase formation and stability of LLZO thin films. These results indicate that crystallization of cubic LLZO already can start at temperatures as low as 500 °C. This finding has strong implications on the materials and design of thin film batteries. The effect of tailoring the Ga concentration on the lithium ion conductivity is investigated by impedance spectroscopy at different temperatures. Non-Arrhenius behavior of the ionic conductivity is observed and its origin is discussed. Finally, conclusions on the role of gallium in the structure formation and stabilization of cubic LLZO structures are presented which serve as engineering guidelines to design future solid-state batteries.

3.2 Experimental

3.2.1 Preparation of solid-state electrolyte thin films by co-sputtering

Radio-frequency (RF) magnetron sputtering equipment (Orion sputtering system, AJA) with five cathodes in confocal off-axis geometry was used for growth of the thin films. Sputtering targets composed of Li_2O (3N, 90% density), $\text{Li}_7\text{La}_3\text{Zr}_2\text{O}_{12}$ (3N, 90% density), and Ga_2O_3 (4N, 90% density) mounted on Cu backing plates were used from TOSHIMA Manufacturing Co., Japan. The MgO (Crystec, single crystal (100), 10 mm x 10 mm) substrates were pre-cleaned using Ar plasma etching with a substrate bias of 20W for 2 min. Reference films were deposited from the LLZO target without intentional substrate heating (monitored substrate temperature did not exceed 50 °C during deposition). Li-stuffed LLZO films were

obtained by simultaneous co-sputtering from LLZO and Li_2O targets. The deposition rates from the individual targets were measured before the film growth using a quartz crystal microbalance positioned where the substrate would be during deposition. During deposition constant rates are assumed. The deposition rates are adjusted to a ratio of 1 mole LLZO per 4 moles of Li_2O . The following deposition parameters were used: 25 sccm Ar flow, process pressure 50 mPa, working distance of 11.8 cm, Li_2O target power density 5 W cm^{-2} , LLZO target power density 2.5 W cm^{-2} .

The addition of various amounts of Ga into the film was achieved through multilayer deposition of LLZO + Li_2O and Ga_2O_3 with a total of 6 layer sequences, as shown in Fig. 3.1. The targeted Ga concentrations (x_{Ga}) in the compound $\text{Li}_{7-3x}\text{Ga}_x\text{La}_3\text{Zr}_2\text{O}_{12}$ were $x_{\text{Ga}} = 0.2, 0.18, 0.16$ and 0.14 . The thickness of the 6 Ga_2O_3 interlayers was varied for the targeted Ga concentrations. The proportion of Li_2O in the co-sputtered layer was adjusted taking into account the added amount of Ga_2O_3 in order to obtain stoichiometry. The nominal composition of each film was calculated based on quartz crystal microbalance rate measurements prior to depositions. The Ar flow rate and pressure were kept constant (25 sccm and 50 mPa respectively), and the power density used for Ga_2O_3 deposition was 3 W cm^{-2} .

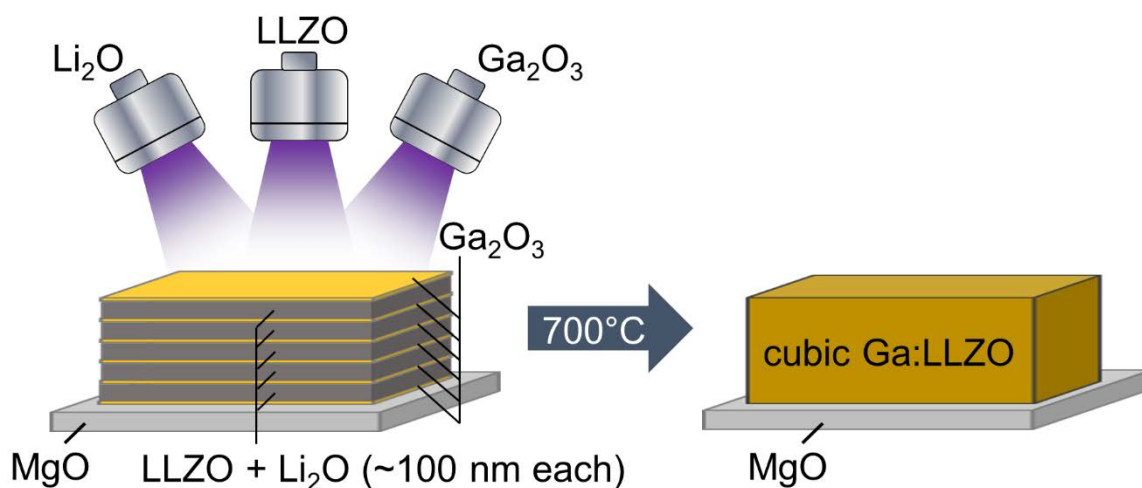


Fig. 3.1 Schematic of method for forming thin film gallium doped LLZO based on multilayer co-sputtering and a post-annealing process.

3.2.2 Characterization of crystalline microstructure and ionic conductivity

The amorphous films deposited at RT were placed in an Anton Paar XRK 900 reaction chamber with Be windows for heating the samples up to 700°C , measured *via* thermocouple, under a flow of 50 sccm O_2 . During the heating in-situ grazing incidence X-ray diffractograms were obtained using a PANalytical X'Pert³ powder diffractometer using a Cu K_α wavelength at an accelerating voltage of 35 keV with grazing incidence geometry and an incidence angle of

1°. Post-annealing measurements were carried out using the same tool and parameters but with a longer scan time. Contour plots were compiled using grazing incidence X-ray diffraction (GI-XRD) data smoothed by adjacent averaging method to reduce noise in the low intensity regions. Lattice constants were calculated from the peak positions of the XRD diagrams using Rietveld refinement.

X-ray photoelectron spectroscopy (XPS) was utilized to identify atomic concentrations in the LLZO film, as well as to assign corresponding chemical states of the elements. The measurements were carried out at RT with monochromatized Al K α X-ray source (PHI Quantum 2000) on LLZO with the different Ga concentrations. In order to obtain a high number of counts for low elemental concentrations, the spectra were acquired with 117.4 eV pass energy, where the full width at half maximum (FWHM) is ~ 1.8 eV. The X-ray spot size was 150 μm . Sputter depth-profiling was necessary to obtain a more accurate representation of the bulk properties of the film, as surface layers are known to form upon contact with air, such as Li₂CO₃. Sputtering was done using an Ar⁺ ion sputter gun, at acceleration voltage of 2 kV and total sputtering time 45 min. The spectra for quantification of the films were selected from the middle of each film, where the signals for La and Zr are either at a maximum or in the middle of a plateau, see later in Fig. 3.7. The effects of preferential sputtering and forward sputtering may change the stoichiometry of the film surface. In addition, the matrix effect for each element in LLZO is not known, however a valid comparison between measured elemental signals can be made under the assumption that the matrix effects are similar for each film. Therefore, the values presented from XPS analysis are not absolute values and only relative comparison is valid. The error is estimated to be in the order of $\sim 10\%$. Spectra were fitted with Gaussian-Lorentzian mixed function and atomic concentrations were evaluated using empiric relative sensitivity factors of the equipment.

In-plane electrochemical impedance spectroscopy was performed using a Zahner (IM6) impedance bridge with a Linkam stage (HFS-600E, UK) containing a 2-point probe electrode geometry of gold coated tungsten tips. Measurement parameters included an AC voltage of 50 mV, a frequency range between $1 \times 10^6 - 0.1$ Hz and a flow of 50 sccm synthetic air to prevent reactions with moisture and CO₂ which are known to occur with LLZO.¹²⁶ Temperature was measured with a thermocouple in contact with the substrate surface. Au top contacts with 100 nm thickness, 7.5 mm width and a separation of 250 μm were deposited *via* thermal evaporation. Zview was used for data processing including data validation using the Kramers-Kronig test. In order to ensure reliability of the data, measurements were carried out over several heating-cooling cycles. The first heating/cooling cycle yielded large differences in conductivity depending on whether the sample was being heated or cooled. Performing further cycles under the same conditions resulted in more consistent results therefore the data for the quantitative analysis was extracted from the second cooling step for all films.

3.3 Results and Discussion

3.3.1 Lithium lanthanum zirconate thin films co-sputtered with lithium oxide

As-deposited films prepared by RF-magnetron co-sputtering from LLZO and Li_2O targets reveal an amorphous structure, shown in Fig. 3.2. After deposition of the films at RT and annealing at 700°C for 2 hours, the films prepared without the extra addition of Li from a Li_2O target crystallized directly into the lithium free $\text{La}_2\text{Zr}_2\text{O}_7$ phase as shown in Fig. 3.3a. (top pattern). The addition of extra lithium from the Li_2O target promoted the formation of the cubic LLZO phase (ICSD 422259) while dwelling at 700°C during the annealing phase (Fig. 3.3a middle pattern). No secondary binary, or ternary, lithium free phases are detected in such prepared films. After cooling the sample to RT the structure reverted back to the tetragonal LLZO phase (ICSD 246817) as illustrated in Fig. 3.3a in the bottom pattern. This transition back to tetragonal LLZO is expected to occur as there is no element added to stabilize the cubic phase at RT.¹³³

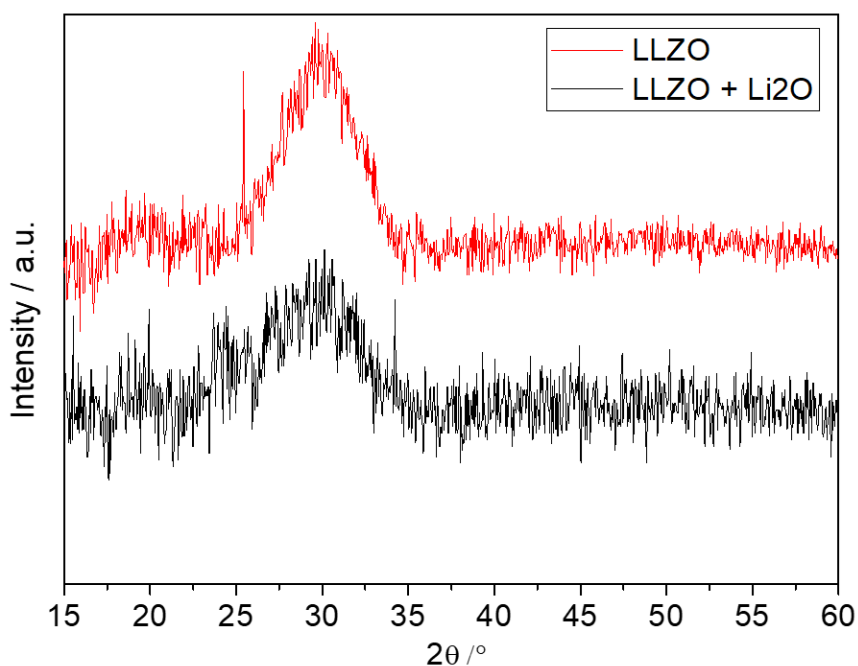


Fig. 3.2 Grazing incidence XRD of typical as-deposited thin films of LLZO and LLZO co-sputtered with Li_2O . Incidence angle $\omega = 1^\circ$. A broad reflection is observed between 2θ of 25° - 35° for both films.

The phase evolution during annealing of the film prepared by co-sputtering from LLZO and Li_2O targets is presented in Fig. 3.3b in an intensity contour plot made from a compilation of GI-XRD data. The corresponding temperature-time profile of the annealing process is shown on the right hand side. The contour plot starts at 300°C and the temperature is increased in 100°C intervals with a dwell time of 1 hour at each step for GI-XRD measurements to observe possible changes in the crystal structure. At 300°C some crystalline material had already formed

which could indicate the formation of $\text{Li}_4\text{Zr}_3\text{O}_8$ (JCPDS 01-041-0324) and Zr_3O (JCPDS 01-074-1282), although not enough peaks are present for a clear assignment. A comparison of this diffractogram with the two reference patterns is shown in Fig. 3.4. A broad reflection is also observed centered around 2θ of 30° signifying that some portion of the film is still amorphous. Upon annealing to a temperature of 500°C additional peaks are measurable which can all be ascribed to the tetragonal LLZO phase. A maximum intensity of the peaks corresponding to the tetragonal phase of LLZO is measurable upon reaching 600°C . During the dwelling period at 600°C the peaks corresponding to cubic LLZO gradually increase in intensity until the 3-hour mark after which no further changes occur signifying that equilibrium between both phases is reached. Further annealing to 650°C results in cubic LLZO dominating as the primary phase and by 700°C a complete transition from tetragonal to the cubic phase has occurred.

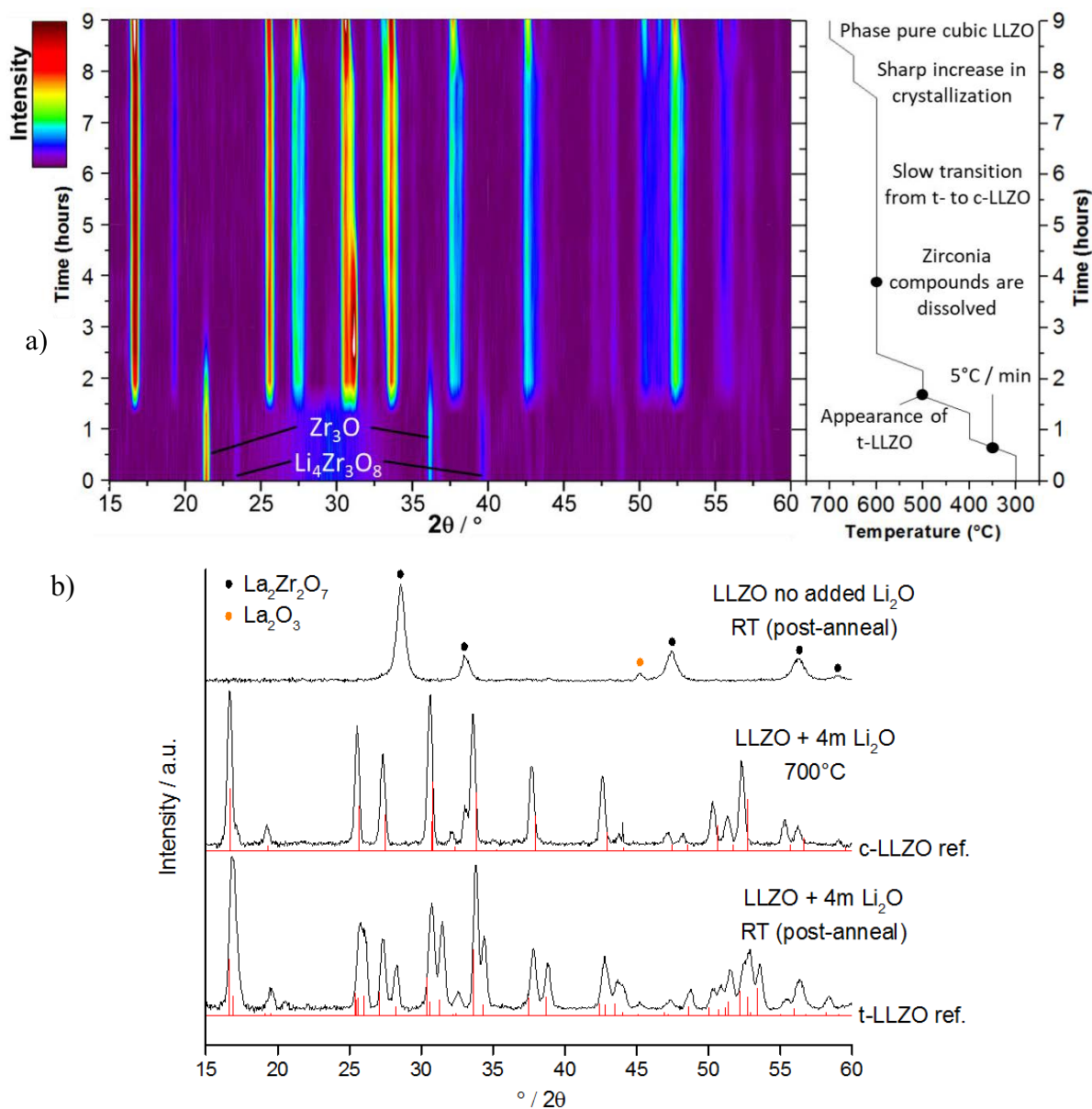


Fig. 3.3a) XRD of LLZO film with no additions after annealing at 700°C compared to film co-sputtered with Li₂O XRDs at 700°C in-situ and then post-annealing. Reference patterns for cubic and tetragonal LLZO are from the ICSD database, (ICSD 422259) and (ICSD 246817) respectively. **b)** Phase evolution of co-sputtered film LLZO + Li₂O showing transition from tetragonal LLZO to cubic LLZO at 600°C. To the right is the temperature-time profile of the annealing process with phase annotations. The ramp rate for heating/cooling was 5°C / min.

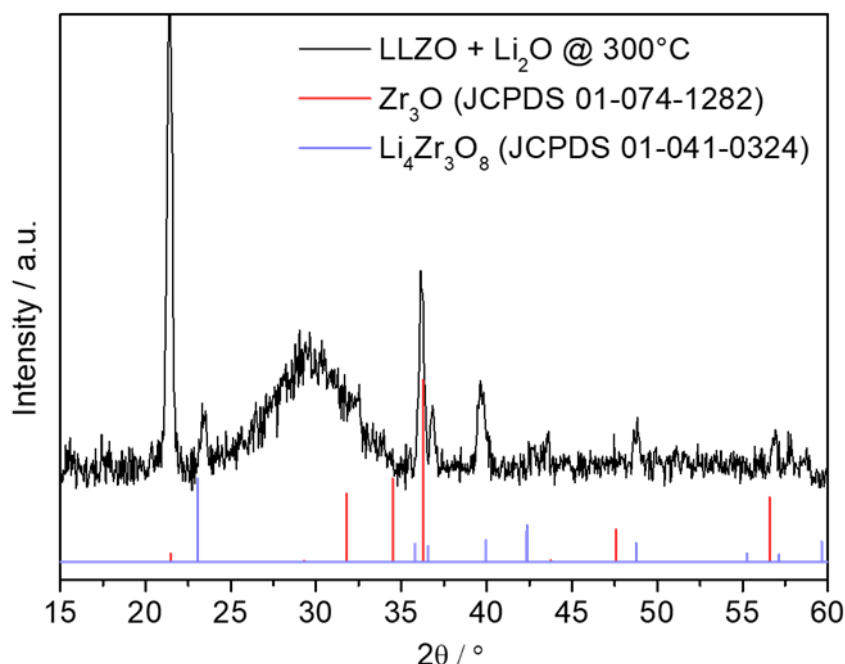


Fig. 3.4 XRD LLZO + Li₂O co-sputtered film at 300°C. Two possible matches are Zr₃O and Li₄Zr₃O₈, however there is a high degree of uncertainty.

3.3.2 Gallium alloying of lithium lanthanum zirconate thin films co-sputtered with lithium oxide

In order to dope the structure with Ga, six interlayers of Ga₂O₃ were sputtered in between the LLZO + Li₂O films at RT. Four multilayer stacks with varying Ga₂O₃ layer thicknesses were deposited, targeting the nominal gallium concentrations (x_{Ga}) in the compound Li_{7-3x}Ga_xLa₃Zr₂O₁₂ of $x_{\text{Ga}} = 0.2, 0.18, 0.16$ and 0.14 . In the following, the films with different Ga concentration are labelled according to the nominal (targeted) composition. As the post-annealing process for each film proceeds, XRD is carried out periodically and converted into intensity contour plots shown in Figs. 3.5a-d. An altered temperature profile is used which rises to 500°C quickly then dwells for an hour at each subsequent 50°C step up to 700°C, as shown in the temperature profiles to the right of each figure.

For all Ga doped films there were no diffraction peaks recorded at RT and diffraction peaks start to emerge at 300°C. From this point onwards the crystallization process differs between each film with different nominal Ga content, which we will discuss in detail through the following:

Ga:LLZO thin film with $x_{\text{Ga}}=0.20$:

In the GI-XRD diagram of the LLZO film with $x_{\text{Ga}} = 0.20$ (Fig. 3.5a) the first peak is observed at 400°C at $2\theta=31.5^\circ$. This peak indicates the formation of ZrO₂ with a baddeleyite structure type (JCPDS 00-037-1484), however, it must be noted that lack of additional peaks does not allow unambiguous assignment. At 500°C the main peaks of the cubic LLZO are already clearly visible, at $16.8^\circ, 25.8^\circ, 27.7^\circ, 31^\circ, 34^\circ, 38.2^\circ, 43.2^\circ$, and an additional three peaks between 50° - 54° . In addition, a peak at 29.8° appears that could be assigned to the ZrO₂ (101) peak (JCPDS 01-079-1763). Upon reaching 600°C the diffraction peaks of the

intermediate phases begin to fade. At this temperature tetragonal LLZO is also formed which can be most clearly observed in the partial splitting of the peak at 37.8° and the triple peaks between 50° - 54° becoming more broad; a conventional XRD is shown in Fig. 3.6 to highlight this development. Heating to 650°C causes the peaks at 29.8° and 31.5° to fully disappear while there is a strong increase in LLZO peak intensities and a complete transition to the cubic phase. Additional peaks with low intensity at 23.6° and 21.5° become visible which fit well to the Li_5GaO_4 phase (JCPDS 00-024-0613). The final annealing step at 700°C caused a further increase in peak intensities of the cubic LLZO phase indicating on-going grain growth.

Ga:LLZO thin film with $x_{\text{Ga}}=0.18$:

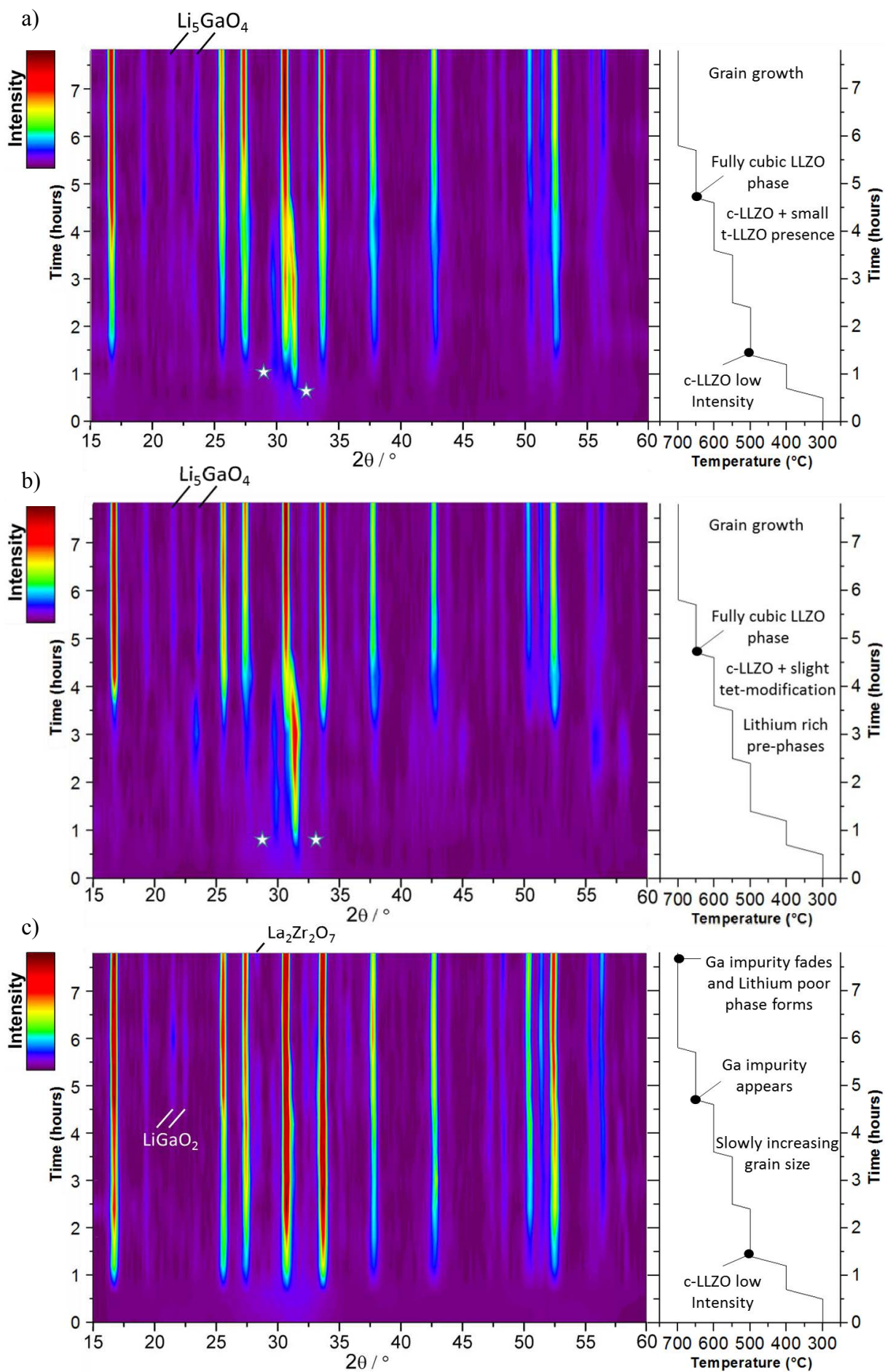
Fig. 3.5b shows the phase evolution for the Ga:LLZO thin film with $x_{\text{Ga}}=0.18$. Similarly, as in the previous case, peaks at 29.8° and 31.5° which indicate ZrO_2 formation appear at 400°C . However, no diffraction peaks corresponding to cubic LLZO are detected at 500°C . Instead, at 550°C a combination of peaks appears which originate from several precursor phases including $\text{La}_4\text{Ga}_2\text{O}_9$, Li_4ZrO_4 and Li_5GaO_4 . At 600°C all diffraction peaks of the ternary intermediate phases fade. The main features correspond to cubic LLZO with some tetragonal LLZO content most visible as a broadening of peaks in the 50° - 54° range and splitting in the peaks at 38.2° and 43.2° . At 650°C the full transition of LLZO to the $I43d$ cubic phase occurs with a small secondary phase peak at 23.6° which may correspond to Li_5GaO_4 . At 700°C there is an increase in peak intensities indicating grain growth.

Ga:LLZO thin film with $x_{\text{Ga}}=0.16$:

The Ga:LLZO layer with $x_{\text{Ga}}=0.16$ directly crystallizes into cubic LLZO at 500°C (Fig. 3.5c). No intermediate crystalline material or phase is observed. All peaks corresponding to cubic LLZO undergo continuous increases in intensity as the temperature increases. At 700°C there is appearance of peaks at 21.5° and 22.5° likely corresponding to LiGaO_2 (ICSD 01-072-1640). These peaks become lower in intensity during the dwell at 700°C signaling a possible absorption of Ga into the LLZO crystal structure. Towards the end of the dwell at 700°C an additional peak at 28° begins to appear which matches the primary peak of the lithium deficient $\text{La}_2\text{Zr}_2\text{O}_7$ phase (ICSD 01-075-0346). This indicates that lithium loss is occurring.

Ga:LLZO thin film with $x_{\text{Ga}}=0.14$:

This layer shows a similar phase evolution as the layer with $x_{\text{Ga}}=0.18$ as seen in the late crystallization of LLZO at 600°C and the same intermediate phases forming at 550°C (Fig. 3.5d). The only significant difference is the lower quantity of Ga containing secondary phases in the final XRD at 700°C .



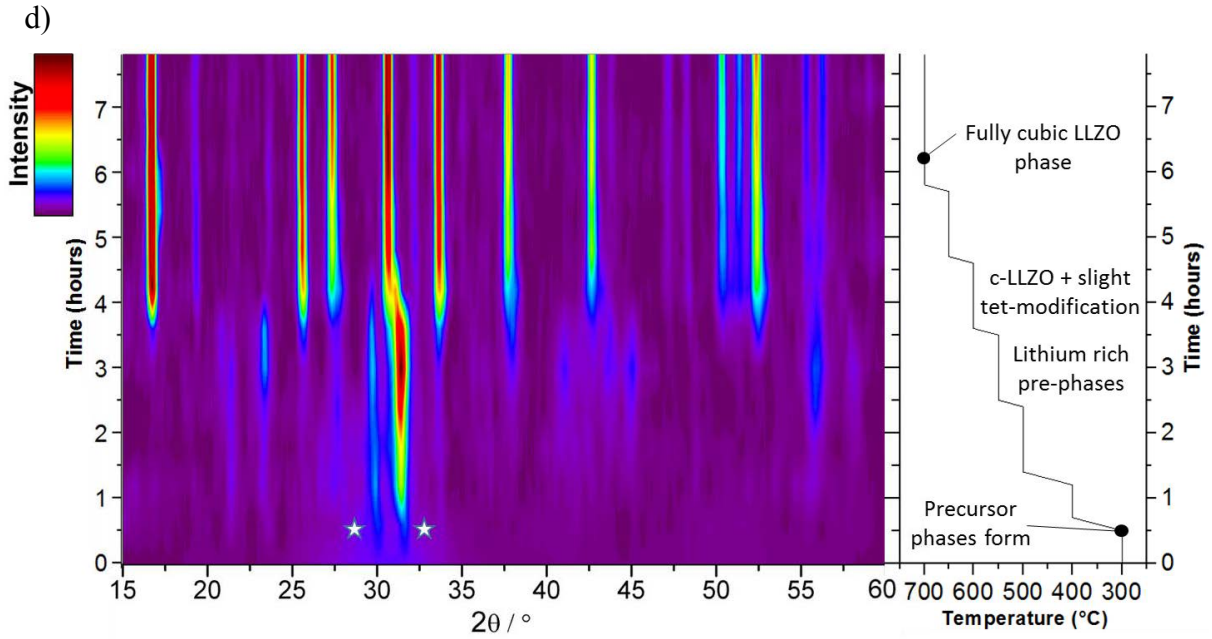


Fig. 3.5 Phase evolution of films with Ga concentrations of a) 0.20 Ga b) 0.18 Ga c) 0.16 Ga d) 0.14 Ga with annotated temperature profiles to the right. All films crystallize into the cubic phase at $> 600^{\circ}\text{C}$. The star symbol is to label precursor phases with tentative assignment to ZrO_2 .

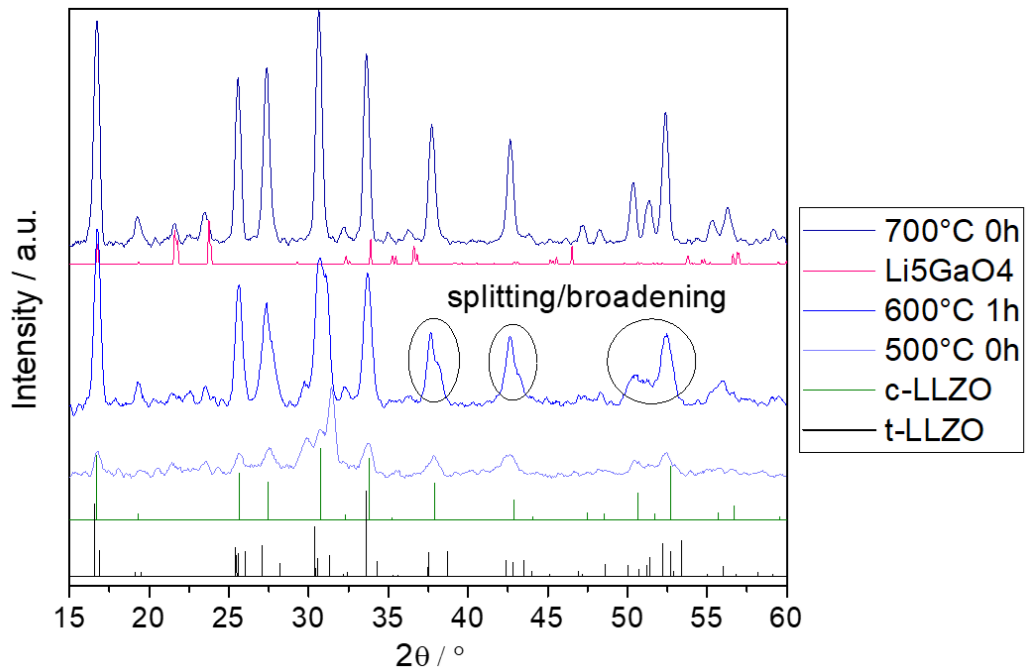


Fig. 3.6 XRD segments from intensity contour plot of film with 0.20 Ga showing the development of the LLZO phase over the course of the in-situ annealing.

The RT GI-XRD pattern for each film after annealing up to 700°C is shown in Fig. 3.7 together with the LLZO layer without addition of Ga. A comparison between the Ga containing and Ga free films shows the clear effect of Ga on the stabilization of the cubic phase at RT. The layer with $x_{\text{Ga}} = 0.16$ shows a slightly preferred orientation with greater relative intensity for the two peaks between 30° - 35° corresponding to the (420) and (422) planes of cubic LLZO phase. The corresponding Lotgering factors are 0.09 and 0.06 respectively.¹³⁴ The lattice parameters, derived from Rietveld refinement, for each film from $x_{\text{Ga}} = 0.20$ to 0.14 are 12.953, 12.954, 12.989 and 12.954 Å, respectively. These values are lower than the previously obtained value of 12.971 Å for 0.25 Ga substituted bulk LLZO pellets⁸⁷ with the exception of $x_{\text{Ga}} = 0.16$ which is higher for unknown reasons. The difference between these values may be explained by thermally induced stresses due to the different coefficients of thermal expansion of the film and the substrate or microstrain. SEM of film and surface cross sections for $x_{\text{Ga}} = 0.20$ -0.14 are shown in Fig. 3.8

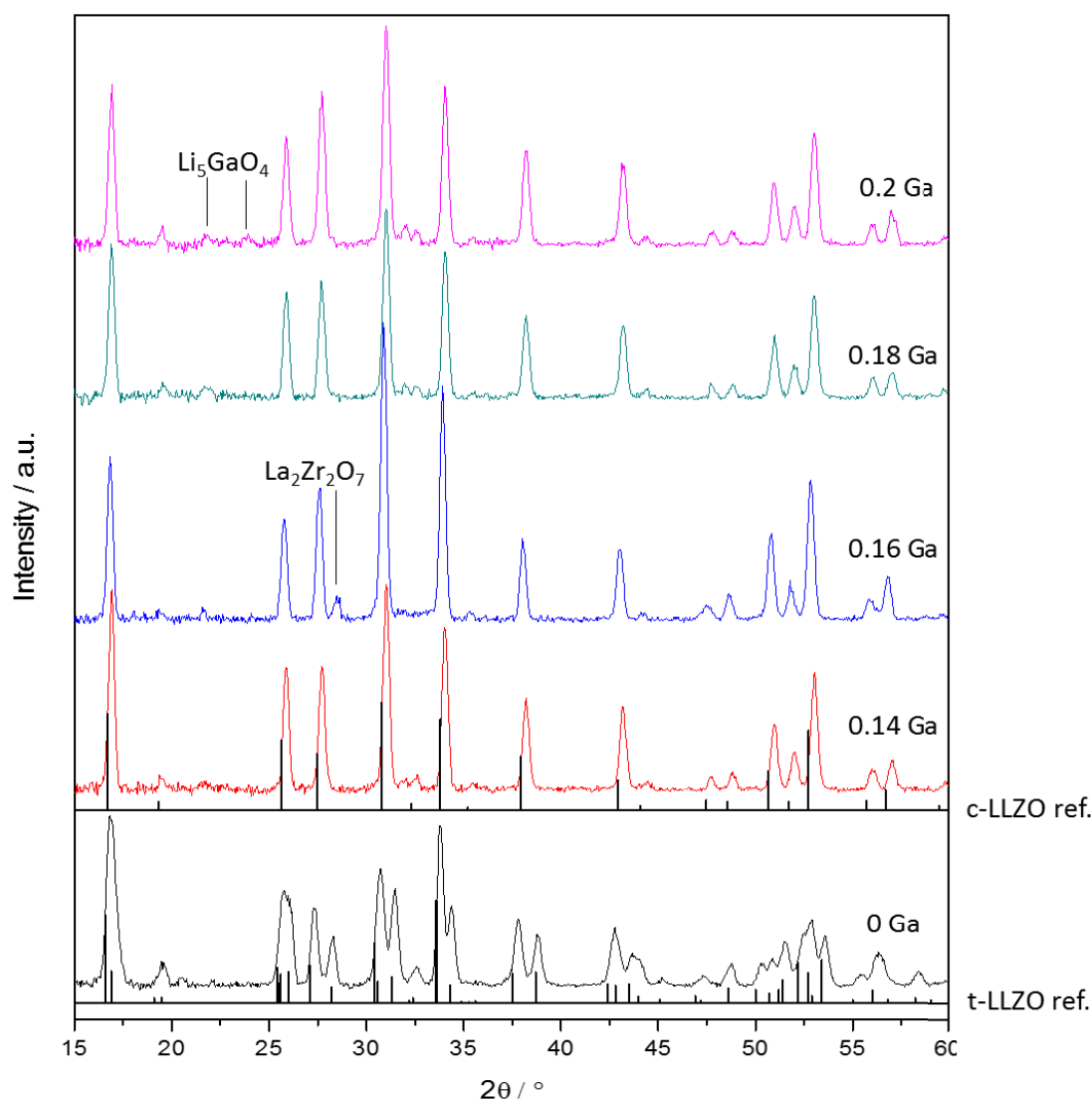


Fig. 3.7 RT XRD of thin films after thermal treatment with varying contents of Ga and Li. Reference patterns for cubic and tetragonal LLZO are from the ICSD database, (ICSD 422259) and (ICSD 246817) respectively.

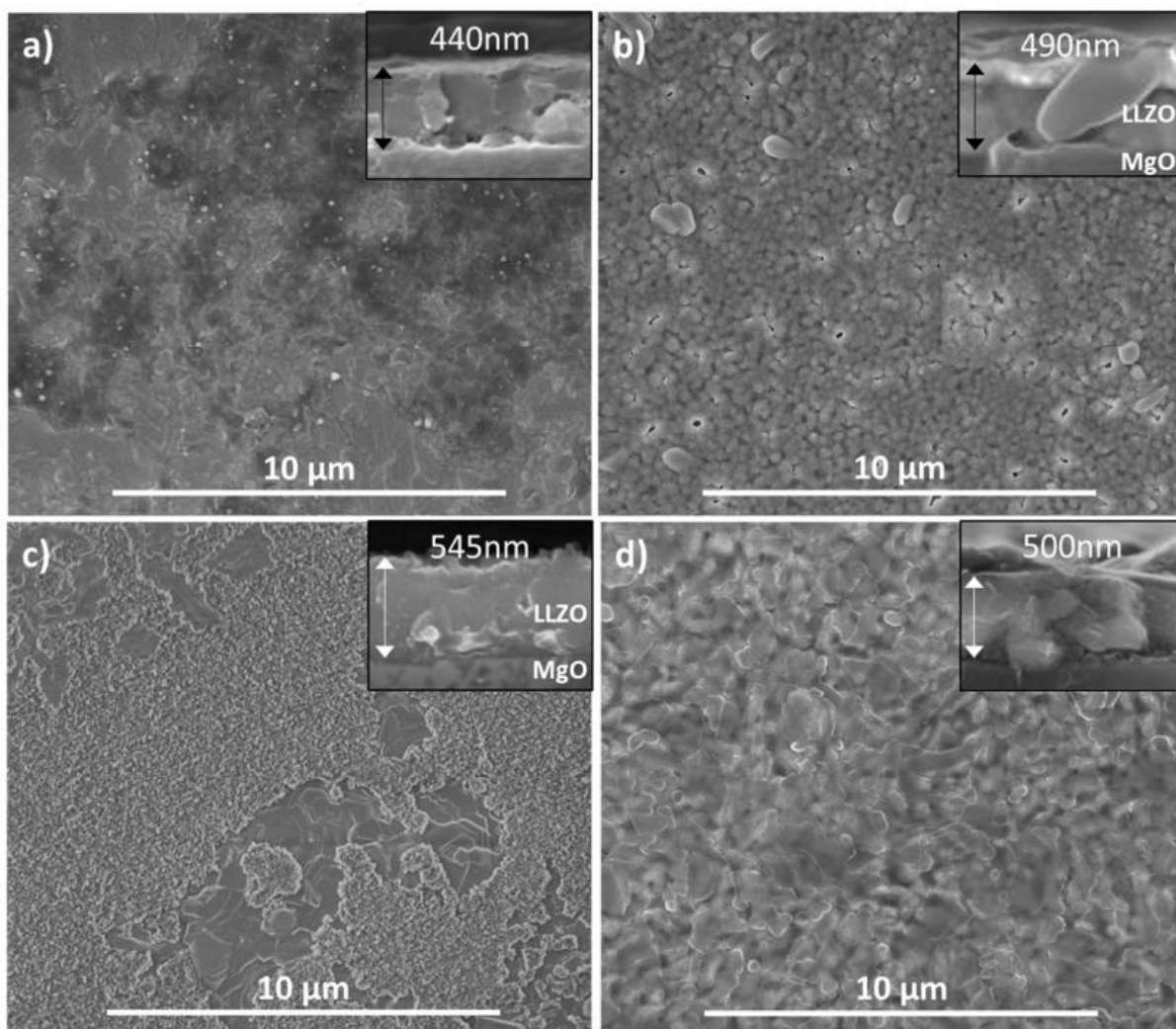


Fig. 3.8 top view and cross-section SEM of the films $x\text{Ga}$ = a) 0.2 b) 0.81 c) 0.16 d) 0.14. Cross-sections are obtained from freshly cleaved edges.

Although the XRD pattern that formed is not influenced by the different Ga contents within this range, the phase evolution particularly in the temperature range from 300°C to 600°C showed a strong dependence.

Now to probe the chemical composition, XPS depth profile measurements were conducted on the same films after the annealing at 700°C, and a representative XPS scan taken from the center of each film where relative La and Zr content reaches a maximum plateau, as illustrated in Fig. 3.9. All XPS spectra were charge corrected with respect to the La 3d 5/2 photoelectron line position for La_2O_3 at 835.1 eV.(CAS registry number 1312818)

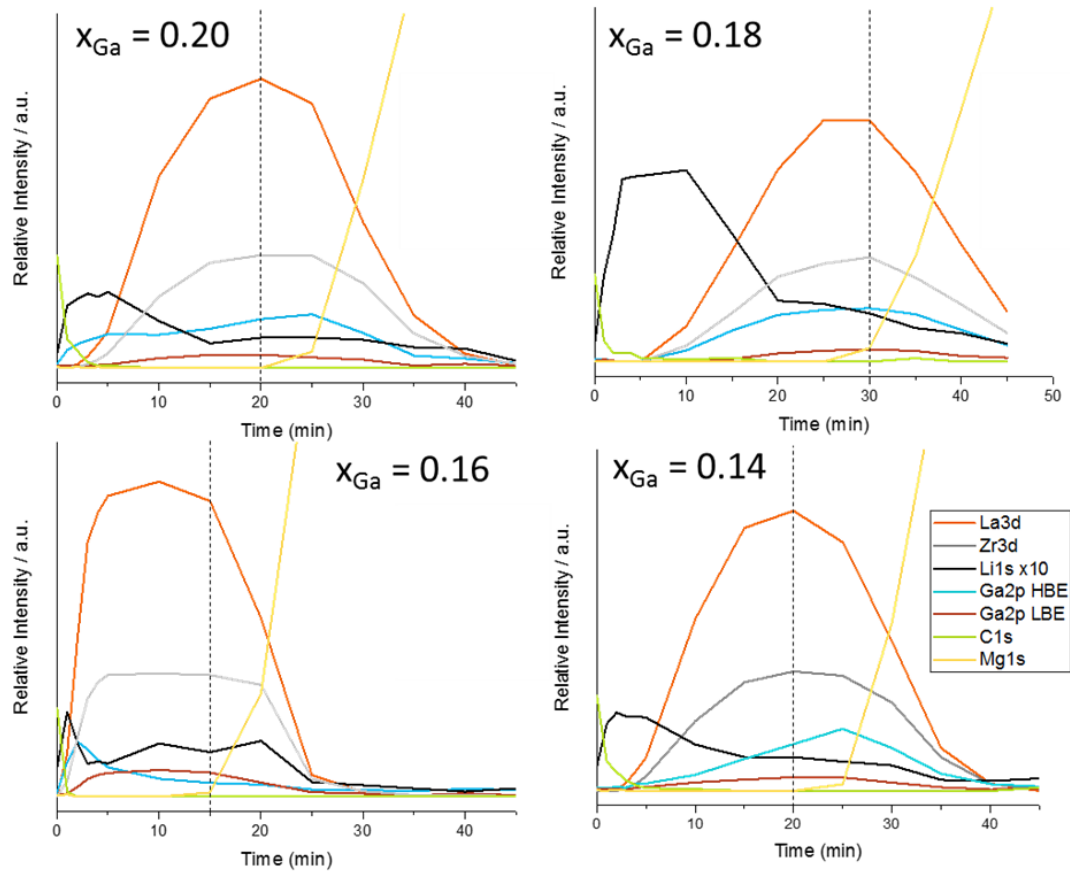


Fig. 3.9 Depth profile of respective peak intensities for $x_{Ga} = 0.14 - 0.20$ films for each element from XPS measurements. Due to the low yield of Li1s signal, the intensity has been increased by factor $\times 10$ for clearer observation. The dotted lines indicate at which point the detailed XPS analyses and quantification was carried out.

The Ga2p level contains two doublets, one with lower binding energies (BE) of 1116.7 eV for the 2p_{5/2} and 1143 eV for the 2p_{3/2} photoelectron line position, and a more dominant one with a shift of +2.3 eV having a 2p_{5/2} line at 1119 eV and 2p_{3/2} line at 1145.3 eV, see Fig. 3.10. On the basis of the maximum saturation of Ga in the LLZO lattice being in the region of 0.5 Ga per LLZO^{87,135} the minor doublet can be assigned to the Ga-O bond in the LLZO lattice and the dominant doublet to the Ga-O bond in either LiGaO₂, which is observed *via* XRD, or an amorphous, Ga rich phase which is expected to precipitate at the grain boundaries of LLZO.⁹¹ Fig. 3.10 also shows the Li1s signals for the 4 samples. Fitting the minimum number of peaks with a fixed FWHM of 2 eV, resulted in 2 different bonding energies at 53.9 eV and 56.2 eV. There is no overlap of Li1s with Mg peaks from the substrate as no Mg was detected at this depth. The spectra and corresponding fits used for quantification of La3d, Zr3d and O1s can be found in Fig. 3.11.

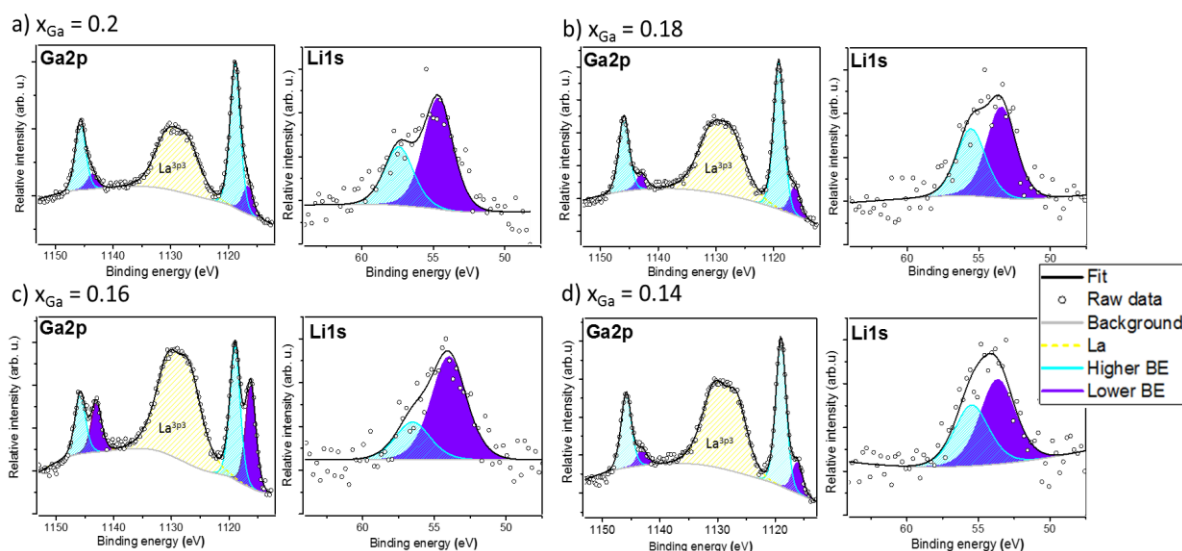


Fig. 3.10 XPS spectra of Ga 2p and Li 1s orbitals for gallium doped samples. Two bonding environments are observed for both elements indicating the presence of a second phase in the thin films. The outlier point in the Li1s spectrum in a) is later removed for an improved fit as described in Table S7.1.

In Table S7.1 the 4 different Ga concentrations, as estimated from the quartz crystal microbalance, are compared to the elemental values determined by XPS. Errors in the elemental concentration between different binding energies is expected to be in the order of 10% when operating at high pass energies of 117.4 eV. There is a relatively higher proportion of Ga in all films, however, an overall trend of decreasing gallium content from films $x_{\text{Ga}} = 0.20$ to 0.14 is still observed.

Element	Orbital	BE (eV)	Predicted x_{Ga}			
			$x_{\text{Ga}} = 0.2^*$	$x_{\text{Ga}} = 0.18$	$x_{\text{Ga}} = 0.16$	$x_{\text{Ga}} = 0.14$
Ga	2p _{3/2}	1116.7	0.24	0.23	0.58	0.2
	2p _{3/2}	1119.0	1.23	1.16	0.73	0.97
	total		1.47	1.39	1.31	1.17
Li	1s	53.9	8.32/5.54	5.01	6.85	5.35
	1s	56.2	4.41/3.15	3.70	2.52	3.86
	total		12.73/8.64	8.71	9.37	9.21
Zr	3d _{5/2}	total	2.42	2.08	2.28	2.19
La	3d _{5/2}	total	3	3	3	3

Table 3.1 Relative elemental concentrations as calculated by XPS for each sample with nominal Ga contents between 0.20 - 0.14. Values are normalized around La content, which is set to 3 for each sample for comparison to the expected formula: $\text{Li}_7\text{La}_3\text{Zr}_2\text{O}_{12}$. *Removing the outlier over the Li1s peaks in Fig. 3.9a results in lower lithium values for both BEs.

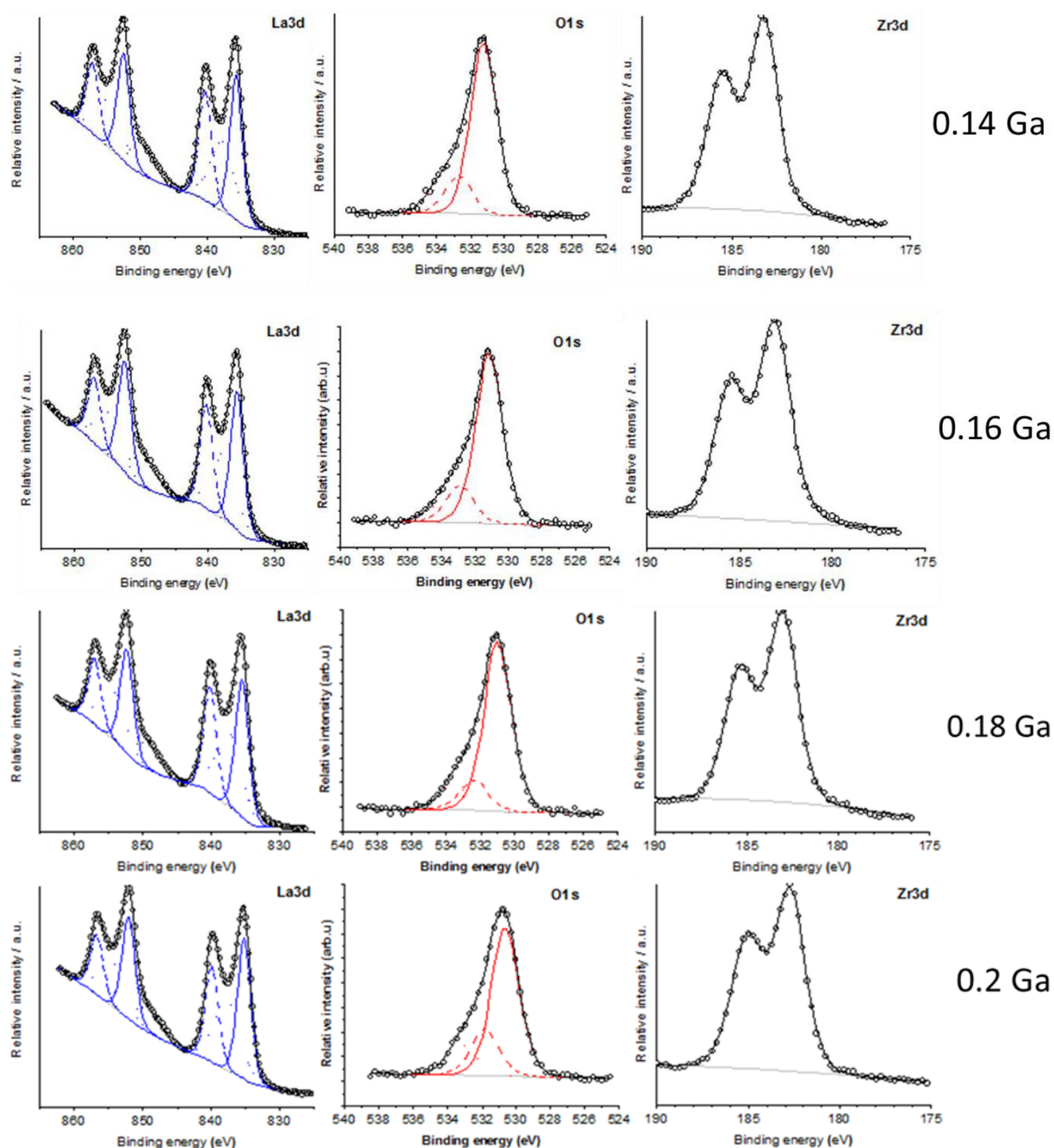


Fig. 3.11 XPS spectra of La3d, O1s and Zr3d orbitals for gallium doped samples. The bonding environments do not change significantly for these elements as the gallium concentration is altered. The La 3d peak was fitted by 3 doublets with fixed FWHM and distance.⁷ However intensities of components were left free, as they vary depending on the hybridization of the orbitals⁸ and chemical composition of the La compound.^{9,10} The energy position of the first La3d doublet is 835.2 eV. Zr3d was fit with the doublet, peak at lower BE is at 182.7 eV

By plotting the concentrations derived from the two components at lower BE for Li and Ga for each sample certain trends may be seen, as shown in Fig. 3.12. The lower BE components of Li and Ga correlate well across all samples therefore the 53.9 eV Li1s peak can be assigned to LLZO. The higher BE components also correlate well indicating that they belong to the same chemical compound which could be an amorphous secondary phase. Relative to the apparent Ga content in the films, the Li content is lower than expected. This may be caused by the presence of O^{2-} vacancies which each result in the loss of $2 Li^+$ from the structure. The presence of oxygen vacancies in LLZO was recently proven by Kubicek et. al.⁹⁵ There is currently no explanation for why the Ga content in the LLZO was not at its limit for all films despite its overall abundance. The most notable connection linking the early crystallization of LLZO and the chemical content of the films is the relatively higher lithium and gallium contents of the $x_{Ga}=0.20$ and 0.16 films.

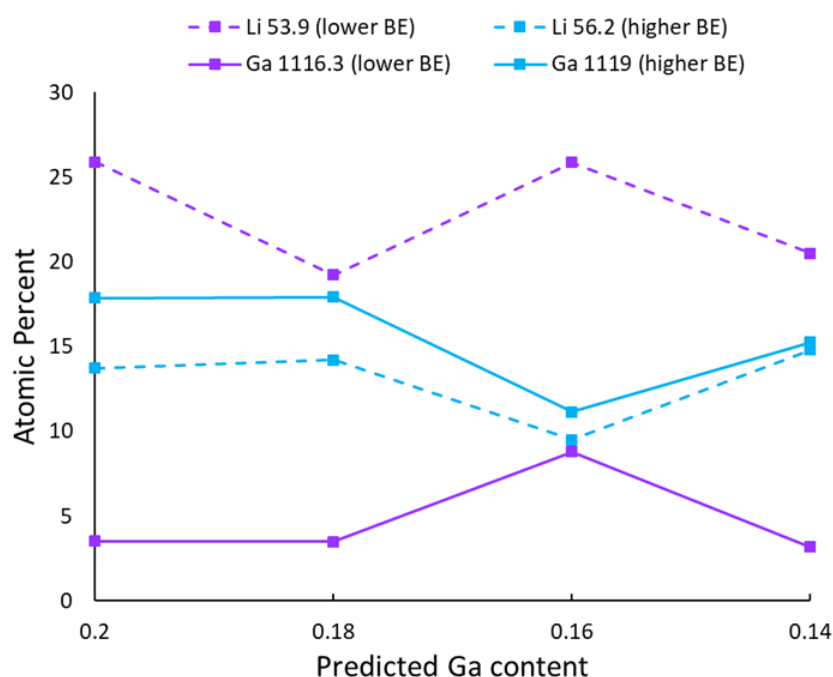


Fig. 3.12 Trends in atomic percent of 2 chemical states (violet - lower BE, blue - higher BE) of Li 1s and Ga 2p across 4 samples. A correlation is observed between both lower BE states and both higher BE states allowing these states to be assigned to the same phases.

3.3.3 Electrochemical impedance spectroscopy analysis of lithium lanthanum zirconate thin films

Impedance spectroscopy carried out over three heating/cooling cycles was employed to determine the (in-plane) ionic conductivity of the annealed thin films. Discrepancies over the course of three heating cycles is shown in Fig. 3.13. Such differences in measured conductivity between the first and second cycles could be related to the contact between the gold electrode and the film. An improved contact with the gold electrode could be established after the first heating due to the alloying of lithium with gold, which is a known phenomenon.¹⁴⁰ The Kramers-Kronig test¹⁴¹ was carried out for all temperatures to verify the self-consistency of the impedance data, an example of which is shown for $x_{\text{Ga}} = 0.18$ in Fig. S7.1.

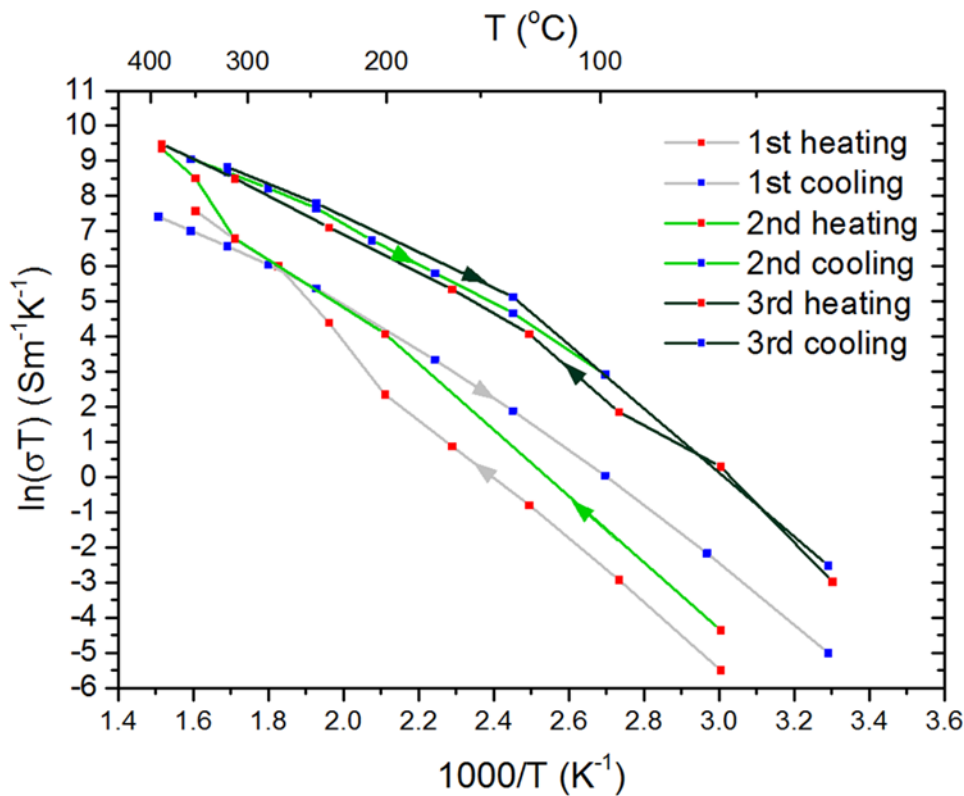


Fig. 3.13 Conductivity measurements for film with 0.18 Ga over the course of three heating and cooling cycles. Conductivities were calculated via *R-CPE* circuit fitting.

The dc-conductivity was extracted from both the impedance and the electric modulus plot in order to check for consistency. This is required as the Nyquist fit methods bear the inconvenience of having parameters not clearly related to the physics of the sample and the fit is dominated by the large impedance (low frequency) data mostly affected by polarization effects. In order to obtain more reliable estimates and to check the errors introduced with the previous models we employed the electric modulus, M^* , formalism.¹⁴² M^* is calculated directly from the measured impedance as

$$M^* = \frac{1}{\epsilon^*} = M' + jM'' = j\omega C_0 Z^*$$

In the above definition M' and M'' are the real and imaginary components of M^* , ε^* is the complex permittivity, $j = (-1)^{1/2}$, $\omega = 2\pi\nu$ as the angular frequency and $C_0 = \varepsilon_0 A/d$ as the geometric capacitance where $\varepsilon_0 = 8.85 \times 10^{-12}$ F/m is the permittivity of free space, A is the cross-sectional area of the thin film and d is the distance between the electrodes. The fits for both methods are shown in Fig. 3.14, note that the low frequency data appears at the origin of the M'' vs M' plot and therefor has less weight on the analysis. In order to derive the ionic conductivity from the electric modulus plot we make use of the definition for ε^* as:

$$\varepsilon^* = \varepsilon' - j \frac{\sigma}{\varepsilon_0 \omega}$$

The real and imaginary components of M^* can then be expressed as:

$$M' = \frac{\varepsilon}{\varepsilon^2 + \left(\frac{\sigma}{\varepsilon_0 \omega}\right)^2} \quad M'' = \frac{\frac{\sigma}{\varepsilon_0 \omega}}{\varepsilon^2 + \left(\frac{\sigma}{\varepsilon_0 \omega}\right)^2}$$

When M' is at high frequencies the term $\sigma/\varepsilon_0 \omega$ tends to 0 therefore the function reduces to $M'_{\text{intercept}} = 1/\varepsilon$, and when M'' is at a maximum the following relation is valid:

$$\varepsilon = \frac{\sigma}{\varepsilon_0 \omega_{\text{max}}}$$

Therefore the conductivity can be calculated with the following equation:

$$\sigma = \frac{\varepsilon_0 \omega_{\text{max}}}{M'_{\text{intercept}}}$$

A comparison of the conductivity values extracted over the full temperature range from the two methods is shown in figure 3.14.

The conductivities for the Ga doped films at RT for $x_{\text{Ga}} = 0.20, 0.18, 0.16$, and 0.14 are 1.2×10^{-6} , 2.7×10^{-6} , 6.9×10^{-7} and 3.0×10^{-6} S cm⁻¹ respectively. Comparing these results to the XPS measured elemental compositions it appears that higher levels of Ga in the LLZO may cause lower conductivities at RT. The initial measurement of film $x_{\text{Ga}} = 0.14$, before high temperature measurements was carried out, shown in Fig. 3.14 yielded a conductivity of 1.6×10^{-5} S cm⁻¹ although the conductivity quickly degraded with successive measurements in O₂ atmosphere before stabilizing almost one order of magnitude lower. This initial value for polycrystalline cubic LLZO was comparable to what has been obtained for epitaxially grown LLZO thin films.⁹⁶

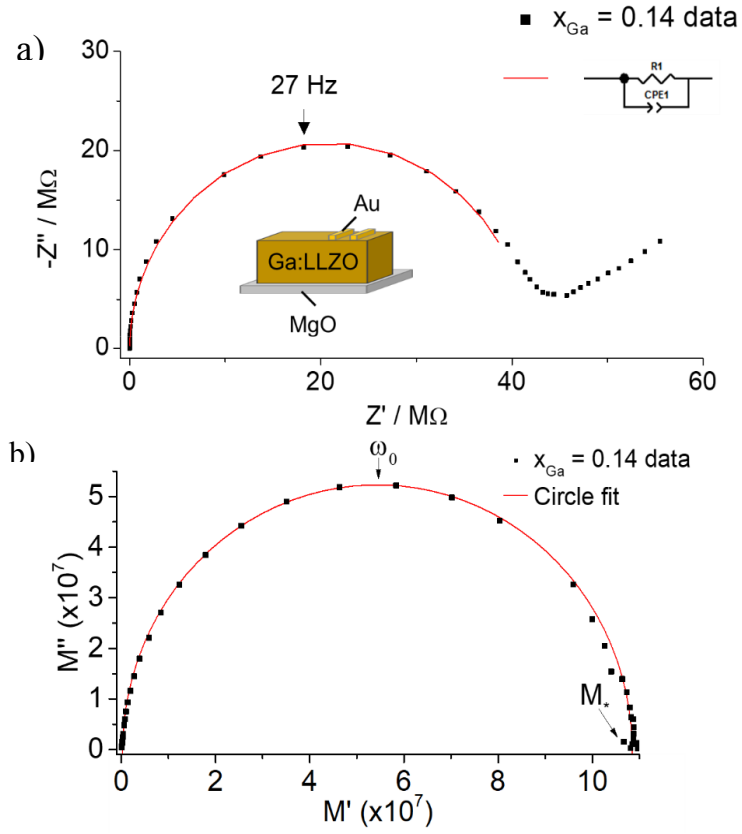


Fig. 3.15) Nyquist plot for electrochemical impedance spectroscopy (EIS) measured at 50°C for LLZO film with 0.14 Ga resulting in a conductivity of $1.6 \times 10^{-5} \text{ S cm}^{-1}$. An R-CPE equivalent circuit model is used to fit the data. b) Plot of the complex electric modulus of the same film with key variables for calculating ionic conductivity labelled.

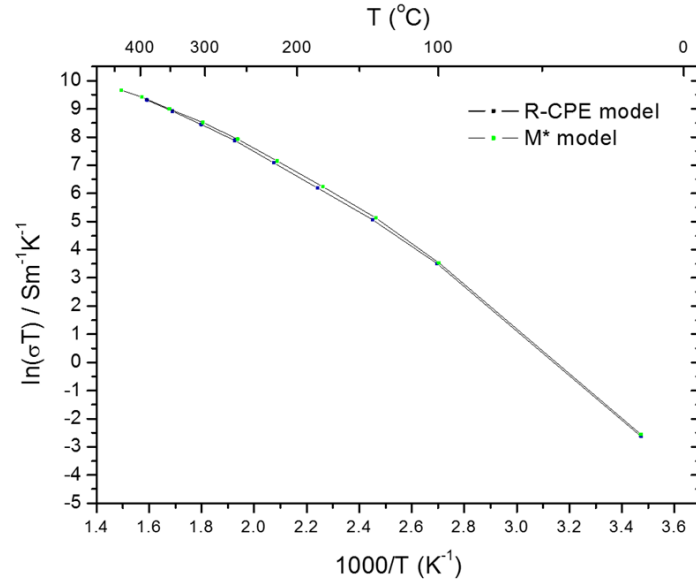


Fig. 3.14 Arrhenius plot of $x_{\text{Ga}} = 0.18$ film ionic conductivity from impedance and electric modulus analysis presented in Fig. 3.13.

The temperature dependence of the conductivity is shown in Fig. 3.16 over the range from 400°C to RT. References are included from previous research on thin film LLZO.^{96,98,99,101,103,104,135} A smooth deviation from the Arrhenius behavior is observed for all investigated samples, with the plot of conductivity in logarithmic scale vs inverse of temperature not being a straight line. The increase of the activation energy (the slope) as the temperature is decreased, is a commonly observed feature in ionic conductors. Generally, the first approach for interpreting such a feature is to fit the curve to an appropriate number of activation energies that represent different conductivity mechanisms in the material. In this case the data was fit with two activation energies using the general expression from linear response theory over the full temperature range, as described in the supporting information, which gives us apparent activation energies $E_1 = 0.66 \pm 0.03$ eV and $E_2 = 0.38 \pm 0.03$ eV. Although the data can be fit this way, it is unclear which conductivity mechanism would yield an activation energy of 0.66 eV in LLZO. On the other hand, E_2 matches well with the expected value for bulk LLZO lithium-ion conductivity.⁸⁹

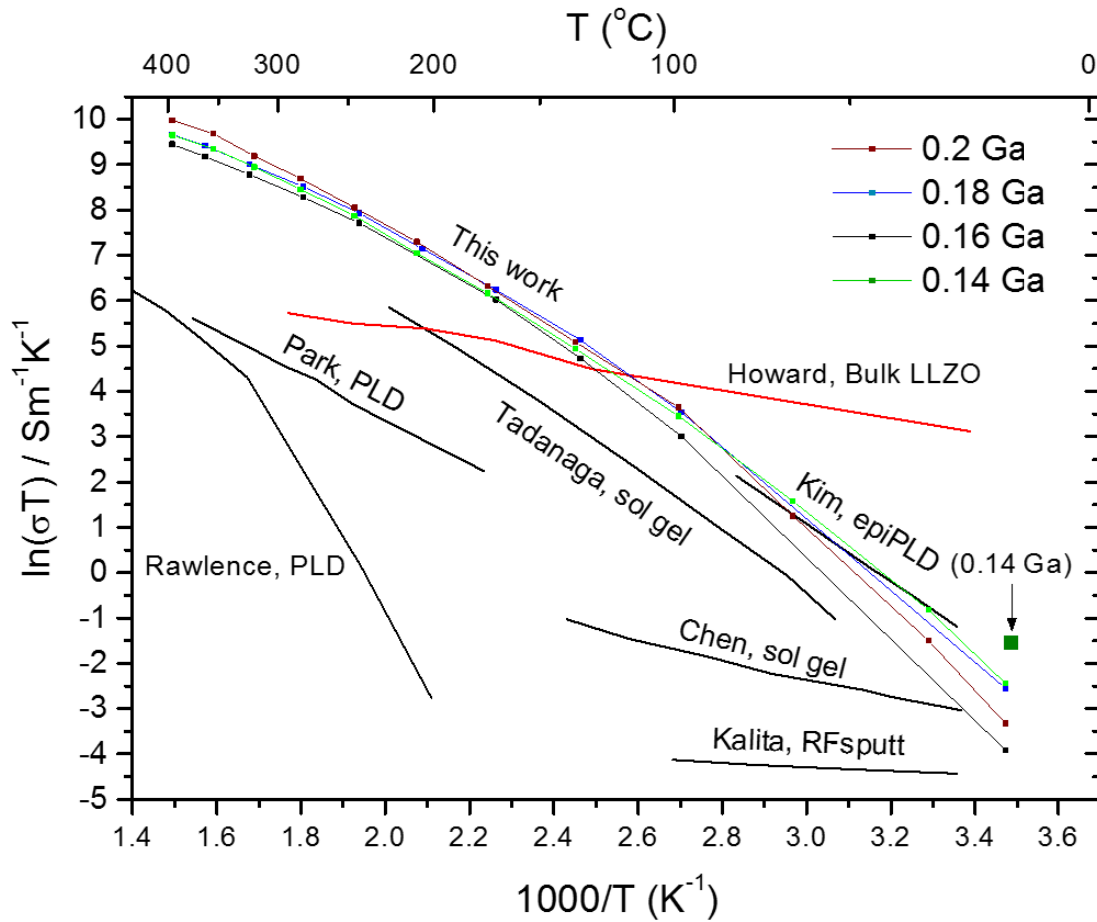


Fig. 3.16 Arrhenius type plot for LLZO films with 0.20, 0.18, 0.16 and 0.14 Ga concentrations. Initial high conductivity measurement of 0.14 Ga film shown in Fig. 6a plotted as a single point. Other reference data for thin film LLZO from literature were Kim et. al.⁹⁶, Rawlence et. al.⁹⁸, Park et. al.⁹⁹, Kalita et. al.¹⁰¹, Tadanaga et. al.¹⁰³ and Chen et. al.¹⁰⁴. Howard et. al.¹³⁵ shows data obtained from a pellet of LLZO doped with 0.5 Ga per unit cell.

Further analysis of the physical implications of this approach (presented in detail in the supporting information) shows that there is a strong mismatch of 1.28×10^4 in the ratio between the jump-attempt frequencies connected to E_1 and E_2 . Both these values should be close to the lattice vibrations (normally $\sim 10^{15}$ Hz). The ion-ion correlation effect is capable of explaining deviations from the Arrhenius behavior, we refer here to ref. ⁵⁷ for details. It was also used in relation to crystalline lithium-ion conductors.⁵⁸ By fitting the data with the coupling model (See in chapter 3 supporting information) that makes use of a single temperature-independent activation energy, which is determined by the lattice energy barriers, a value of $E_a = 0.35 \pm 0.02$ eV is obtained. In Fig. S7.2 the temperature dependence of the effective activation energy due to correlation effects is presented in further detail.

3.4 Conclusion

Herein we demonstrate co-sputtering followed by post-annealing as a promising approach for the formation of cubic-LLZO thin films with high lithium ion conductivity and thermal stability. Importantly, the issue of lithium loss during vacuum deposition and annealing is overcome by gaining control over the initial lithium content in the film. By incorporating Ga_2O_3 interlayers, the cubic phase is stabilized at RT with an initial lithium ion conductivity of $1.6 \times 10^{-5} \text{ S cm}^{-1}$ at RT that degrades down to $3.0 \times 10^{-6} \text{ S cm}^{-1}$ during high temperature conductivity measurements. Non-Arrhenius behavior was observed over a large temperature range and was modelled and discussed with the approach of the two-activation energy model as well as an ion-ion correlation model.

Through studying the effect of gallium content on phase evolution during annealing, a more in-depth understanding of the interplay between the precursor phases and desired LLZO phases has been gained, particularly in the case of LLZO with high Ga content. In the lower temperature region of the annealing process between 300 - 600°C the effect of the Ga content on the crystallization was particularly pronounced. The $x_{\text{Ga}} = 0.16$ and 0.20 films, with XPS measured Ga contents of 0.58 and 0.24 respectively, formed a low temperature cubic LLZO phase at 500°C whereas films with lower Li and Ga contents formed LLZO at 600°C. Synthesis of the desired cubic phase at these lower temperatures is of particular interest for later integrating such films into a full solid-state cell.

4 Chromium Nitride as Stable Cathode Current Collector for All-solid-state Thin Film Li⁺ ion Batteries

This chapter is based on the following publication:

A. N. Filippin,[‡] M. Rawlence,[‡] A. Wäckerlin, T. Feurer, T. Zünd, K. Kravchyk, M. Kovalenko, Y. E. Romanyuk, A. N. Tiwari, S. Buecheler, **RSC Advances**, 7, 26960-26967, 2016

[‡] Indicates co-first author

4.1 Introduction

In this chapter thin films of Cr_xN alloys are fabricated by pulsed DC magnetron sputtering, a deposition technique that allows high deposition rates and is industrially scalable, to show the transition point between CrN and Cr₂N. The compatibility of Cr₂N with the high voltage cathode LMNO is verified by high temperature post-annealing of LMNO thin films sputtered onto Cr₂N, followed by assembling and testing of coin cells comprising a LiPF₆-based liquid electrolyte and lithium foil as anode. These results pave the way for future efforts on replacing the liquid electrolyte with a suitable solid-state alternative for constructing all-solid-state batteries.

4.2 Experimental

Cr_xN thin films were deposited by pulsed DC magnetron sputtering of a chromium target (99.95% purity, Umicore) in a Balzers BAS 450 PM deposition system. The depositions were carried out at a pressure of 0.3 Pa on boron doped silicon (100) (Prime grade, University wafers), stainless steel coin spacers (16 mm diameter × 0.5 mm thickness, Grade 316L, Hohsen Corp.), soda lime glass (5 cm × 5 cm) and aluminum foil (25 μm thick, 99.45% – metals basis, Alfa Aesar) substrates, varying the Ar to N₂ ratio for each composition. Prior to each deposition both the substrates and the Cr target were pre-sputtered for 5 minutes in pure Ar followed by the poisoning of the target with an Ar to N₂ ratio of 3:18 (sccm) for 5 minutes. The target power used in all cases was 0.32 W cm⁻², the pulsing frequency was 100 kHz, the reverse time was 2 μs, the total pressure was fixed at 0.3 Pa, and the temperature of the substrates was fixed at 300 °C.

The deposition time for Cr₂N was tuned to obtain the desired thickness of approximately 500 nm with a rate of ~900 Å min⁻¹. Such a thickness was chosen to ensure a low resistivity of ~1.1 × 10⁻⁴ Ω cm. 500 nm thin films of Li_xMn_{1.5}Ni_{0.5}O₄ were deposited by RF magnetron sputtering as cathode material on Cr₂N(500 nm)/stainless steel (SS) and Cr₂N(500 nm)/Si for characterization, alternating layers of NiO (99.9% purity target, AJA International) and LiMn₂O₄ (99.9% purity target, Jiangyin Entret Coating Technology Co.) with additional layers of Li₂O (99.9% purity target, TOSHIMA Manufacturing Co.) to compensate for the lithium loss. The deposition process was carried out at 220 °C at a pressure of 0.05 Pa (Ar:O₂ ratio of 24:1), the RF power of the LiMn₂O₄, NiO and Li₂O targets was 1.23 W cm⁻², 0.47 W cm⁻² and 1.23 W cm⁻², respectively, yielding a deposition rate of 8.5 Å min⁻¹ (LiMn₂O₄), 0.75 Å min⁻¹ (NiO) and ~3 Å min⁻¹ (Li₂O). The deposition time of Li₂O was set to 0.11 times that of

LiMn₂O₄ and NiO. The annealing on Cr₂N/SS or Cr₂N/Si current collectors was performed at 600 °C during 3 hours and in some cases at 700 °C for 1 hour, using in all experiments a 10 °C min⁻¹ heating ramp and allowing the samples to cool down naturally. The Mn to Ni ratio was measured by energy dispersive X-ray spectroscopy (EDX). The total quantity of cathode material in each cell was determined by weighing in an analytical balance (Mettler Toledo XS205 Dual Range, 0.01 mg readability) each substrate before and after deposition of LMNO, obtaining an average of approximately 0.5 mg of LMNO per coin cell measured.

SEM images were acquired in a FEG-SEM HITACHI S-4800 working at 5 kV to minimize electrical charging of the layers. EDX spectra were registered at 10 kV using a Bruker XFlash 6|10 X-ray detector with 121 eV resolution at Mn K_α and the standardless quantification was performed with the software ESPRIT from Bruker. X-ray diffractograms were obtained with a PANalytical X'Pert PRO diffractometer using the CuK_{α1} radiation in a Bragg–Brentano configuration, while the grazing incidence X-ray diffraction diagrams (GIXRD) were acquired in a PANalytical X'Pert PRO MPD diffractometer using CuK_α radiation. Four-point probe resistivity measurements were done in a NAGY SD-600 sheet resistivity meter on the soda lime glass coated substrates with an error in the measured sheet resistance below 2%. X-Ray Photoelectron Spectroscopy (XPS) measurements were performed with monochromatized Al K_α X-ray source (PHI Quantum 2000 equipment) at room temperature on both Cr₂N/SS and Cr₂N/Si samples. The surveys were acquired with 117.4 eV pass energy, and single scans with 29.35 eV pass energy. The latter provides high resolution scans with a full width half maximum of 1 eV. Depth profiles were carried out with an Ar⁺ ion sputter gun, at acceleration voltage of 2 kV. Atomic concentrations were evaluated using MultiPak software.

Electrochemical measurements were conducted in air tight coin-type cells, as in the scheme from Fig. 4.1, assembled in an Ar-filled glove box (O₂ < 0.1 ppm, H₂O < 0.1 ppm). Elemental lithium was employed as both reference and counter electrode in Li⁺ ion half-cells. As electrolyte 1 M LiPF₆ (battery grade, Novolyte) in dimethylcarbonate and ethylene carbonate (1:1 EC:DMC by weight, Novolyte) with 3 wt% 4-fluoro-1,3-dioxolan-2-one (FEC, battery grade, Solvionic) was used. Pre-dried glass microfiber (GF/D, Whatman, 80 °C for 12 hours under vacuum) served as separator. LMNO cells were cycled between 3–5 V vs. Li⁺/Li. All electrochemical measurements were carried out at room temperature on MPG2 multi-channel workstation (BioLogic). Specific capacities and currents were quantified with respect to the mass of the electrode loading.

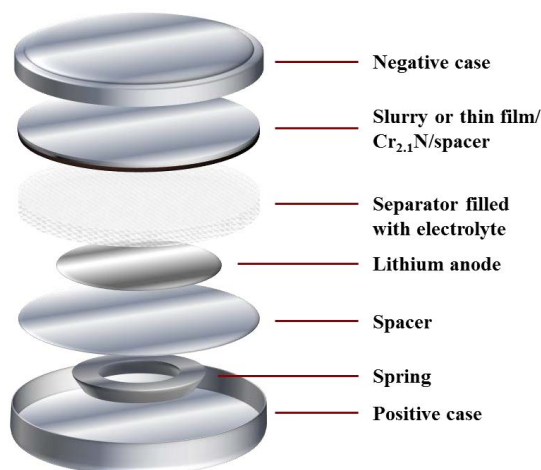


Fig. 4.1 Scheme of the coin cells assembly used in this work

To test the electrochemical stability of the current collectors the same setup was used. In this case the current collectors were not coated with any electrode material and the electrochemical measurements were performed on aluminum coated with ~ 500 nm of Cr_2N ($\text{Cr}_2\text{N}/\text{Al}$) and bare aluminum for comparison.

Electrochemical impedance spectroscopy (EIS) was performed on annealed (3 hours at 600°C in air) LMNO deposited on $\text{Cr}_2\text{N}(500\text{ nm})/\text{Si}(100)$. 100 nm thick gold top contacts were deposited by thermal evaporation at a pressure of $\sim 10^{-4}$ Pa and a rate of 1.2 \AA s^{-1} onto the annealed LMNO, and copper wires were bonded to them with silver paste (see scheme in Fig. 4.19a). The measurements were done at open circuit voltage in a VMP3 multichannel workstation (Bio-Logic) in the frequency range 1 MHz to 10 mHz and applying a bias of 100 mV.

4.3 Results and Discussion

The evolution of the Cr_xN film composition and resistivity, with respect to the nitrogen–argon ratios during deposition are presented in Fig. 4.2. The Cr content was derived from EDX and decreases with higher N_2 ratios, while the resistivity increases substantially. The film thickness also decreases with higher N_2 ratios. Above a N_2/Ar ratio of 1.49 only CrN is obtained and the deposition rate continues to decrease. The thickness variation with the N_2/Ar ratio is shown in Fig. 4.3.

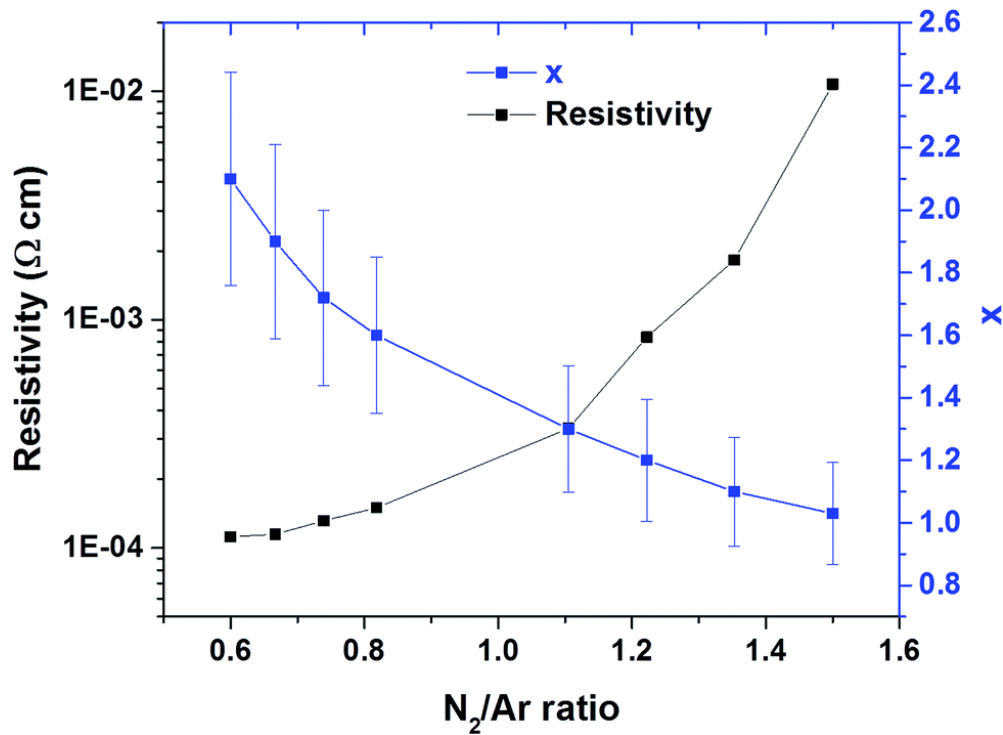


Fig. 4.3 Approximate composition (x) and resistivity of Cr_xN films on soda lime glass as function of Ar/N_2 ratio in the sputtering gas.

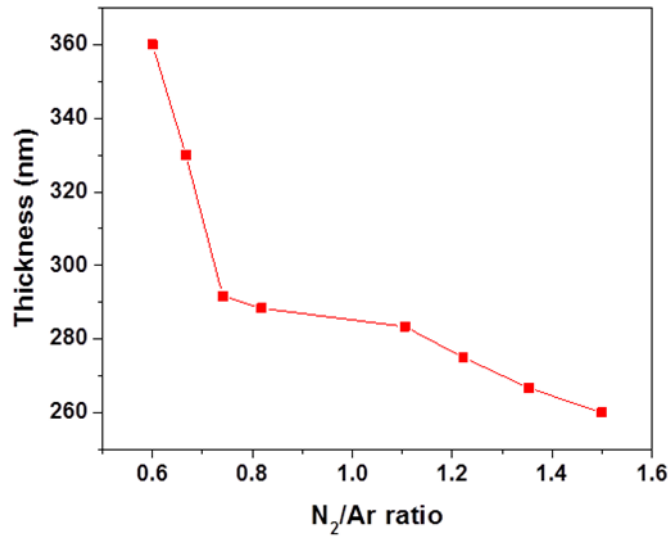


Fig. 4.2 Cr_xN thin film thickness determined by SEM (Fig. 4.4) as a function of the N_2/Ar ratio.

The XRD diagrams in Fig. 4.4 represent the phase evolution of the Cr_xN films deposited on soda lime glass when x varies from 1 to 2.1, observing a clear phase transition from cubic CrN (JCPDS 11-0065) to hexagonal β - Cr_2N (JCPDS 35-0803).^{143,144} For comparison the XRD of a thin film of Cr prepared using only Ar is also shown in Fig. 4.4 (JCPDS 019-0323).¹⁴⁵ The observed changes in the peak intensities, position and width between $x = 1$ and $x = 1.6$ can be attributed to differences in nitrogen content in the $Cr-N$ solid solution. At $x = 1.7$ there seems to be a coexistence of the cubic and hexagonal phases, while at $x = 1.9$ the shoulder at the right of the $Cr_2N(111)$ peak could be a reminiscence of the cubic phase. For $x = 2.1$ only the peaks

assigned to Cr_2N hexagonal phase can be observed. The as-obtained Cr_2N is a polycrystalline film with a slight preferred orientation in the (110) direction with a Lotgering factor of $F(110) = 0.17$,¹⁴⁶ and the observed peaks are shifted compared to the reference pattern which might be attributed to residual stress in the film (Fig. 4.5). We observe that the phase evolution in Fig. 4.4 corresponds well to the x value obtained *via* EDX.

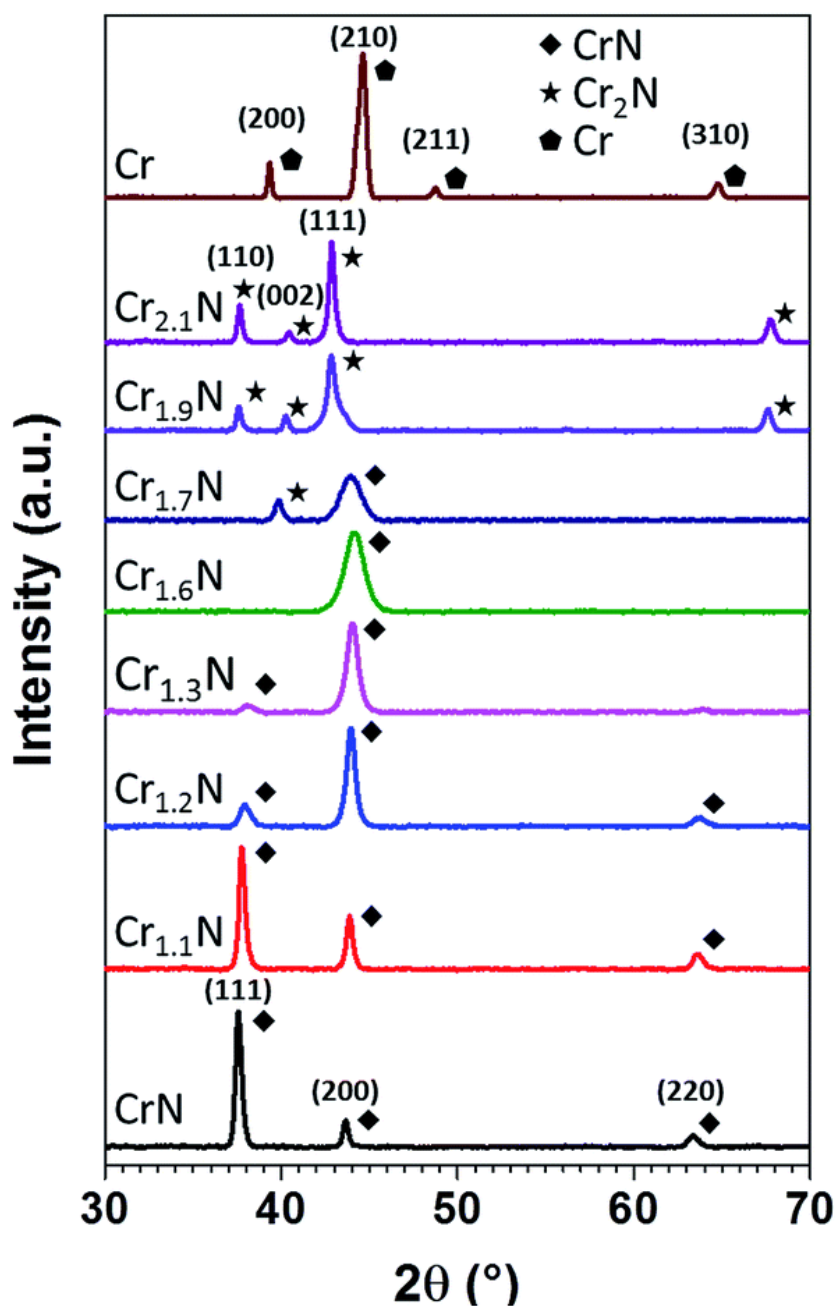


Fig. 4.4 X-ray diffractograms of Cr_xN thin films exhibiting different estimated Cr/N ratios prepared at 300 °C by pulsed DC magnetron sputtering.

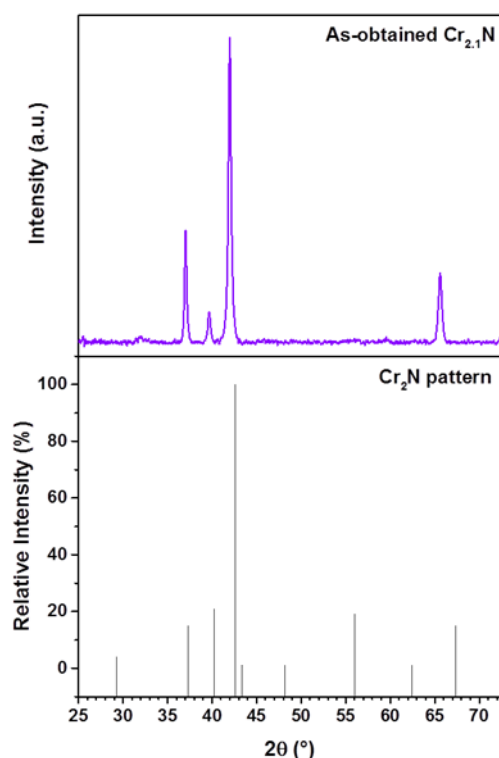


Fig. 4.5 Relative peaks intensities of as-prepared $\text{Cr}_{2.1}\text{N}$ (top) and the Cr_2N pattern.

The microstructure change of Cr_xN thin films grown by pulsed DC magnetron sputtering was studied by SEM, revealing a noticeable difference in the microstructure and surface roughness of the films with different Cr content (Fig. 4.6a–d). The film cross-sections present a columnar microstructure for the CrN and $\text{Cr}_{2.1}\text{N}$ cases as seen in Fig. 4.6d. In the intermediate composition between $\text{Cr}_{1.2}\text{N}$ and $\text{Cr}_{1.7}\text{N}$ the columnar features become less defined as the composition reaches a value close to $\text{Cr}_{1.6}\text{N}$ giving rise to more compact films (Fig. 4.6d, 4.7 and 4.8). At $x = 1.7$ the columnar features begin to reappear (Fig. 4.7) which may be caused by the phase transition to Cr_2N . This correlates well with the XRD diagrams from Fig. 4.4 where it can be observed that, for $x = 1.6$, only a broadened $\text{CrN}(200)$ peak is present. The higher deposition rates resulting from a lower N_2 content in the gas mixture are offset by the growing density of the film as it changes to Cr_2N . This results in a higher growth rate at higher x values. SEM images for other intermediate compositions can be found in Fig. 4.7 and 4.8.

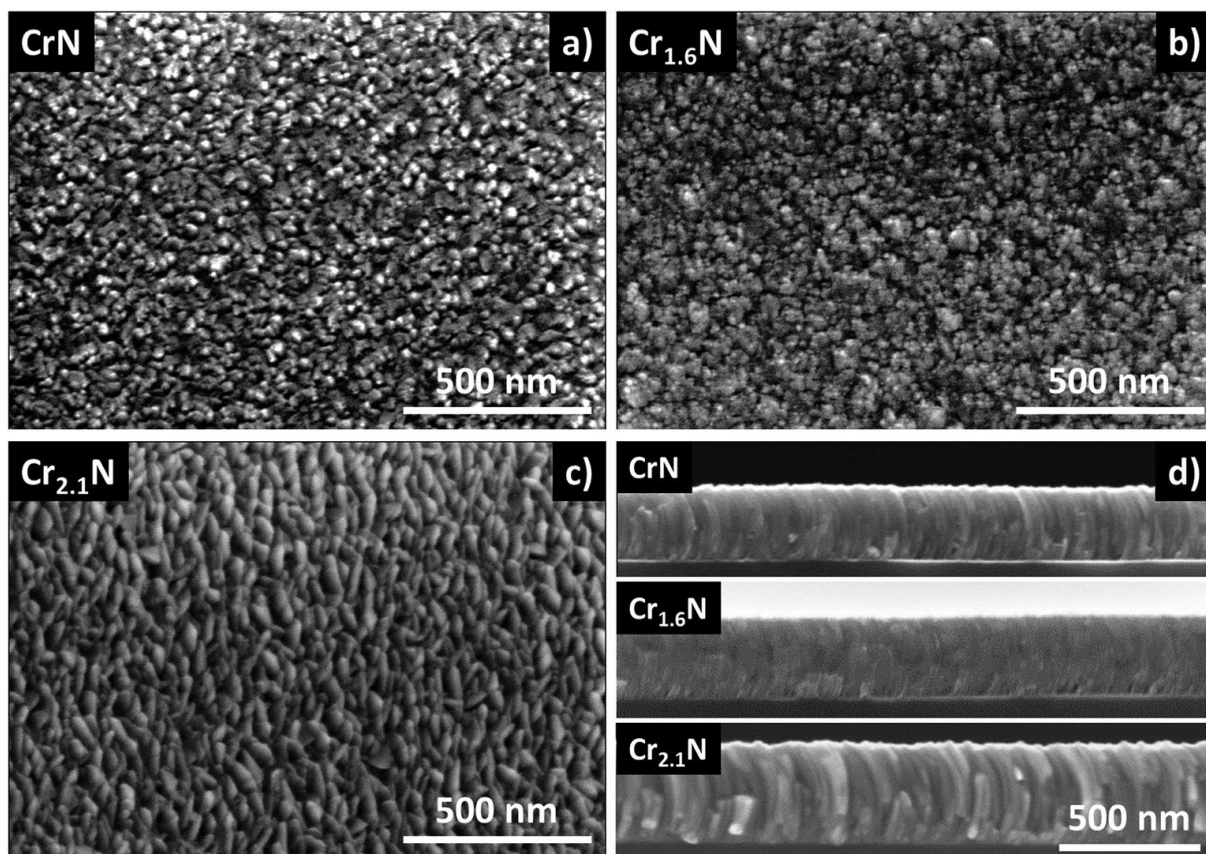


Fig. 4.7 SEM images of Cr_xN thin films with 3 different N_2 contents prepared at 300 °C by pulsed DC magnetron sputtering, showing the surface roughness of the as-prepared samples, normal views (a–c), and their columnar morphology, cross sections in (d).

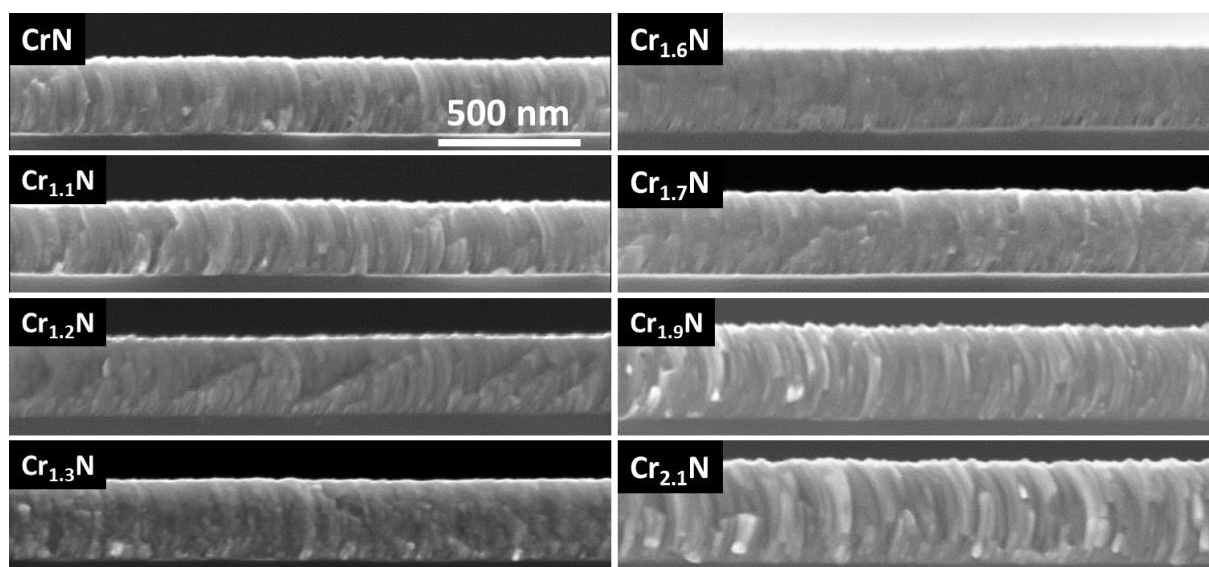


Fig. 4.6 SEM cross sections of Cr_xN thin films on Si(100).

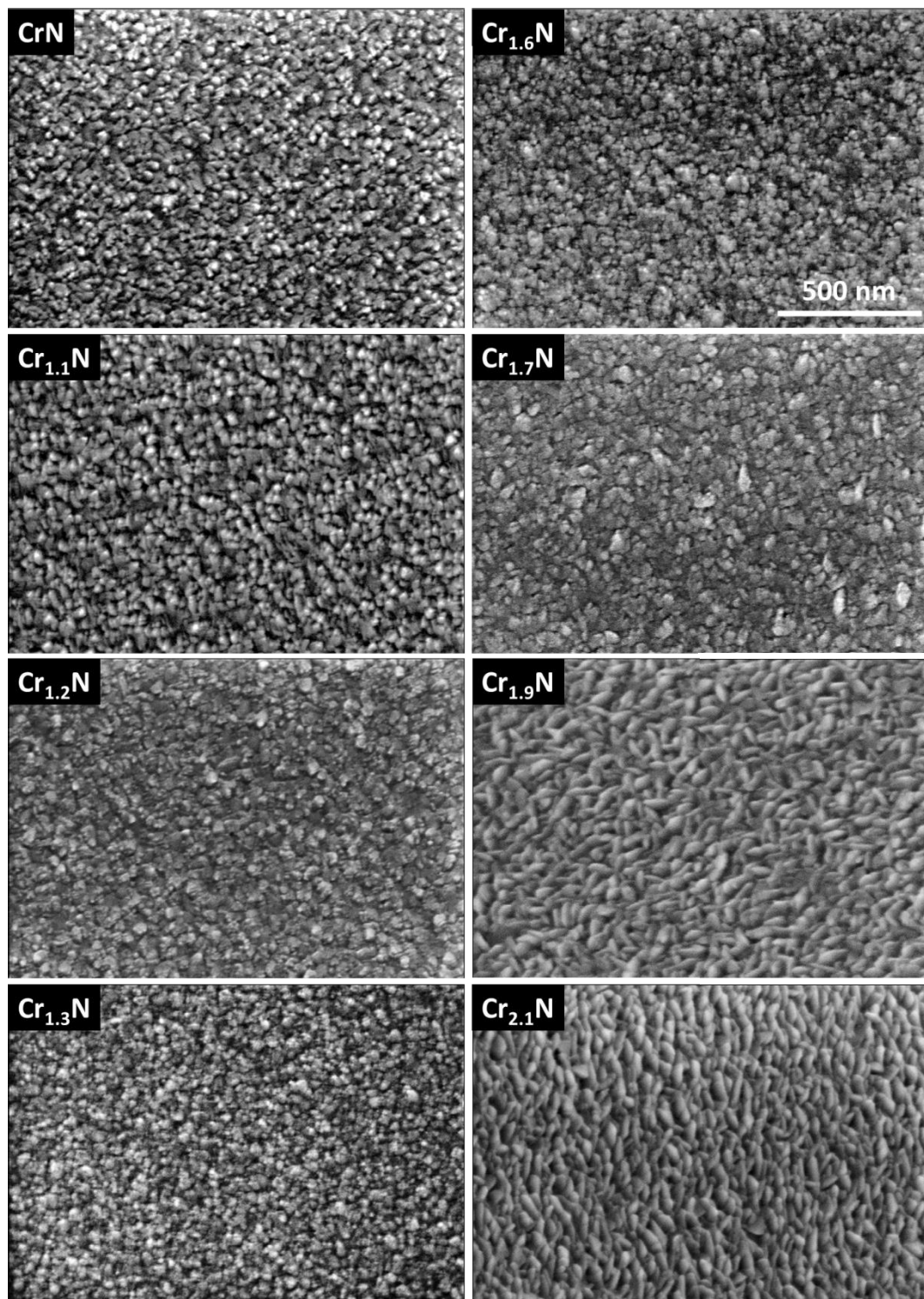


Fig. 4.8 SEM normal views of Cr_xN thin films showing the change in surface microstructure for CrN - $\text{Cr}_{2.1}\text{N}$ (the scale is the same for all images).

The sheet resistance of $\text{Cr}_{2.1}\text{N}$ thin films of 489 nm was determined to be as low as $2.6 \, \Omega \, \text{sq}^{-1}$, which is close to the estimated bulk value (data points and fitting shown in Fig. 4.9a). Furthermore, as the thickness of these layers increased, they evolve towards a more columnar and porous microstructure, presenting fully developed curved columns at $\sim 300 \, \text{nm}$, as a result of our deposition configuration (moving substrate), as observed in the SEM images in Fig. 4.10 (SEM normal views in Fig. 4.11).

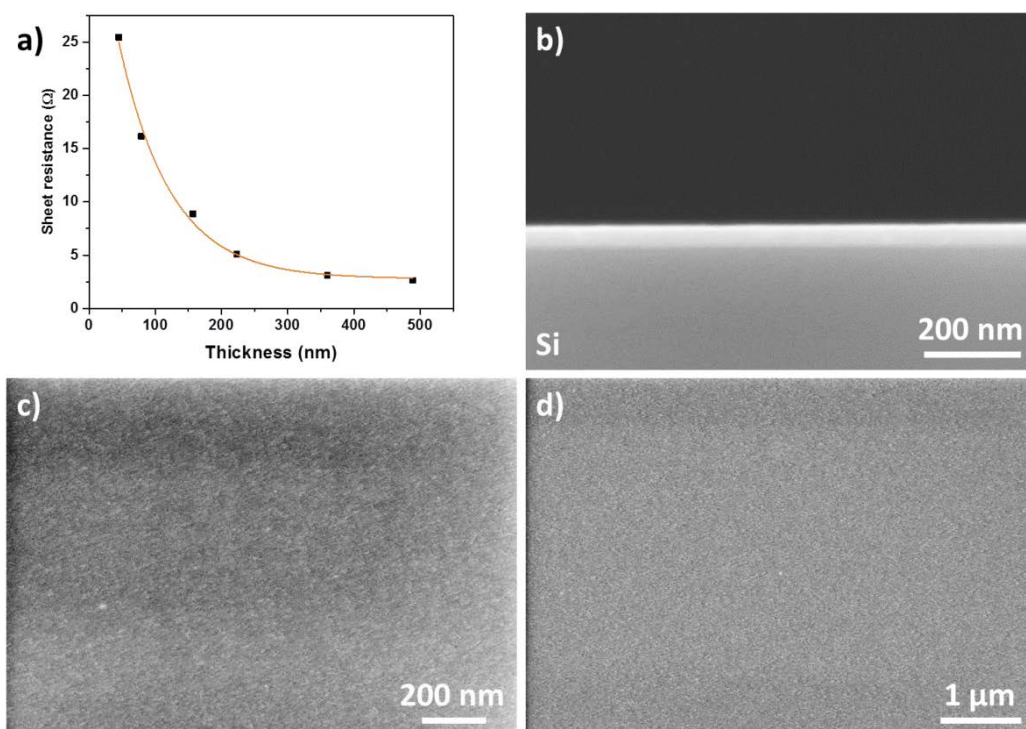


Fig. 4.9 a) Evolution of $\text{Cr}_{2.1}\text{N}$ sheet resistance with thickness. b)-d) SEM micrographs of a 45 nm thick $\text{Cr}_{2.1}\text{N}$ film.

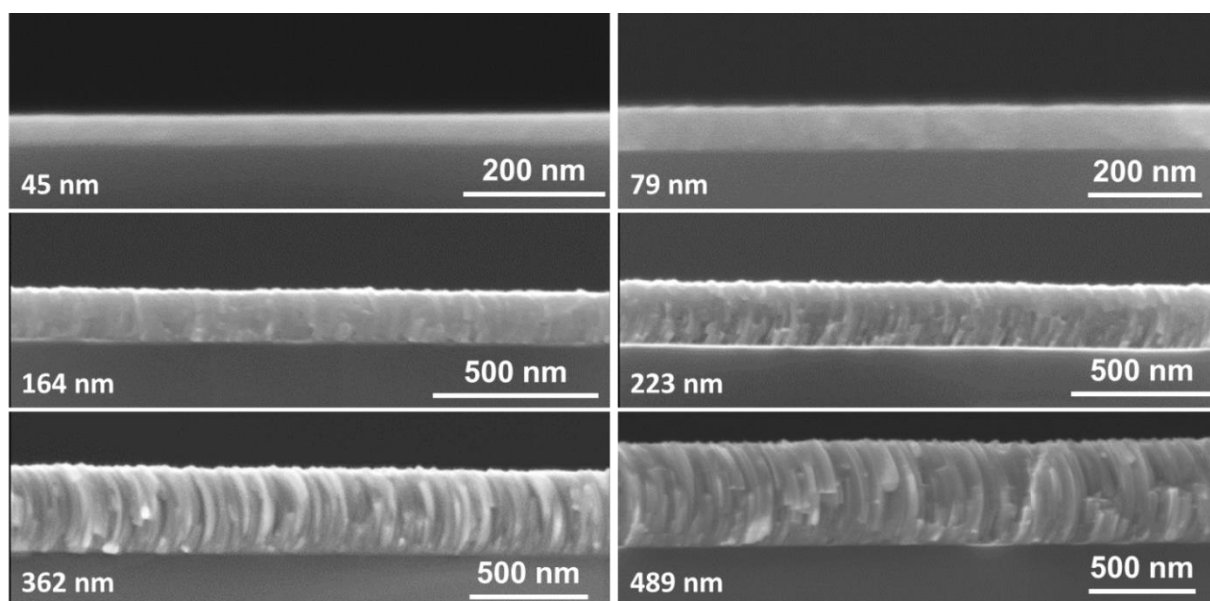


Fig. 4.10 SEM cross sections of $\text{Cr}_{2.1}\text{N}$ with different thicknesses

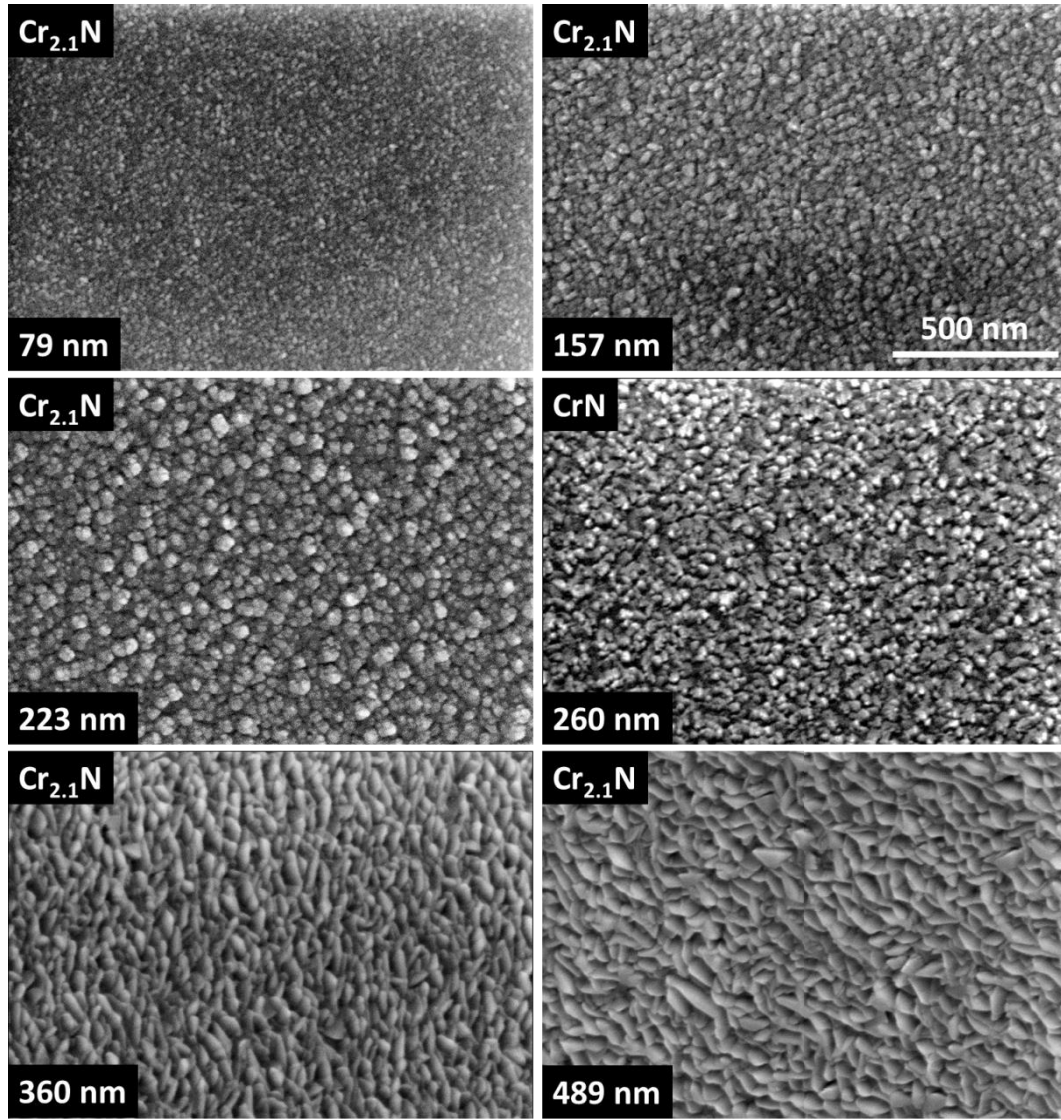


Fig. 4.11 SEM normal views of Cr_{2.1}N with different thicknesses showing the change in surface microstructure. A 260 nm thick CrN film has been included for comparison.

For the Cr_{2.1}N composition, the thickness of the film was kept between 45 nm and 489 nm, Fig. 4.10. The sheet resistance measured as shown in Fig. 4.10a), revealed an exponential trend for the sheet resistance that approximately obeys the equation $sh = 2.79 + 39.56 \times e^{-0.01 \times th}$ [$R^2 = 0.992$], where sh is the sheet resistance and th the thickness. Even for the thinnest film prepared, at 45 nm, the sheet resistance remains relatively low and from the SEM micrographs of Fig. 4.9(b-d) no macroscopic voids are observed, although this low thickness region is characterized by the presence of discontinuities or islands in the film. For the sake of simplicity and to emphasize that the chromium rich composition obtained corresponds mainly to the Cr₂N phase, Cr_{2.1}N will henceforth be referred to as Cr₂N.

Electrochemical characterization of Cr₂N films was performed on Al foil substrates (Cr₂N/Al) aiming to simplify cell assembly using coin cell configuration. Aluminum foil is a commonly used cathode current collector in lithium ion batteries which is highly resistant to oxidation and has good electronic conductivity. The morphology and resistivity of Cr₂N/Al films was identical to those formed on silicon and glass. Electrochemical stability measurements of Cr₂N/Al films were done by cyclic voltammetry (CV) at a slow scan rate of 0.1 mV s⁻¹ to reveal any signs of oxidation of Cr₂N. The measurements in Fig. 4.12a and b show that during the first cycle both Al and Cr₂N/Al current collectors have very low current density (about 10–20 $\mu\text{A cm}^{-2}$) in the whole 2–5 V voltage range even at very high potentials proving high resistance to oxidation in Cr₂N/Al films. Small signs of oxidation observed in Fig. 4.12a and b above 4.5 V vs. Li⁺/Li for both Cr₂N/Al and Al current collectors can be assigned to the decomposition of the LiPF₆ electrolyte itself,¹⁴⁷ whereas the anodic peaks at 3.7 V and 4.2 V during the first cycle are usually attributed to the passivation of Al (note that Cr₂N/Al has only one side coated with Cr₂N).²¹ Moreover, after only 3 cycles Cr₂N/Al current collector shows almost complete passivation evidenced by a negligible current density in the CV, closely resembling the behavior of Al.²¹

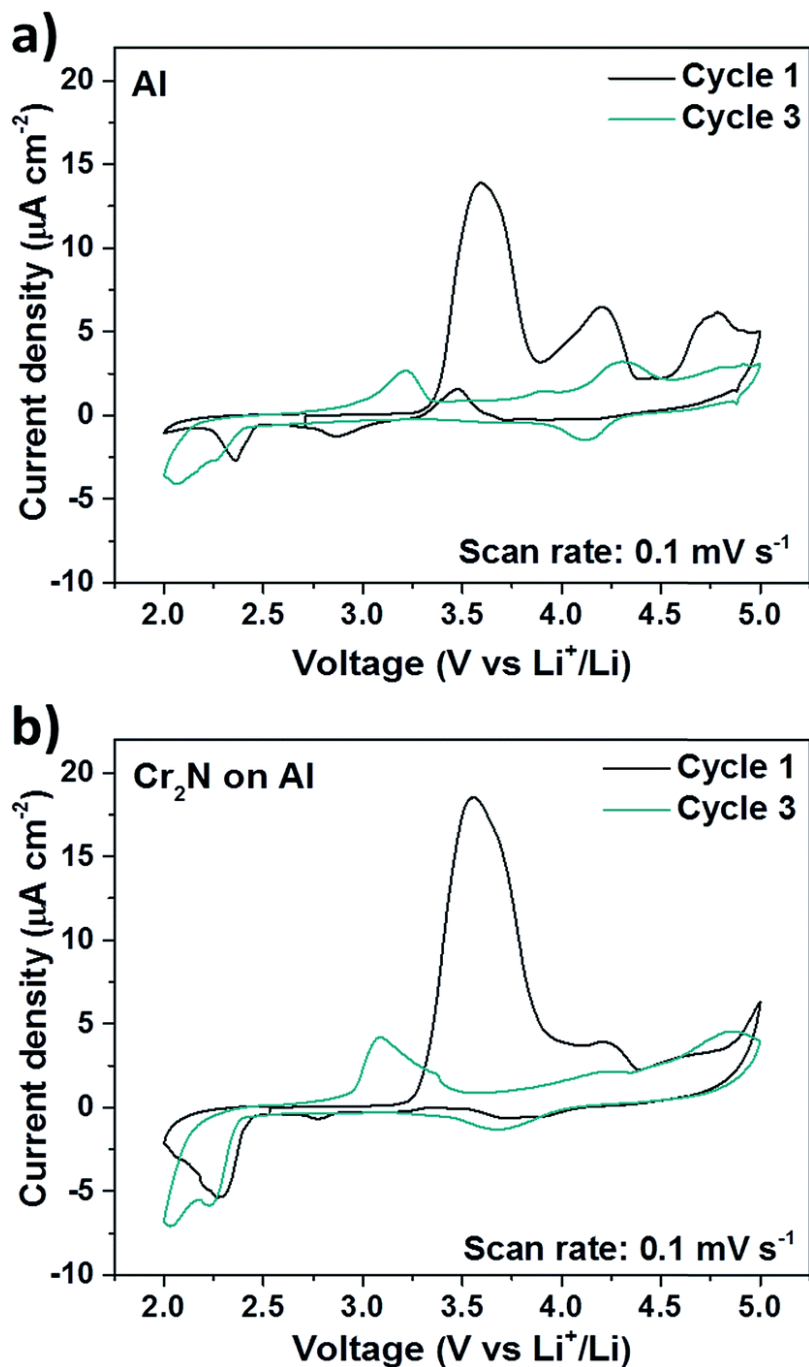


Fig. 4.12 Electrochemical performance of $\text{Cr}_2\text{N}/\text{Al}$ ~500 nm thick CC in comparison with aluminum foil. (a) CVs of bare Al foil between 2–5 V vs. Li^+/Li . (b) CVs of $\text{Cr}_2\text{N}/\text{Al}$ CC between 2–5 V vs. Li^+/Li .

In order to address the high temperature oxidation and lithium resistance of the Cr_2N current collector, GIXRD and XPS studies were performed on LMNO/ Cr_2N . The high potential cathode material LMNO was deposited by RF-magnetron sputtering at a substrate temperature of 220°C . At this temperature and low pressure (0.05 Pa) it is expected that the LMNO thin film presents a growth according to zone T in Thornton's structure zone model, i.e. not well defined fibrous grains, which is in agreement with SEM observations in Fig. 4.14, top.¹⁴⁸ Moreover, there is a diffuse interface between LMNO and Cr_2N of roughly 50 nm (Fig. 4.13a). The observed nanograins on the surface (Fig. 4.13b) correlate well to the wide full-width-half-

maximum observed in the XRD of the as-prepared LMNO (Fig. 4.13c). After annealing at 600 °C for 3 hours significant changes occur to the LMNO/Cr₂N multilayer as evidenced in the SEM cross section in Fig. 4.15b and described below. Compared to the as-prepared sample (Fig. 4.13a, b and 4.14, top), the LMNO/Cr₂N interface of the annealed sample is considerably thicker and has a higher porosity, while the Cr₂N columns are now fused.

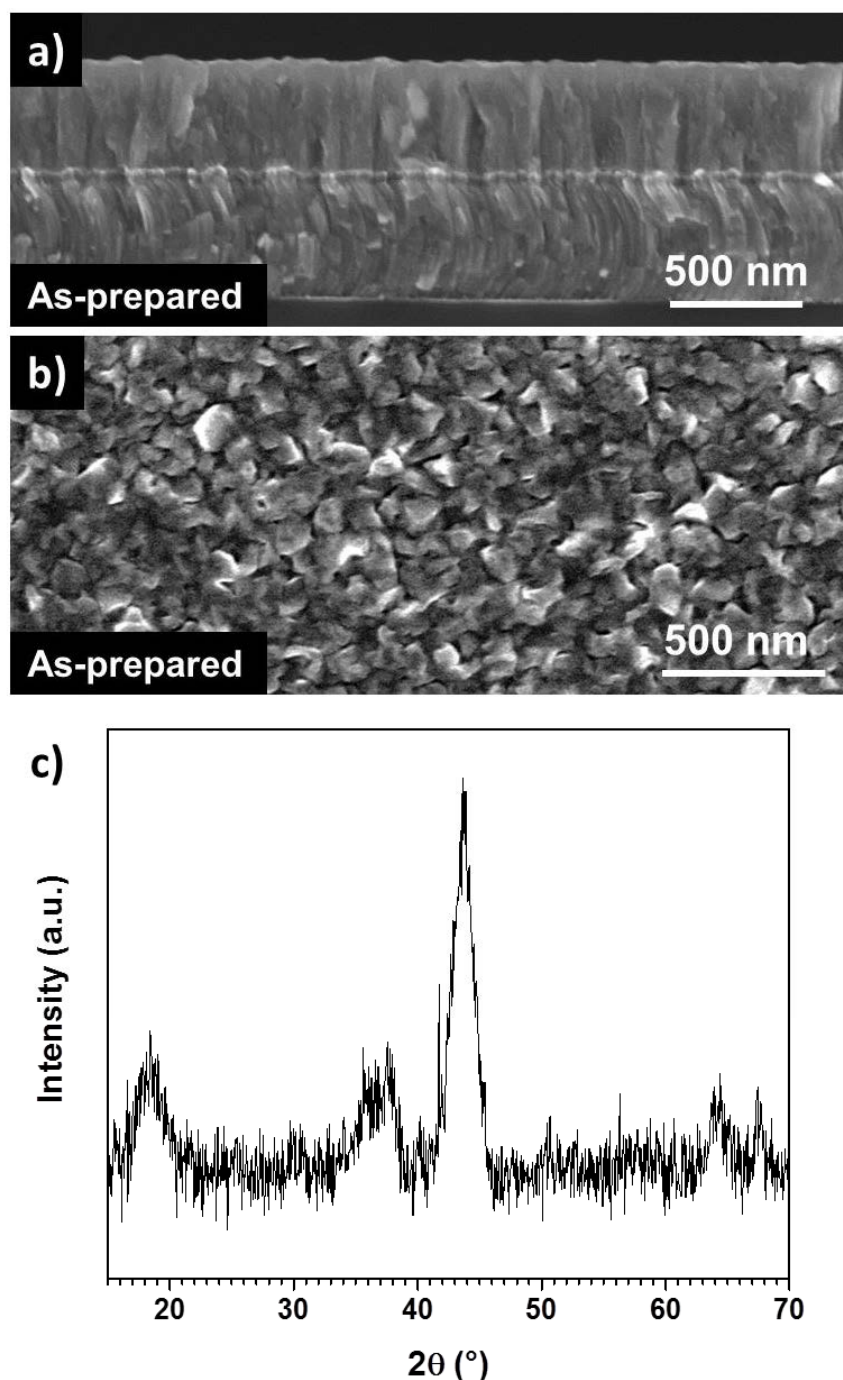


Fig. 4.13 SEM normal view of as-prepared LMNO(500) on Cr₂N(500 nm)/Si (a) and its cross section (b). c) GIXRD of as-prepared LMNO(500 nm)/Cr₂N(500 nm)/SS at $\omega = 1^\circ$.

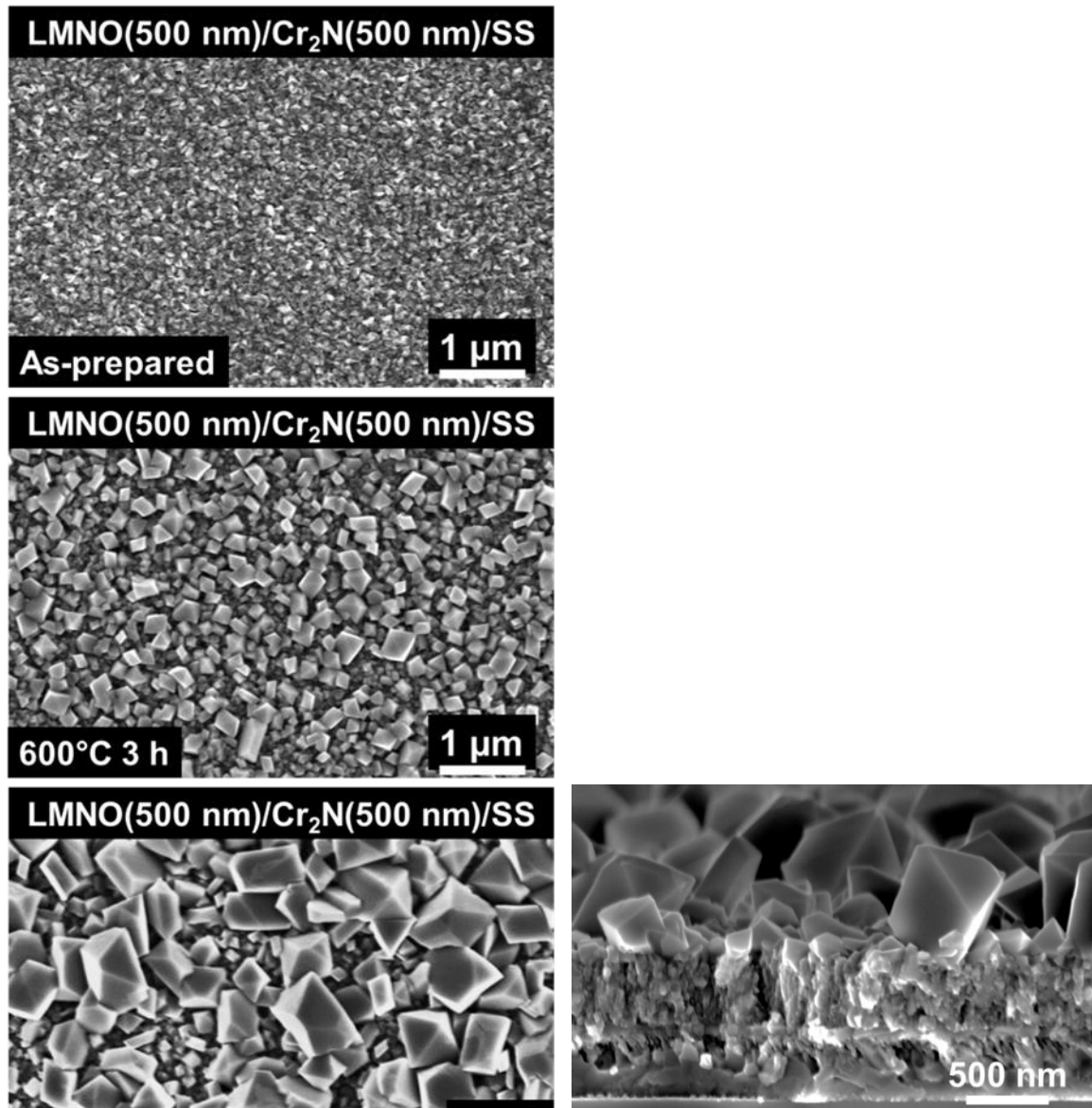


Fig. 4.14 SEM normal views of LMNO(500 nm)/Cr₂N(500 nm)/SS for the as-prepared (top), 600 °C 3 h (middle) and 700 °C 1h (bottom left) cases. Upon annealing, the surface of the samples develop crystals. The size depends on the annealing temperature, observing the largest crystal for the 700 °C 1 hour treatment, which may be attributed to the large surface segregation of chromium (bottom right).

In addition to microstructural changes in the thin films, a polycrystalline second layer of LMNO can be seen after annealing. On the original LMNO film surface a large number of crystals form which increase in size up to ~500 nm as the temperature is increased to 700 °C (Fig. 4.14, bottom left and right). The preferential diffusion of different cations towards the surface of LMNO has already been reported by Shin D. W. et al. and was attributed to the a possible structural stabilization driven by the surface free energy (σ).¹⁴⁹ σ can be lowered by the presence of particles of different chemical nature to the surface, leading to the growth of surface crystals by heterogeneous nucleation.¹⁵⁰ This phenomenon could explain the formation of crystals at 600 °C (Fig. 4.15 and Fig. 4.14 middle) which is caused by the diffusion of chromium towards the surface and subsequent nucleation (see Fig. 4.15c). At 700 °C (Fig. 4.14, bottom left and right) large crystals grew on the LMNO surface at the expense of Cr (from

Cr₂N) and LMNO, that now show a higher porosity. The diffractogram in Fig. 5.15a for LMNO(500 nm)/Cr₂N (500 nm)/SS annealed at 600 °C for 3 hours indicates that LMNO is crystalline. For a grazing angle of 1° all the main peaks related to the Fd $\bar{3}$ m cubic spinel structure are clearly present (JCPDS 80-2162) and in perfect agreement with previously reported studies on LMNO layers deposited by sputtering. However, we are unable to distinguish whether the observed diffraction peaks originate from the surface crystals, the LMNO film, or a combination of both due to the proximity of Cr-doped LMNO lattice parameters^{151,152} On the other hand, when the angle is increased to 5° the peaks coming from the Cr₂N current collector and stainless steel substrate are observed unchanged by the annealing treatment. A thicker Cr₂N layer (1200 nm) has been chosen for the XRD analysis for a more pronounced view of the evolution of the Cr₂N peaks, but the cells for electrochemical measurements were fabricated using a thinner Cr₂N layer (500 nm).

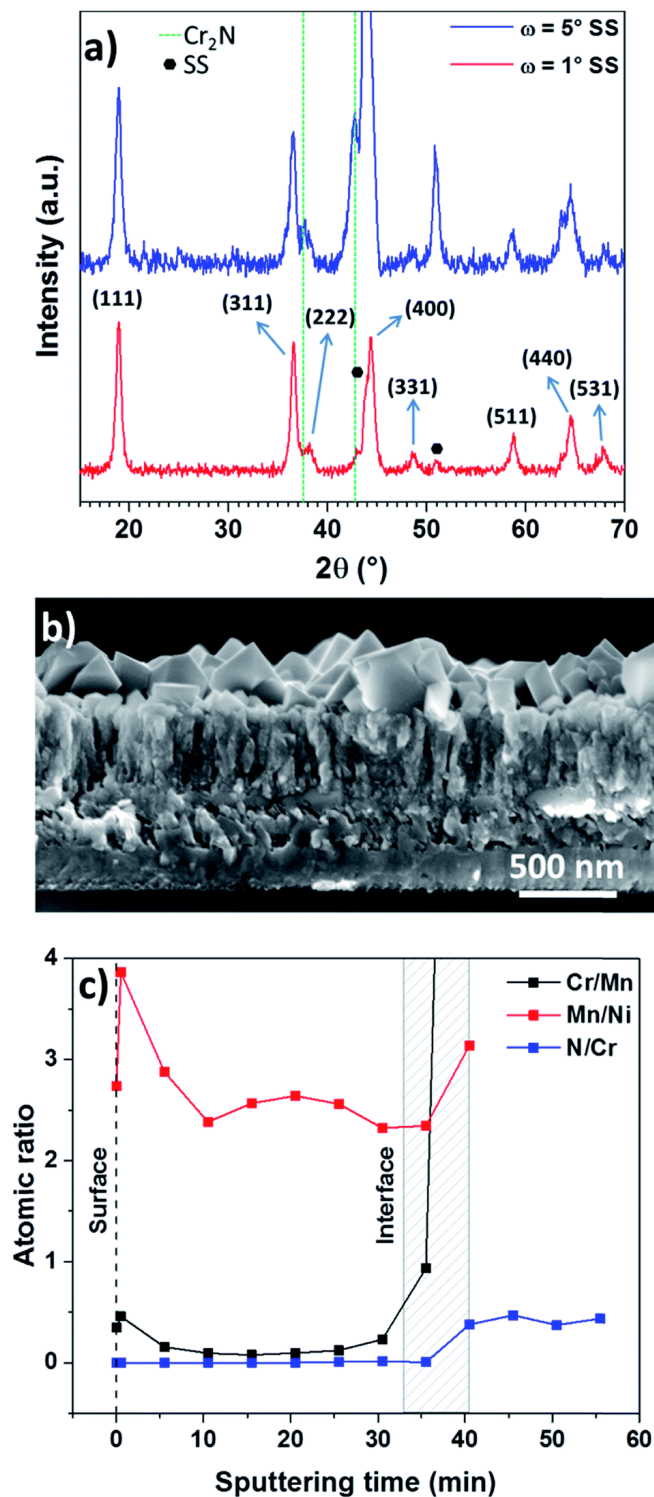


Fig. 4.15 (a) GIXRD of annealed LMNO(500 nm)/Cr₂N(500 nm)/SS at grazing angles (ω) 1° and 5°; the green dashed lines indicate the Cr₂N peaks. (b) SEM cross section of LMNO(500 nm)/Cr₂N(500 nm)/SS. (c) Atomic ratios calculated from XPS sputter-depth profiles for LMNO(500 nm)/Cr₂N(500 nm)/SS, the dashed line represents the LMNO surface and the dashed rectangle depicts the interface region between LMNO cathode material and Cr₂N current collector. The thermal treatment was in all cases 600 °C for 3 hours.

For temperatures of 600 °C and above the surface area is increased due to the aforementioned formation of crystals which might lead to an enhancement of the performance at high cycling rates. The XPS sputter-depth profiles in Fig. 4.16 for LMNO(500 nm)/Cr₂N(500 nm)/SS annealed at 600 °C for 3 hours revealed Cr incorporation into LMNO and some oxidation of Cr₂N evidenced by the shoulder at higher binding energies in the Cr peaks around the 40.5 minute mark and a still prominent oxygen signal. Note that the nitrogen signal appears at this mark, indicating a coexistence of chromium oxide and chromium nitride at the interface, while at the 35.5 minute mark there is no nitrogen detected while the oxygen peak at lower binding energies can be assigned to a chromium oxide species (not incorporated into the LMNO). The atomic ratio calculated obtained from the XPS sputter-depth profile in Fig. 4.16 is displayed in Fig. 4.15c, where it can be seen that the concentration of Cr is higher at the LMNO surface (sputter time 0, dashed line) in line with our hypothesis regarding the formation of crystals at the LMNO surface and the previously reported surface segregation observed for Cr-doped LMNO.¹⁴⁹ The Mn/Ni ratio lies around 2.6 at the bulk of the LMNO while the N/Cr ratio (at the 50.5 minute mark) gives an approximate composition of the alloy of C_{2.4}N, in good agreement with EDX data (Table ST1†) and in line with the GIXRD diagram from Fig. 4.15a. The dashed rectangle in Fig. 4.15c has been included to give an idea of the LMNO–Cr₂N interface region. In the case of the 1 hour thermal treatment at 700 °C the concentration of Cr in the LMNO film is even higher than that of Ni, indicating a heavier oxidation of the Cr₂N current collector as evidenced in Fig. 4.17 by broadened Cr peaks throughout the entire analyzed depth and a more intense oxygen peak even after 95 minutes of sputtering, and a much higher Cr/Mn ratio, as shown in Fig. 4.18. In addition, this higher concentration of Cr is correlated with the presence of larger crystals when compared to the 600 °C thermal treatment for 3 hours. However, Cr doping has been demonstrated to be an effective way to stabilize the LMNO cathode, so it can be expected that the incorporation of a certain amount of this element into LMNO has no negative effect on its performance.¹⁴⁹ XPS surveys can be found in Fig. S7.3.

LMNO(500 nm)/Cr₂N(500 nm)/SS 600 °C 3 h

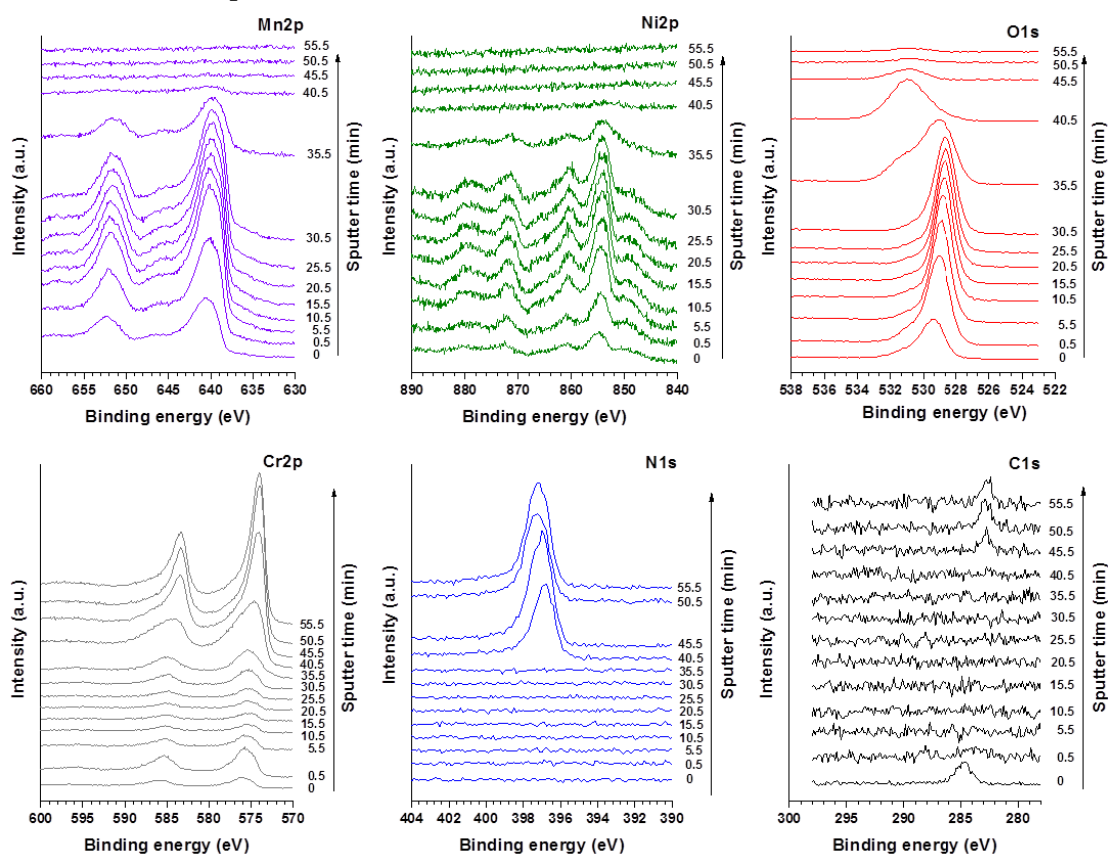


Fig. 4.16 XPS peaks for several elements in the sputter-depth profile of LMNO(500 nm)/Cr₂N(500 nm)/SS, annealed at 600 °C for 3 hours.

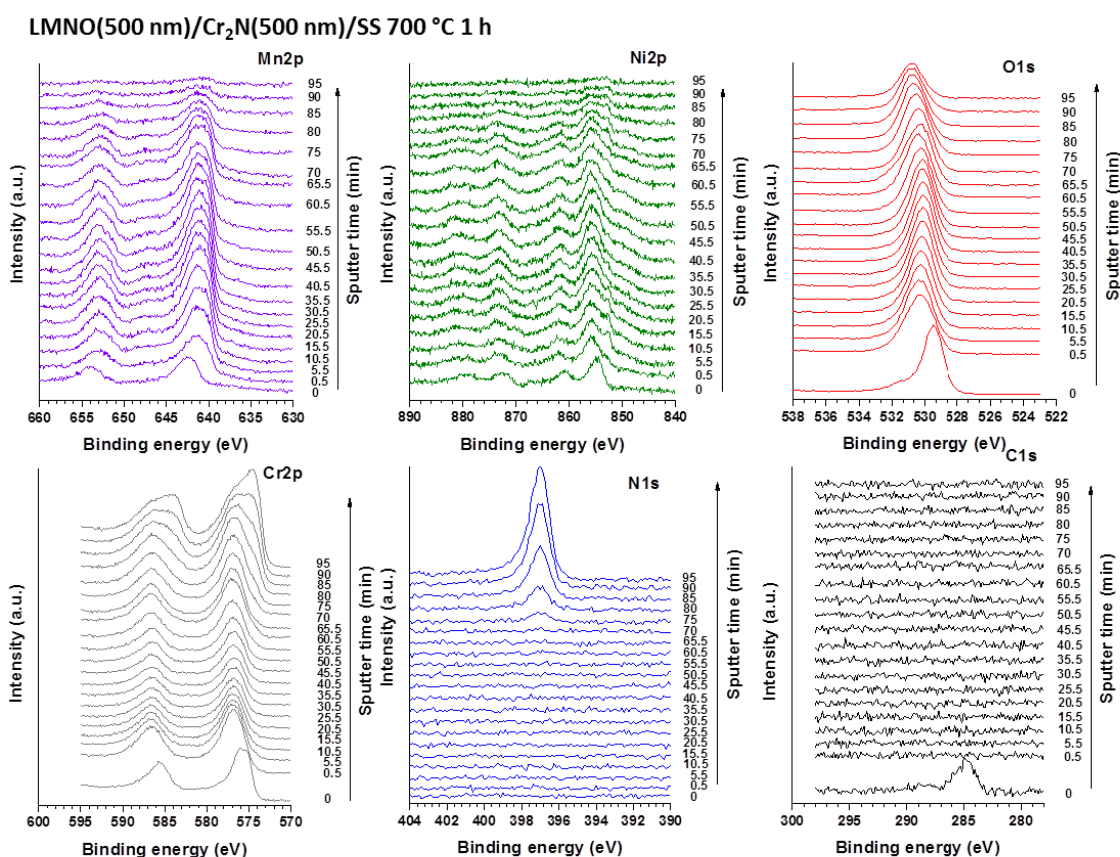


Fig. 4.17 XPS peaks for several elements in the sputter-depth profile of LMNO(500 nm)/Cr₂N(500 nm)/SS, annealed at 700 °C for 1 hour.

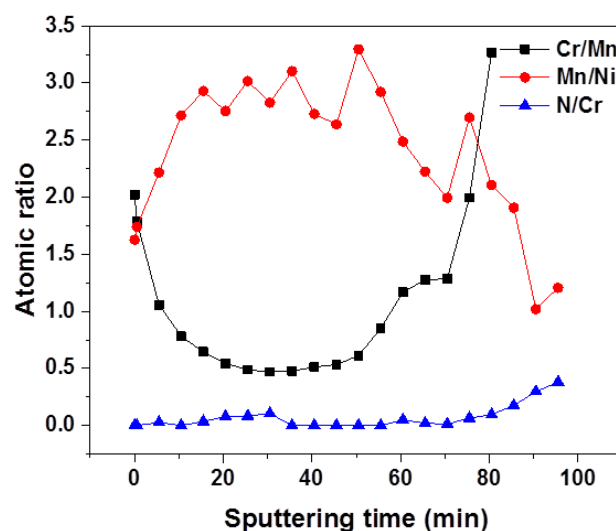


Fig. 4.18 Mn/Cr, Mn/Ni and N/Cr atomic ratios for LMNO(500 nm)/Cr₂N(500 nm)/SS after annealing at 700 °C 1 hour.

In order to assess the electrochemical characteristics of the LMNO/Cr₂N multilayer, through-plane EIS was carried out. After annealing the multilayer for 3 hours in air at 600 °C, 100 nm thick gold top contacts were deposited *via* evaporation onto the LMNO and copper wires were bonded to them with silver paste as shown in the schematic in Fig. 4.19a. The

Nyquist plot shown in Fig. 4.19b exhibits two arcs which were modeled with the equivalent circuit shown in the inset. The first arc measured at ~ 64 kHz had a resistance of $130 \Omega \text{ cm}^2$. Due to the high frequency here, it is likely that this response is caused by electronic transport. Therefore, we assign this value to the charge transfer resistance at the interface between the current collector and cathode. Although this resistance value is higher than for pristine Cr_2N , it is comparable to optimized interfaces in solid-state battery systems which require high temperature processing.⁵⁴ The second arc, with a resistance of $658 \Omega \text{ cm}^2$ and occurring at 919 Hz could correspond to movement of lithium ions in the LMNO. When factoring in the LMNO thickness of 500 nm a Li^+ ion conductivity of $7.6 \times 10^{-8} \text{ S cm}^{-1}$ is calculated. This corresponds well to other values found in literature.¹⁵³

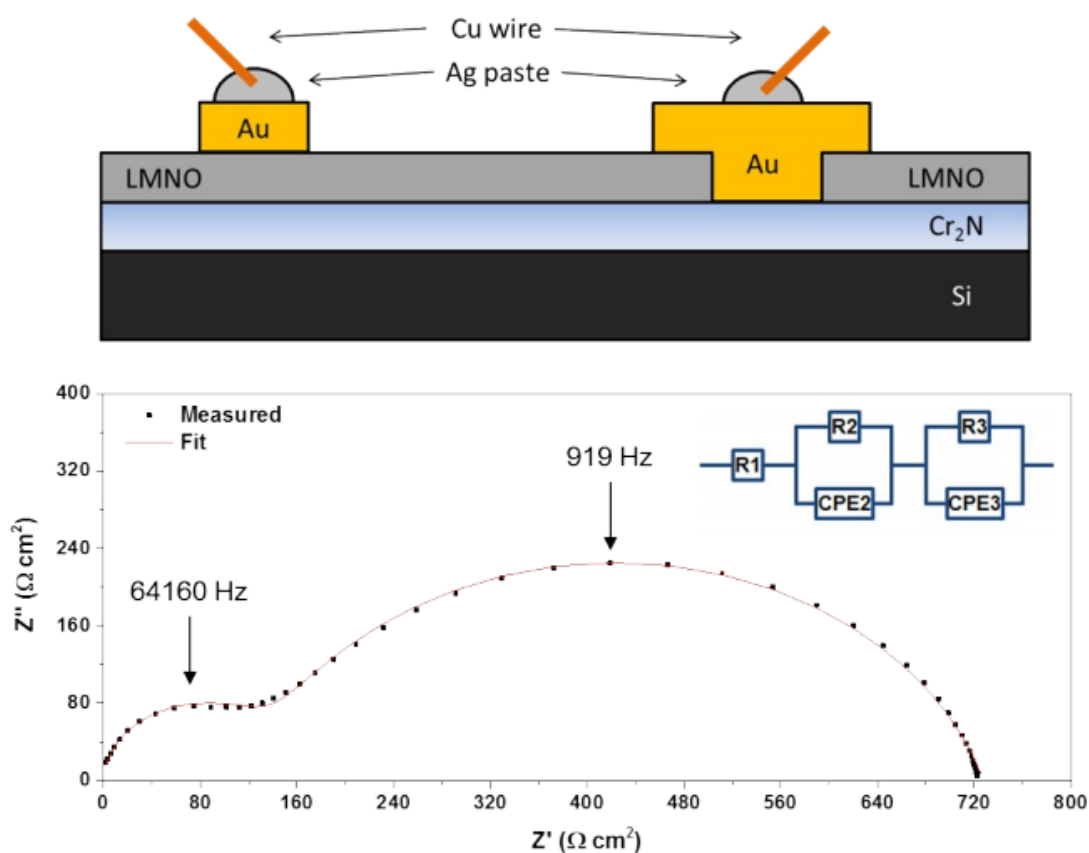


Fig. 4.19a) Schematic of the multilayer and contacts used for EIS. b) Nyquist plot at room temperature of LMNO(500 nm)/ Cr_2N (500 nm)/Si after annealing at 600°C 3 hours. Frequency range from 1 MHz to 10 mHz. The fit of the data is shown in red. The inset depicts the equivalent circuit used to fit the data, consisting of resistors and constant phase elements.

The CV curves of pure LMNO thin films (no binder or carbon black added) after annealing at 600°C for 3 hours in Fig. 4.20a clearly present the double peaks associated to the oxidation/reduction of nickel in the voltage range 4.6–5 V vs. Li^+/Li , while poor electrochemical activity was detected in the region 3.9–4.3 V consistent with the oxidation/reduction of manganese.¹⁵⁴ The clear observation of the Ni redox peaks is another indication of a good electrical contact between the current collector and the cathode as shown by Caballero et al.¹⁵⁴ Galvanostatic voltage profiles show very clear discharge–charge plateaus

with reduced hysteresis after cycle 10 (Fig. 4.20b). The cycling behavior of LMNO annealed at 600 °C (Fig. 4.20c) depends strongly on the cycling rate, exhibiting the highest initial capacity but also fastest capacity fade for the lowest rate of 1C. At 5C the initial capacity is noticeably lower as expected due to the low ionic and electronic conductivity of LMNO,¹⁵³ and the fast charge rate (equal to the discharge rate). The faster degradation at lower rates suggests that the longer time spent at higher voltages is a contributing factor. This degradation can be assigned to the partial oxidation of liquid electrolyte and to the reaction/dissolution of Ni or Mn ions into the liquid electrolyte since we previously established the stability of Cr₂N in this potential range (Fig. 4.12b),¹⁵⁵⁻¹⁵⁷ and to the presence of truncated particles on the LMNO surface (Fig. 4.14, middle and bottom left), besides octahedral ones, which have been reported to cause a poor performance/cyclability of LMNO.¹⁷ In addition, the cycling for the film annealed at 700 °C for 1 hour performed better (Fig. 4.20c), showing the slowest capacity fade and the highest coulombic efficiency probably because of an enhanced stability of the spinel structure upon cycling due to a higher incorporation of Cr³⁺ into LMNO (Fig. 4.17 and 4.18) and bigger particle size at the surface, which in turn reduce the surface area (Fig. 4.14 bottom left).¹⁵⁸ Note that the formation of LMNO thin films is not fully optimized. In order to considerably increase the performance of these cells it is mandatory to substitute the liquid electrolyte, which is unstable at high voltages, with a solid-state-electrolyte as demonstrated by J. Li et al.¹⁵⁹

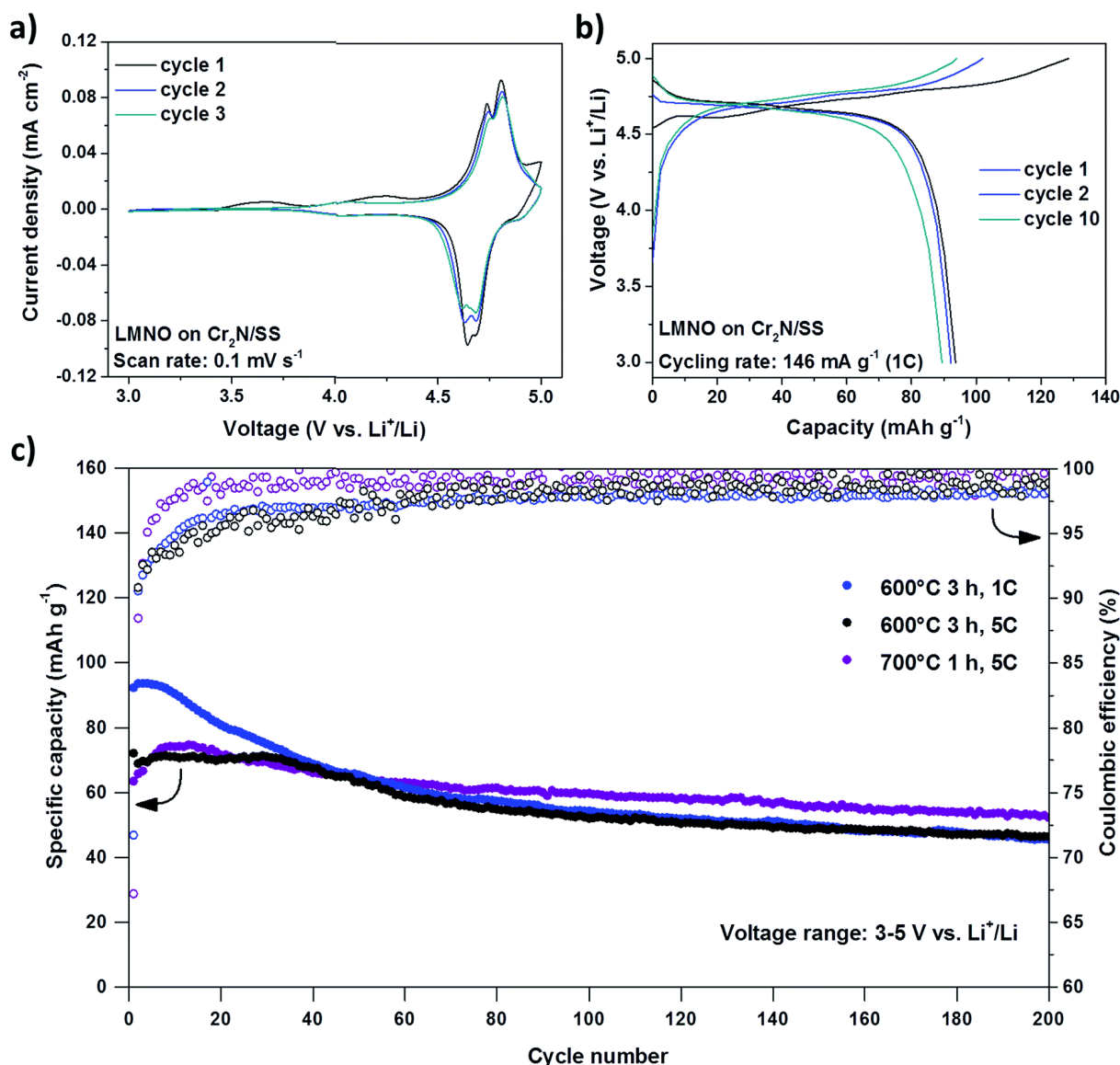


Fig. 4.20 Electrochemical performance of LMNO on Cr₂N current collectors. (a) CV of LMNO annealed at 600 °C for 3 hours and then measured between 3–5 V vs. Li⁺/Li. (b) Galvanostatic charge and discharge curves of LMNO annealed at 600 °C for 3 hours. (c) Cycling behavior of LMNO annealed at 600 °C for 3 hours and 700 °C for 1 hour measured at different C rates.

4.4 Conclusion

In order to address the current challenge of finding a current collector which can remain stable during and after thin film solid-state battery deposition processes the Cr₂N system was explored. A range of Cr_xN thin films were deposited by pulsed DC sputtering by varying the Ar/N₂ during deposition. The Cr content increased with the reduction of N₂ content, while the resistivity decreased, reaching a value of $\sim 1.1 \times 10^{-4} \Omega \text{ cm}$ for the composition of Cr_{2.1}N. With this stoichiometry the Cr₂N columnar structure formed with a preferential orientation in the (110) direction as observed by XRD. The electrochemical stability of this alloy in a LiPF₆-

based electrolyte was proven for over 200 cycles in the voltage range of 3–4.8 V vs. Li^+/Li . Moreover, the crystallization of LMNO at high temperature on the Cr_2N current collector and the subsequent cycling have demonstrated the suitability of this material as a stable current collector for lithium containing cathode materials up to 600 °C in air. The observation of Cr diffusion into the cathode varies depending on the annealing temperature. Based on these observations Cr_2N has shown to be a promising cathode current collector for use in all-solid-state thin film batteries. This is the first material which has been proven to meet all the stability requirements for such high temperature processes and therefore opens the way for high-voltage, high performance thin film electrodes to be processed directly into a full solid-state cell .

4.5 Personal Contribution

This chapter is based on work in which I was co-first author and contributed equally to the work. My specific contributions were as follows: identification of the potential of this material system for the proposed application, design of the materials characterization experiments, all XRD measurements and impedance spectroscopy, extensive discussion on all results, several full proof readings and handling of minor revisions before acceptance of the manuscript.

5 Summary and Outlook

5.1 General Conclusion

The objectives of this thesis were two fold. First, to gain a better understanding of the formation of cubic phase $\text{Li}_7\text{La}_3\text{Zr}_2\text{O}_{12}$ in thin film form, and how changing the composition and annealing conditions affects the properties of the final film. And second, to study thin films of Cr_2N as a material for use as a bottom current collector in thin film batteries. In both areas significant advancements were made which contribute towards the integration of more high performance materials into solid-state batteries which have more challenging synthesis routes but can ultimately lead to more competitive devices in the future.

The initial approach, explored in chapter 2, of annealing LLZO thin films in an atmosphere with a high LiOH partial pressure to improve lithium content in the film resulted in different ratios of tetragonal and cubic phase $\text{Li}_7\text{La}_3\text{Zr}_2\text{O}_{12}$ as well as the impurity phase $\text{La}_2\text{Zr}_2\text{O}_7$. With standard material science analysis tools such as SEM and XRD it was understood how film thickness plays a role in phase formation. Thinner films tended to form the cubic phase, and increasing the thickness resulted in the appearance of greater amounts of impurity phase $\text{La}_2\text{Zr}_2\text{O}_7$. This trend was related to a change in surface area and morphology with thinner films being partially de-wetted from the substrate thereby increasing the surface area, and making them more able to incorporate lithium from the ambient environment during annealing. Electrochemical impedance spectroscopy (EIS) over a range of temperatures revealed a very high activation energy of 1.39 eV, but at temperatures above 300°C there was a change in activation energy to 0.6 eV. From this point where the lithium ion conductivity reached $3.2 \times 10^{-1} \text{ S cm}^{-1}$ the electrolyte performed adequately in line with other results reported in literature for LLZO. The room temperature conductivity however, was too low to be measured $<10^{-9} \text{ S cm}^{-1}$. High levels of impurity phases were still observed in the continuous films that were measured which could explain the low performance. The conclusion from this work was to clearly identify the issue of Li deficiency in vacuum-deposited thin films, and the issue of dewetting for low film thicknesses. Although the technique of annealing films in a LiOH atmosphere was met with partial success, a more efficient and controllable way of maintaining a high lithium content in the electrolyte thin films was needed.

In chapter 3, thin films deposited with sputtering from Li_2O and $\text{Li}_7\text{La}_3\text{Zr}_2\text{O}_{12}$ targets simultaneously allowed the lithium content of the film to be controlled during the deposition itself. Different amounts of Ga_2O_3 were added by sputtering interspersed layers inside the film allowing cubic LLZO to form during annealing. By studying the effect of Ga and Li content on phase evolution, important insights could be gained into the interplay between the temperature of crystallization, the bonding states of each element and the final lithium ion conductivity. Several films with lithium ion conductivities above $1 \times 10^{-6} \text{ S cm}^{-1}$ at RT were formed with one film reaching $1.6 \times 10^{-5} \text{ S cm}^{-1}$. This was a large improvement over the post-annealing lithiation process in chapter 2, and marked a milestone in the research project where the electrolyte thin films had reached a good performance for integration in a full solid-state battery. In this case the total resistance of a 400 nm film would be just 2.5 Ω . Additionally, the crystallization temperature in some films for cubic LLZO was discovered to be at 500°C in the in-situ

annealing XRD patterns. This is the lowest temperature of crystallization reported so far, and could have important implications for forming all solid-state batteries with good interfacial properties and low inter-diffusion of elements during processing. These results demonstrate the importance of keeping a high lithium content in the thin films of LLZO during the annealing process.

In Chapter 4 a crucial step towards making thin film solid-state batteries possible was explored. The current collector for the lower side of the thin film battery must be stable over a wide temperature range while in contact with a lithium and oxygen containing layer. In this case Cr_xN thin films were the material of choice for the bottom current collector which were deposited *via* sputtering in different concentrations of N_2 gas. A ratio of $\text{Cr}_{2.1}\text{N}$ was found to be most beneficial for minimal resistivity. $\text{LiMn}_{1.5}\text{Ni}_{0.5}\text{O}_4$ was used as the cathode which was also deposited by sputtering and required an annealing temperature of 700°C for 1 hour. $\text{Cr}_{2.1}\text{N}$ was able to maintain its crystal structure and conductivity well after the cathode annealing. The electrochemical stability was proven up to 4.8 V and cycling of the half cell 200 times in a liquid electrolyte proved the viability of the material as a stable current collector for high temperature processing.

Overall the work presented outlines clear guidelines for forming LLZO thin films with the desired Li^+ ion conductivity required for integration into solid-state batteries. Coupled with the introduction of a stable current collector with a newly proven high temperature stability in contact with lithium and oxygen rich material, this work successfully tackles two key issues which were preventing the integration of high performance cathodes and solid electrolytes into thin-film all-solid-state Li^+ ion batteries.

5.2 Outlook

Through the significant progress demonstrated in this work the preliminary work required before the assembly of a full solid-state cell using sequential thin film deposition has been completed. Several important questions still remain to be answered about how the combination of all components will perform as a device.

A full solid-state battery using the solid electrolyte and current collector developed in this work would be important to be able to assess the real performance in the final application. Interfacial properties related to charge transfer, chemical stability and morphology could be studied here and comparisons to solid-state batteries made onto pellets of the electrolyte can be made.

Now that in-depth knowledge on the phase evolution of LLZO for thin films made by co-sputtering has been gathered, keeping the processing temperature of the entire cell to below 500°C may be possible as a low temperature strategy. With a study into low temperature cathode deposition the inter-diffusion of elements between each layer can be mitigated which is an important strategy. This would lower the interfacial resistance by preventing the formation of insulating phases and preserving the properties of each layer in the full solid-state battery stack.

Another question which is vital to the future application of LLZO into high performance solid-state batteries is why the lithium ion conductivity drops so dramatically when going to thin film regimes. Further elucidation here could lead to improvements of up to 2 orders of magnitude bringing the performance of such a layer up to the expected lithium ion conductivity of bulk LLZO pellets at $>1 \times 10^{-3} \text{ S cm}^{-1}$ for the Ga doped variety. Investigation into the porosity of thin films after processing and the effect of thermally induced strain on Li^+ ion conductivity may shed some light on the underlying causes.

The $\text{Cr}_{2.1}\text{N}$ current collector performed adequately in the final half-cell test however one of the key issues which limited performance was the diffusion of Cr into the cathode material which lowered the effective energy capacity of the cell. This could be prevented by including other elements into the current collector such as Al, which is well known to have very stable properties as an oxide, or by adding a diffusion barrier between the $\text{Cr}_{2.1}\text{N}$ and cathode which could be up to 2-3 nm thick to prevent too much interfacial resistance.

6 References

- 1 Volta, A. On the Electricity Excited by the Mere Contact of Conducting Substances of Different Kinds. In a Letter from Mr. Alexander Volta, F. R. S. Professor of Natural Philosophy in the University of Pavia, to the Rt. Hon. Sir Joseph Banks, Bart. K. B. P. R. S. *Philosophical Transactions of the Royal Society of London* **90**, 403-431, doi:10.1098/rstl.1800.0018 (1800).
- 2 Vlad, A., Singh, N., Galande, C. & Ajayan, P. M. Design Considerations for Unconventional Electrochemical Energy Storage Architectures. *Advanced Energy Materials* **5**, doi:10.1002/aenm.201402115 (2015).
- 3 Younesi, R., Veith, G. M., Johansson, P., Edstrom, K. & Vegge, T. Lithium salts for advanced lithium batteries: Li-metal, Li-O₂, and Li-S. *Energy Environ. Sci.* **8**, 1905-1922, doi:10.1039/C5EE01215E (2015).
- 4 Peled, E., Golodnitsky, D., Ardel, G. & Eshkenazy, V. THE SEI MODEL - APPLICATION TO LITHIUM POLYMER ELECTROLYTE BATTERIES. *Electrochimica Acta* **40**, 2197-2204, doi:10.1016/0013-4686(95)00163-9 (1995).
- 5 Adachi, G. Y., Imanaka, N. & Aono, H. Fast Li-circle plus conducting ceramic electrolytes. *Advanced Materials* **8**, 127-+, doi:10.1002/adma.19960080205 (1996).
- 6 Goodenough, J. B. & Kim, Y. Challenges for Rechargeable Li Batteries. *Chemistry of Materials* **22**, 587-603, doi:10.1021/cm901452z (2010).
- 7 Hu, M., Pang, X. L. & Zhou, Z. Recent progress in high-voltage lithium ion batteries. *Journal of Power Sources* **237**, 229-242, doi:10.1016/j.jpowsour.2013.03.024 (2013).
- 8 Bachman, J. C. *et al.* Inorganic Solid-State Electrolytes for Lithium Batteries: Mechanisms and Properties Governing Ion Conduction. *Chemical Reviews* **116**, 140-162, doi:10.1021/acs.chemrev.5b00563 (2016).
- 9 Kalhoff, J., Eshetu, G. G., Bresser, D. & Passerini, S. Safer Electrolytes for Lithium-Ion Batteries: State of the Art and Perspectives. *Chemsuschem* **8**, 2154-2175, doi:10.1002/cssc.201500284 (2015).
- 10 Oudenhoven, J. F. M., Baggetto, L. & Notten, P. H. L. All-Solid-State Lithium-Ion Microbatteries: A Review of Various Three-Dimensional Concepts. *Advanced Energy Materials* **1**, 10-33, doi:10.1002/aenm.201000002 (2011).
- 11 Sun, K. *et al.* 3D Printing of Interdigitated Li-Ion Microbattery Architectures. *Advanced Materials* **25**, 4539-4543, doi:10.1002/adma.201301036 (2013).
- 12 Kim, S. H. *et al.* Printable Solid-State Lithium-Ion Batteries: A New Route toward Shape-Conformable Power Sources with Aesthetic Versatility for Flexible Electronics. *Nano Letters* **15**, 5168-5177, doi:10.1021/acs.nanolett.5b01394 (2015).
- 13 Kato, Y. *et al.* High-power all-solid-state batteries using sulfide superionic conductors. *Nature Energy* **1**, doi:10.1038/nenergy.2016.30 (2016).
- 14 Wang, Z. Y. *et al.* In Situ STEM-EELS Observation of Nanoscale Interfacial Phenomena in All-Solid-State Batteries. *Nano Letters* **16**, 3760-3767, doi:10.1021/acs.nanolett.6b01119 (2016).
- 15 Wang, Y. *et al.* Lithium and lithium ion batteries for applications in microelectronic devices: A review. *Journal of Power Sources* **286**, 330-345, doi:<https://doi.org/10.1016/j.jpowsour.2015.03.164> (2015).
- 16 van den Broek, J., Afyon, S. & Rupp, J. L. M. Interface-Engineered All-Solid-State Li-Ion Batteries Based on Garnet-Type Fast Li⁺ Conductors. *Advanced Energy Materials* **6**, 1600736, doi:10.1002/aenm.201600736 (2016).

- 17 Manthiram, A., Chemelewski, K. & Lee, E.-S. A perspective on the high-voltage $\text{LiMn}_{1.5}\text{Ni}_{0.5}\text{O}_4$ spinel cathode for lithium-ion batteries. *Energy & Environmental Science* **7**, 1339-1350, doi:10.1039/C3EE42981D (2014).
- 18 Lobe, S. *et al.* Radio frequency magnetron sputtering of $\text{Li}_7\text{La}_3\text{Zr}_2\text{O}_{12}$ thin films for solid-state batteries. *Journal of Power Sources* **307**, 684-689, doi:<http://dx.doi.org/10.1016/j.jpowsour.2015.12.054> (2016).
- 19 Deng, J. *et al.* Electrochemical performance and kinetic behavior of lithium ion in $\text{Li}_4\text{Ti}_5\text{O}_{12}$ thin film electrodes. *Applied Surface Science* **314**, 936-941, doi:<https://doi.org/10.1016/j.apsusc.2014.06.162> (2014).
- 20 Li, T. K. & Ng, D. H. L. Fabrication of Al– LiAlO_2 metal matrix composites and crystalline γ - LiAlO_2 . *Materials Science and Engineering: A* **445–446**, 652-656, doi:<https://doi.org/10.1016/j.msea.2006.09.092> (2007).
- 21 Myung, S.-T., Hitoshi, Y. & Sun, Y.-K. Electrochemical behavior and passivation of current collectors in lithium-ion batteries. *Journal of Materials Chemistry* **21**, 9891-9911, doi:10.1039/C0JM04353B (2011).
- 22 Graham, M. J. & Cohen, M. On the Mechanism of Low-Temperature Oxidation (23°–450°C) of Polycrystalline Nickel. *Journal of The Electrochemical Society* **119**, 879-882, doi:10.1149/1.2404360 (1972).
- 23 Warren, A., Nylund, A. & Olefjord, I. Oxidation of tungsten and tungsten carbide in dry and humid atmospheres. *International Journal of Refractory Metals and Hard Materials* **14**, 345-353, doi:[http://dx.doi.org/10.1016/S0263-4368\(96\)00027-3](http://dx.doi.org/10.1016/S0263-4368(96)00027-3) (1996).
- 24 Hallström, S., Halvarsson, M., Höglund, L., Jonsson, T. & Ågren, J. High temperature oxidation of chromium: Kinetic modeling and microstructural investigation. *Solid State Ionics* **240**, 41-50, doi:<https://doi.org/10.1016/j.ssi.2013.02.017> (2013).
- 25 Komaba, S. *et al.* Preparation of Li–Mn–O thin films by r.f.-sputtering method and its application to rechargeable batteries. *Journal of Applied Electrochemistry* **30**, 1179-1182, doi:10.1023/A:1004047614084 (2000).
- 26 Pelton, A. D. The Au–Li (Gold-Lithium) system. *Bulletin of Alloy Phase Diagrams* **7**, 228-231, doi:10.1007/BF02868994 (1986).
- 27 Sangster, J. & Pelton, A. D. The li-pt (lithium-platinum) system. *Journal of Phase Equilibria* **12**, 678-681, doi:10.1007/BF02645170 (1991).
- 28 Freixas, J. *et al.* Sputtered Titanium Nitride: A Bifunctional Material for Li-Ion Microbatteries. *Journal of The Electrochemical Society* **162**, A493-A500, doi:10.1149/2.0051504jes (2015).
- 29 Chen, H.-Y. & Lu, F.-H. Oxidation behavior of titanium nitride films. *Journal of Vacuum Science & Technology A: Vacuum, Surfaces, and Films* **23**, 1006-1009, doi:10.1116/1.1914815 (2005).
- 30 Izquierdo, G. & West, A. R. Phase equilibria in the system Li_2O – TiO_2 . *Materials Research Bulletin* **15**, 1655-1660, doi:[http://dx.doi.org/10.1016/0025-5408\(80\)90248-2](http://dx.doi.org/10.1016/0025-5408(80)90248-2) (1980).
- 31 Zhang, G. A., Yan, P. X., Wang, P., Chen, Y. M. & Zhang, J. Y. Influence of nitrogen content on the structural, electrical and mechanical properties of CrN_x thin films. *Materials Science and Engineering: A* **460**, 301-305, doi:<http://dx.doi.org/10.1016/j.msea.2007.01.149> (2007).
- 32 Lin, J., Sproul, W. D., Moore, J. J., Lee, S. & Myers, S. High rate deposition of thick CrN and Cr₂N coatings using modulated pulse power (MPP) magnetron sputtering. *Surface and Coatings Technology* **205**, 3226-3234, doi:<http://dx.doi.org/10.1016/j.surfcoat.2010.11.039> (2011).
- 33 Ernst, W. *et al.* Thermal decomposition routes of CrN hard coatings synthesized by reactive arc evaporation and magnetron sputtering. *Thin Solid Films* **517**, 568-574, doi:<http://dx.doi.org/10.1016/j.tsf.2008.06.086> (2008).

- 34 Cabana, J. *et al.* Antifluorite-Type Lithium Chromium Oxide Nitrides: Synthesis, Structure, Order, and Electrochemical Properties. *Inorganic Chemistry* **43**, 7050-7060, doi:10.1021/ic049138z (2004).
- 35 Héau, C., Fillit, R. Y., Vaux, F. & Pascaretti, F. Study of thermal stability of some hard nitride coatings deposited by reactive magnetron sputtering. *Surface and Coatings Technology* **120**, 200-205, doi:[http://dx.doi.org/10.1016/S0257-8972\(99\)00456-9](http://dx.doi.org/10.1016/S0257-8972(99)00456-9) (1999).
- 36 Qi, Z. B. *et al.* A comparative study of the oxidation behavior of Cr₂N and CrN coatings. *Thin Solid Films* **544**, 515-520, doi:<http://dx.doi.org/10.1016/j.tsf.2013.01.031> (2013).
- 37 Islam, M. S. & Fisher, C. A. J. Lithium and sodium battery cathode materials: computational insights into voltage, diffusion and nanostructural properties. *Chemical Society Reviews* **43**, 185-204, doi:10.1039/C3CS60199D (2014).
- 38 Cho, J., Kim, Y.-W., Kim, B., Lee, J.-G. & Park, B. A Breakthrough in the Safety of Lithium Secondary Batteries by Coating the Cathode Material with AlPO₄ Nanoparticles. *Angewandte Chemie International Edition* **42**, 1618-1621, doi:10.1002/anie.200250452 (2003).
- 39 Ohzuku, T., Ariyoshi, K. & Yamamoto, S. Synthesis and Characterization of LiNi_{0.5}Mn_{1.5}O₄ by Two-Step Solid State Reaction. *Journal of the Ceramic Society of Japan* **110**, 501-505, doi:10.2109/jcersj.110.501 (2002).
- 40 Myung, S.-T. *et al.* Nickel-Rich Layered Cathode Materials for Automotive Lithium-Ion Batteries: Achievements and Perspectives. *ACS Energy Lett.* **2**, 196-223, doi:10.1021/acsenergylett.6b00594 (2017).
- 41 Lin, F. *et al.* Surface reconstruction and chemical evolution of stoichiometric layered cathode materials for lithium-ion batteries. *Nature Communications* **5**, 3529, doi:10.1038/ncomms4529 (2014).
- 42 Hanafusa, R., Oka, Y. & Nakamura, T. Electrochemical and Magnetic Studies of Li-Deficient Li_{1-x}Co_{1-x}FexPO₄ Olivine Cathode Compounds. *Journal of The Electrochemical Society* **162**, A3045-A3051, doi:10.1149/2.0071502jes (2015).
- 43 Doughty, D. H. & Roth, E. P. A General Discussion of Li Ion Battery Safety. *The Electrochemical Society Interface* **21**, 37-44, doi:10.1149/2.F03122if (2012).
- 44 Xu, W. *et al.* Lithium metal anodes for rechargeable batteries. *Energy & Environmental Science* **7**, 513-537, doi:10.1039/C3EE40795K (2014).
- 45 Besenhard, J. O. *Handbook of Battery Materials*. (John Wiley & Sons, 2008).
- 46 Ohara, S., Suzuki, J., Sekine, K. & Takamura, T. Li insertion/extraction reaction at a Si film evaporated on a Ni foil. *Journal of Power Sources* **119-121**, 591-596, doi:[https://doi.org/10.1016/S0378-7753\(03\)00301-X](https://doi.org/10.1016/S0378-7753(03)00301-X) (2003).
- 47 Omampuliyur, R. S. *et al.* Nanostructured Thin Film Silicon Anodes for Li-Ion Microbatteries. *Journal of Nanoscience and Nanotechnology* **15**, 4926-4933, doi:10.1166/jnn.2015.9831 (2015).
- 48 Richards, W. D., Miara, L. J., Wang, Y., Kim, J. C. & Ceder, G. Interface Stability in Solid-State Batteries. *Chemistry of Materials* **28**, 266-273, doi:10.1021/acs.chemmater.5b04082 (2016).
- 49 Murugan, R., Thangadurai, V. & Weppner, W. Fast lithium ion conduction in garnet-type Li₇La₃Zr₂O₁₂. *Angewandte Chemie-International Edition* **46**, 7778-7781, doi:10.1002/anie.200701144 (2007).
- 50 Yu, X. H., Bates, J. B., Jellison, G. E. & Hart, F. X. A stable thin-film lithium electrolyte: Lithium phosphorus oxynitride. *Journal of the Electrochemical Society* **144**, 524-532, doi:10.1149/1.1837443 (1997).
- 51 Chen, C. H. & Amine, K. Ionic conductivity, lithium insertion and extraction of lanthanum lithium titanate. *Solid State Ionics* **144**, 51-57, doi:10.1016/S0167-2738(01)00884-0 (2001).

- 52 Aguesse, F. *et al.* Microstructure and ionic conductivity of LLTO thin films: Influence of different substrates and excess lithium in the target. *Solid State Ionics* **272**, 1-8, doi:10.1016/j.ssi.2014.12.005 (2015).
- 53 Mo, Y., Ong, S. P. & Ceder, G. First Principles Study of the Li₁₀GeP₂S₁₂ Lithium Super Ionic Conductor Material. *Chemistry of Materials* **24**, 15-17, doi:10.1021/cm203303y (2012).
- 54 Kato, T. *et al.* In-situ Li₇La₃Zr₂O₁₂/LiCoO₂ interface modification for advanced all-solid-state battery. *Journal of Power Sources* **260**, 292-298, doi:10.1016/j.jpowsour.2014.02.102 (2014).
- 55 Okada, K. *et al.* Preparation and electrochemical properties of LiAlO₂-coated Li(Ni_{1/3}Mn_{1/3}Co_{1/3})O₂ for all-solid-state batteries. *Solid State Ionics* **255**, 120-127, doi:10.1016/j.ssi.2013.12.019 (2014).
- 56 Luo, W. *et al.* Transition from Superlithiophobicity to Superlithiophilicity of Garnet Solid-State Electrolyte. *Journal of the American Chemical Society* **138**, 12258-12262, doi:10.1021/jacs.6b06777 (2016).
- 57 Han, X. *et al.* Negating interfacial impedance in garnet-based solid-state Li metal batteries. *Nat Mater* **advance online publication** (2016).
- 58 Inaguma, Y. *et al.* High Ionic-Conductivity in Lithium Lanthanum Titanate. *Solid State Communications* **86**, 689-693, doi:10.1016/0038-1098(93)90841-a (1993).
- 59 Thompson, T. *et al.* Electrochemical Window of the Li-Ion Solid Electrolyte Li₇La₃Zr₂O₁₂. *ACS Energy Lett.* **2**, 462-468, doi:10.1021/acsenerylett.6b00593 (2017).
- 60 Awaka, J. *et al.* Crystal Structure of Fast Lithium-ion-conducting Cubic Li₇La₃Zr₂O₁₂. *Chemistry Letters* **40**, 60-62, doi:10.1246/cl.2011.60 (2011).
- 61 Awaka, J., Kijima, N., Hayakawa, H. & Akimoto, J. Synthesis and structure analysis of tetragonal Li₇La₃Zr₂O₁₂ with the garnet-related type structure. *Journal of Solid State Chemistry* **182**, 2046-2052, doi:10.1016/j.jssc.2009.05.020 (2009).
- 62 Geiger, C. A. *et al.* Crystal Chemistry and Stability of "Li₇La₃Zr₂O₁₂" Garnet: A Fast Lithium-Ion Conductor. *Inorganic Chemistry* **50**, 1089-1097, doi:10.1021/ic101914e (2011).
- 63 Buschmann, H. *et al.* Structure and dynamics of the fast lithium ion conductor "Li₇La₃Zr₂O₁₂". *Physical Chemistry Chemical Physics* **13**, 19378-19392, doi:10.1039/c1cp22108f (2011).
- 64 Rangasamy, E., Wolfenstine, J. & Sakamoto, J. The role of Al and Li concentration on the formation of cubic garnet solid electrolyte of nominal composition Li₇La₃Zr₂O₁₂. *Solid State Ionics* **206**, 28-32, doi:<http://dx.doi.org/10.1016/j.ssi.2011.10.022> (2012).
- 65 Huang, M. A. *et al.* Effect of sintering temperature on structure and ionic conductivity of Li_(7-x)La₃Zr₂O_(12-0.5x) (x=0.5 similar to 0.7) ceramics. *Solid State Ionics* **204**, 41-45, doi:10.1016/j.ssi.2011.10.003 (2011).
- 66 Kotobuki, M., Kanamura, K., Sato, Y. & Yoshida, T. Fabrication of all-solid-state lithium battery with lithium metal anode using Al₂O₃-added Li₇La₃Zr₂O₁₂ solid electrolyte. *Journal of Power Sources* **196**, 7750-7754, doi:<http://dx.doi.org/10.1016/j.jpowsour.2011.04.047> (2011).
- 67 Ohta, S., Kobayashi, T. & Asaoka, T. High lithium ionic conductivity in the garnet-type oxide Li_{7-X}La₃(Zr_{2-X}Nb_X)O₁₂ (X=0-2). *Journal of Power Sources* **196**, 3342-3345, doi:10.1016/j.jpowsour.2010.11.089 (2011).
- 68 Kokal, I., Somer, M., Notten, P. H. L. & Hintzen, H. T. Sol-gel synthesis and lithium ion conductivity of Li₇La₃Zr₂O₁₂ with garnet-related type structure. *Solid State Ionics* **185**, 42-46, doi:<https://doi.org/10.1016/j.ssi.2011.01.002> (2011).

- 69 Jin, Y. & McGinn, P. J. Al-doped Li₇La₃Zr₂O₁₂ synthesized by a polymerized complex method. *Journal of Power Sources* **196**, 8683-8687, doi:10.1016/j.jpowsour.2011.05.065 (2011).
- 70 Li, Y. *et al.* Ionic distribution and conductivity in lithium garnet Li₇La₃Zr₂O₁₂. *Journal of Power Sources* **209**, 278-281, doi:<http://dx.doi.org/10.1016/j.jpowsour.2012.02.100> (2012).
- 71 Takano, R., Tadanaga, K., Hayashi, A. & Tatsumisago, M. Low temperature synthesis of Al-doped Li₇La₃Zr₂O₁₂ solid electrolyte by a sol-gel process. *Solid State Ionics* **255**, 104-107, doi:<http://dx.doi.org/10.1016/j.ssi.2013.12.006> (2014).
- 72 Düvel, A., Kuhn, A., Robben, L., Wilkening, M. & Heitjans, P. Mechano-synthesis of Solid Electrolytes: Preparation, Characterization, and Li Ion Transport Properties of Garnet-Type Al-Doped Li₇La₃Zr₂O₁₂ Crystallizing with Cubic Symmetry. *The Journal of Physical Chemistry C* **116**, 15192-15202, doi:10.1021/jp301193r (2012).
- 73 David, I. N., Thompson, T., Wolfenstine, J., Allen, J. L. & Sakamoto, J. Microstructure and Li-Ion Conductivity of Hot-Pressed Cubic Li₇La₃Zr₂O₁₂. *Journal of the American Ceramic Society* **98**, 1209-1214, doi:10.1111/jace.13455 (2015).
- 74 Rosenkiewitz, N., Schuhmacher, J., Bockmeyer, M. & Deubener, J. Nitrogen-free sol-gel synthesis of Al-substituted cubic garnet Li₇La₃Zr₂O₁₂ (LLZO). *Journal of Power Sources* **278**, 104-108, doi:<http://dx.doi.org/10.1016/j.jpowsour.2014.12.066> (2015).
- 75 Raskovalov, A. A., Il'ina, E. A. & Antonov, B. D. Structure and transport properties of Li₇La₃Zr₂-0.75xAl_xO₁₂ superionic solid electrolytes. *Journal of Power Sources* **238**, 48-52, doi:<http://dx.doi.org/10.1016/j.jpowsour.2013.03.049> (2013).
- 76 Shimonishi, Y. *et al.* Synthesis of garnet-type Li_{7-x}La₃Zr₂O_{12-1/2x} and its stability in aqueous solutions. *Solid State Ionics* **183**, 48-53, doi:<http://dx.doi.org/10.1016/j.ssi.2010.12.010> (2011).
- 77 Thompson, T. *et al.* Tetragonal vs. cubic phase stability in Al - free Ta doped Li₇La₃Zr₂O₁₂ (LLZO). *Journal of Materials Chemistry A* **2**, 13431-13436, doi:10.1039/C4TA02099E (2014).
- 78 Liu, C. *et al.* Reversible ion exchange and structural stability of garnet-type Nb-doped Li₇La₃Zr₂O₁₂ in water for applications in lithium batteries. *Journal of Power Sources* **282**, 286-293, doi:10.1016/j.jpowsour.2015.02.050 (2015).
- 79 Hitz, G. T., Wachsman, E. D. & Thangadurai, V. Highly Li-Stuffed Garnet-Type Li_{7+x}La₃Zr_{2-x}Y_xO₁₂. *Journal of the Electrochemical Society* **160**, A1248-A1255, doi:10.1149/2.088308jes (2013).
- 80 Matsuda, Y. *et al.* Phase relation, structure and ionic conductivity of Li_{7-x-3y}Al_yLa₃Zr_{2-x}Ta_xO₁₂. *Rsc Advances* **6**, 78210-78218, doi:10.1039/c6ra13317g (2016).
- 81 Rettenwander, D. *et al.* Structural and Electrochemical Consequences of Al and Ga Cosubstitution in Li(7)La(3)Zr(2)O(12) Solid Electrolytes. *Chemistry of Materials* **28**, 2384-2392, doi:10.1021/acs.chemmater.6b00579 (2016).
- 82 Shin, D. O. *et al.* Synergistic multi-doping effects on the Li₇La₃Zr₂O₁₂ solid electrolyte for fast lithium ion conduction. *Scientific Reports* **5**, doi:10.1038/srep18053 (2015).
- 83 Cao, Z. *et al.* Effect of Sb-Ba codoping on the ionic conductivity of Li₇La₃Zr₂O₁₂ ceramic. *Ceramics International* **41**, 6232-6236, doi:<https://doi.org/10.1016/j.ceramint.2015.01.030> (2015).
- 84 Gu, W., Ezbiri, M., Rao, R. P., Avdeev, M. & Adams, S. Effects of penta- and trivalent dopants on structure and conductivity Of Li₇La₃Zr₂O₁₂. *Solid State Ionics* **274**, 100-105, doi:10.1016/j.ssi.2015.03.019 (2015).

- 85 Tong, X., Thangadurai, V. & Wachsman, E. D. Highly Conductive Li Garnets by a Multielement Doping Strategy. *INORGANIC CHEMISTRY* **54**, 3600-3607, doi:10.1021/acs.inorgchem.5b00184 (2015).
- 86 Dhivya, L. & Murugan, R. Effect of Simultaneous Substitution of Y and Ta on the Stabilization of Cubic Phase, Microstructure, and Li⁺ Conductivity of Li₇La₃Zr₂O₁₂ Lithium Garnet. *ACS APPLIED MATERIALS & INTERFACES* **6**, 17606-17615, doi:10.1021/am503731h (2014).
- 87 Wagner, R. *et al.* Crystal Structure of Garnet-Related Li-Ion Conductor Li_{7-3x}Ga_xLa₃Zr₂O₁₂: Fast Li-Ion Conduction Caused by a Different Cubic Modification? *Chemistry of Materials* **28**, 1861-1871, doi:10.1021/acs.chemmater.6b00038 (2016).
- 88 Wu, J. F. *et al.* Gallium-Doped Li₇La₃Zr₂O₁₂ Garnet-Type Electrolytes with High Lithium-Ion Conductivity. *Acs Applied Materials & Interfaces* **9**, 1542-1552, doi:10.1021/acsami.6b13902 (2017).
- 89 Bernuy-Lopez, C. *et al.* Atmosphere Controlled Processing of Ga-Substituted Garnets for High Li-Ion Conductivity Ceramics. *Chemistry of Materials* **26**, 3610-3617, doi:10.1021/cm5008069 (2014).
- 90 Jalem, R. *et al.* Effects of Gallium Doping in Garnet-Type Li₇La₃Zr₂O₁₂ Solid Electrolytes. *Chemistry of Materials* **27**, 2821-2831, doi:10.1021/cm5045122 (2015).
- 91 Afyon, S., Krumeich, F. & Rupp, J. L. M. A shortcut to garnet-type fast Li-ion conductors for all-solid state batteries. *Journal of Materials Chemistry A* **3**, 18636-18648, doi:10.1039/C5TA03239C (2015).
- 92 Wagner, R. *et al.* Fast Li-Ion-Conducting Garnet-Related Li_{7-3x}FexLa₃Zr₂O₁₂ with Uncommon I(4)_{over-bar}3d Structure. *Chemistry of Materials* **28**, 5943-5951, doi:10.1021/acs.chemmater.6b02516 (2016).
- 93 Wolfenstine, J., Rangasamy, E., Allen, J. L. & Sakamoto, J. High conductivity of dense tetragonal Li₇La₃Zr₂O₁₂. *Journal of Power Sources* **208**, 193-196, doi:<https://doi.org/10.1016/j.jpowsour.2012.02.031> (2012).
- 94 Zhang, Y., Chen, F., Tu, R., Shen, Q. & Zhang, L. Field assisted sintering of dense Al-substituted cubic phase Li₇La₃Zr₂O₁₂ solid electrolytes. *Journal of Power Sources* **268**, 960-964, doi:<https://doi.org/10.1016/j.jpowsour.2014.03.148> (2014).
- 95 Kubicek, M. *et al.* Oxygen Vacancies in Fast Lithium-Ion Conducting Garnets. *Chemistry of Materials* **29**, 7189-7196, doi:10.1021/acs.chemmater.7b01281 (2017).
- 96 Kim, S., Hirayama, M., Taminato, S. & Kanno, R. Epitaxial growth and lithium ion conductivity of lithium-oxide garnet for an all solid-state battery electrolyte. *Dalton Transactions* **42**, 13112-13117, doi:10.1039/C3DT51795K (2013).
- 97 Tan, J. J. & Tiwari, A. Fabrication and Characterization of Li₇La₃Zr₂O₁₂ Thin Films for Lithium Ion Battery. *Ecs Solid State Letters* **1**, Q57-Q60, doi:10.1149/2.013206ssl (2012).
- 98 Rawlence, M., Garbayo, I., Buecheler, S. & Rupp, J. L. M. On the chemical stability of post-lithiated garnet Al-stabilized Li₇La₃Zr₂O₁₂ solid state electrolyte thin films. *Nanoscale* **8**, 14746-14753, doi:10.1039/c6nr04162k (2016).
- 99 Park, J. S. *et al.* Effects of crystallinity and impurities on the electrical conductivity of Li-La-Zr-O thin films. *Thin Solid Films* **576**, 55-60, doi:<http://dx.doi.org/10.1016/j.tsf.2014.11.019> (2015).
- 100 Garbayo, I., Struzik, M., Pfenninger, R., Bowman, W. & Rupp, J. L. M. Glass-Type Polyamorphism in Li-Garnet Thin Film Solid State Battery Conductors. (2017).
- 101 Kalita, D. J., Lee, S. H., Lee, K. S., Ko, D. H. & Yoon, Y. S. Ionic conductivity properties of amorphous Li-La-Zr-O solid electrolyte for thin film batteries. *Solid State Ionics* **229**, 14-19, doi:10.1016/j.ssi.2012.09.011 (2012).

- 102 Ahn, C. W. *et al.* Microstructure and Ionic Conductivity in Li₇La₃Zr₂O₁₂ Film Prepared by Aerosol Deposition Method. *Journal of the Electrochemical Society* **162**, A60-A63, doi:10.1149/2.0411501jes (2015).
- 103 Tadanaga, K. *et al.* Preparation of lithium ion conductive Al-doped Li₇La₃Zr₂O₁₂ thin films by a sol-gel process. *Journal of Power Sources* **273**, 844-847, doi:10.1016/j.jpowsour.2014.09.164 (2015).
- 104 Chen, R.-J. *et al.* Sol-gel derived Li-La-Zr-O thin films as solid electrolytes for lithium-ion batteries. *Journal of Materials Chemistry A* **2**, 13277-13282, doi:10.1039/C4TA02289K (2014).
- 105 Bitzer, M., Van Gestel, T., Uhlenbruck, S. & Hans Peter, B. Sol-gel synthesis of thin solid Li₇La₃Zr₂O₁₂ electrolyte films for Li-ion batteries. *THIN SOLID FILMS* **615**, 128-134, doi:10.1016/j.tsf.2016.07.010 (2016).
- 106 Katsui, H. & Goto, T. Preparation of cubic and tetragonal Li₇La₃Zr₂O₁₂ film by metal organic chemical vapor deposition. *Thin Solid Films* **584**, 130-134, doi:<http://dx.doi.org/10.1016/j.tsf.2014.11.094> (2015).
- 107 Langer, F., Glenneberg, J., Bardenhagen, I. & Kun, R. Synthesis of single phase cubic Al-substituted Li₇La₃Zr₂O₁₂ by solid state lithiation of mixed hydroxides. *Journal of Alloys and Compounds* **645**, 64-69, doi:<http://dx.doi.org/10.1016/j.jallcom.2015.03.209> (2015).
- 108 Chen, R.-J. *et al.* Effect of calcining and Al doping on structure and conductivity of Li₇La₃Zr₂O₁₂. *Solid State Ionics* **265**, 7-12, doi:<http://dx.doi.org/10.1016/j.ssi.2014.07.004> (2014).
- 109 Rupp, J. L. M., Scherrer, B. & Gauckler, L. J. Engineering disorder in precipitation-based nano-scaled metal oxide thin films. *Physical Chemistry Chemical Physics* **12**, 11114-11124, doi:10.1039/b920971a (2010).
- 110 Huber, T. M., Opitz, A. K. & Fleig, J. Oxygen reduction via grain boundary transport in thin film platinum electrodes on yttria stabilized zirconia. *Solid State Ionics* **273**, 8-12, doi:<http://dx.doi.org/10.1016/j.ssi.2014.11.006> (2015).
- 111 Ryll, T. *et al.* Microscopic and Nanoscopic Three-Phase-Boundaries of Platinum Thin-Film Electrodes on YSZ Electrolyte. *Advanced Functional Materials* **21**, 565-572, doi:10.1002/adfm.201001729 (2011).
- 112 Cheng, L. *et al.* Effect of microstructure and surface impurity segregation on the electrical and electrochemical properties of dense Al-substituted Li₇La₃Zr₂O₁₂. *Journal of Materials Chemistry A* **2**, 172-181, doi:10.1039/C3TA13999A (2014).
- 113 Chen, Y. *et al.* Segregated Chemistry and Structure on (001) and (100) Surfaces of (La_{1-x}Sr_x)₂CoO₄ Override the Crystal Anisotropy in Oxygen Exchange Kinetics. *Chemistry of Materials* **27**, 5436-5450, doi:10.1021/acs.chemmater.5b02292 (2015).
- 114 Kubicek, M. *et al.* Tensile Lattice Strain Accelerates Oxygen Surface Exchange and Diffusion in La_{1-x}Sr_xCoO_{3-delta} Thin Films. *Acs Nano* **7**, 3276-3286, doi:10.1021/nn305987x (2013).
- 115 Schweiger, S., Kubicek, M., Messerschmitt, F., Murer, C. & Rupp, J. L. M. A Microdot Multilayer Oxide Device: Let Us Tune the Strain-Ionic Transport Interaction. *Acs Nano* **8**, 5032-5048, doi:10.1021/nn501128y (2014).
- 116 Shi, Y. U., Bork, A. H., Schweiger, S. & Rupp, J. L. M. The effect of mechanical twisting on oxygen ionic transport in solid-state energy conversion membranes. *Nature Materials* **14**, 721+, doi:10.1038/nmat4278 (2015).
- 117 Yang, T., Gordon, Z. D., Li, Y. & Chan, C. K. Nanostructured Garnet-Type Solid Electrolytes for Lithium Batteries: Electrospinning Synthesis of Li₇La₃Zr₂O₁₂ Nanowires and Particle Size-Dependent Phase Transformation. *Journal of Physical Chemistry C* **119**, 14947-14953, doi:10.1021/acs.jpcc.5b03589 (2015).

- 118 Gribb, A. A. & Banfield, J. F. Particle size effects on transformation kinetics and phase stability in nanocrystalline TiO₂. *American Mineralogist* **82**, 717-728 (1997).
- 119 Zhang, Y. L. *et al.* The size dependence of structural stability in nano-sized ZrO₂ particles. *Materials Science and Engineering a-Structural Materials Properties Microstructure and Processing* **438**, 399-402, doi:10.1016/j.msea.2006.03.109 (2006).
- 120 Scherrer, B. *et al.* Crystallization and Microstructure of Yttria-Stabilized-Zirconia Thin Films Deposited by Spray Pyrolysis. *Advanced Functional Materials* **21**, 3967-3975, doi:10.1002/adfm.201101268 (2011).
- 121 Frison, R. *et al.* Crystallization of 8 mol% yttria-stabilized zirconia thin-films deposited by RF-sputtering. *Solid State Ionics* **232**, 29-36, doi:10.1016/j.ssi.2012.11.014 (2013).
- 122 Scherrer, B. *et al.* Microstructures of YSZ and CGO Thin Films Deposited by Spray Pyrolysis: Influence of Processing Parameters on the Porosity. *Advanced Functional Materials* **22**, 3509-3518, doi:10.1002/adfm.201200454 (2012).
- 123 D.B. Chrisey, G. K. H. Pulsed Laser Deposition of Thin Films. *Wiley-Interscience* (1994).
- 124 Schou, J. Physical aspects of the pulsed laser deposition technique: The stoichiometric transfer of material from target to film. *Applied Surface Science* **255**, 5191-5198, doi:<http://dx.doi.org/10.1016/j.apsusc.2008.10.101> (2009).
- 125 Rettenwander, D. *et al.* Site Occupation of Ga and Al in Stabilized Cubic Li_{7-3(x plus y)Ga_xAl_yLa₃Zr₂O₁₂} Garnets As Deduced from (27)Al and Ga-71 MAS NMR at Ultrahigh Magnetic Fields. *Chemistry of Materials* **27**, 3135-3142, doi:10.1021/acs.chemmater.5b00684 (2015).
- 126 Cheng, L. *et al.* Interrelationships among Grain Size, Surface Composition, Air Stability, and Interfacial Resistance of Al-Substituted Li₇La₃Zr₂O₁₂ Solid Electrolytes. *ACS Applied Materials & Interfaces* **7**, 17649-17655, doi:10.1021/acsami.5b02528 (2015).
- 127 Kong, L. *et al.* A Novel Chemical Route to Prepare La₂Zr₂O₇ Pyrochlore. *Journal of the American Ceramic Society* **96**, 935-941, doi:10.1111/jace.12060 (2013).
- 128 Allen, J. L., Wolfenstine, J., Rangasamy, E. & Sakamoto, J. Effect of substitution (Ta, Al, Ga) on the conductivity of Li₇La₃Zr₂O₁₂. *Journal of Power Sources* **206**, 315-319, doi:10.1016/j.jpowsour.2012.01.131 (2012).
- 129 Danielson, D. T., Sparacin, D. K., Michel, J. & Kimerling, L. C. Surface-energy-driven dewetting theory of silicon-on-insulator agglomeration. *Journal of Applied Physics* **100**, 083507, doi:10.1063/1.2357345 (2006).
- 130 Ou, G., Liu, W., Yao, L., Wu, H. & Pan, W. High conductivity of La₂Zr₂O₇ nanofibers by phase control. *Journal of Materials Chemistry A* **2**, 1855-1861, doi:10.1039/C3TA13465B (2014).
- 131 Islam, Q. A., Nag, S. & Basu, R. N. Study of electrical conductivity of Ca-substituted La₂Zr₂O₇. *Materials Research Bulletin* **48**, 3103-3107, doi:<http://dx.doi.org/10.1016/j.materresbull.2013.04.081> (2013).
- 132 Labrincha, J. A., Frade, J. R. & Marques, F. M. B. Protonic conduction in La₂Zr₂O₇-based pyrochlore materials. *Solid State Ionics* **99**, 33-40, doi:10.1016/s0167-2738(97)00198-7 (1997).
- 133 Matsui, M. *et al.* Phase stability of a garnet-type lithium ion conductor Li₇La₃Zr₂O₁₂. *Dalton Trans.* **43**, 1019-1024, doi:10.1039/C3DT52024B (2014).
- 134 Lotgering, F. K. Topotactical Reactions with Ferrimagnetic Oxides Having Hexagonal Crystal Structures .1. *Journal of Inorganic & Nuclear Chemistry* **9**, 113-+, doi:10.1016/0022-1902(59)80070-1 (1959).
- 135 Howard, M. A. *et al.* Effect of Ga incorporation on the structure and Li ion conductivity of La₃Zr₂Li₇O₁₂. *Dalton Transactions* **41**, 12048-12053, doi:10.1039/c2dt31318a (2012).

- 136 Sunding, M. F. *et al.* XPS characterisation of in situ treated lanthanum oxide and hydroxide using tailored charge referencing and peak fitting procedures. *Journal of Electron Spectroscopy and Related Phenomena* **184**, 399-409, doi:10.1016/j.elspec.2011.04.002 (2011).
- 137 Imada, S. & Jo, T. Multiplet Structures in the 3D and 4D Core Photoemission Spectra for La Compounds. *Journal of the Physical Society of Japan* **58**, 402-405, doi:10.1143/jpsj.58.402 (1989).
- 138 Jorgensen, C. K. PHOTO-ELECTRON SPECTROMETRY OF INORGANIC SOLIDS. *Chimia* **25**, 213-+ (1971).
- 139 Signorelli, A. J. & Hayes, R. G. X-Ray Photoelectron Spectroscopy of Various Core Levels of Lanthanide Ions - Roles of Monopole Excitation and Electrostatic Coupling. *Physical Review B* **8**, 81-86, doi:10.1103/PhysRevB.8.81 (1973).
- 140 Taillades, G., Benjelloun, N., Sarradin, J. & Ribes, M. Metal-based very thin film anodes for lithium ion microbatteries. *Solid State Ionics* **152–153**, 119-124, doi:[http://dx.doi.org/10.1016/S0167-2738\(02\)00360-0](http://dx.doi.org/10.1016/S0167-2738(02)00360-0) (2002).
- 141 Toll, J. S. Causality and the Dispersion Relation - Logical Foundations. *Physical Review* **104**, 1760-1770, doi:10.1103/PhysRev.104.1760 (1956).
- 142 Grant, R. J., Ingram, M. D. & West, A. R. An investigation of β -alumina electrolytes by electric modulus spectroscopy. *Electrochimica Acta* **22**, 729-734, doi:[https://doi.org/10.1016/0013-4686\(77\)80027-3](https://doi.org/10.1016/0013-4686(77)80027-3) (1977).
- 143 Turkdogan, E. & Ignatowicz, S. The solubility of nitrogen in iron-chromium alloys. *J. of the Iron and Steel Inst*, 242-247 (1958).
- 144 Morris, M. C. *et al.* in *Standard X-ray Diffraction Powder Patterns*, U.S. Department of Commerce/National Bureau of Standards (Washington DC, 1985).
- 145 Brümmer, O. & Michel, W. in *Phys. Verh.* Vol. 12 19 (1961).
- 146 Furushima, R., Tanaka, S., Kato, Z. & Uematsu, K. Orientation distribution–Lotgering factor relationship in a polycrystalline material—as an example of bismuth titanate prepared by a magnetic field. *Journal of the Ceramic Society of Japan* **118**, 921-926, doi:10.2109/jcersj2.118.921 (2010).
- 147 Guéguen, A. *et al.* Decomposition of LiPF₆ in High Energy Lithium-Ion Batteries Studied with Online Electrochemical Mass Spectrometry. *Journal of The Electrochemical Society* **163**, A1095-A1100, doi:10.1149/2.0981606jes (2016).
- 148 Thornton, J. A. in *31st Annual Technical Symposium on Optical and Optoelectronic Applied Sciences and Engineering*. (SPIE).
- 149 Shin, D. W., Bridges, C. A., Huq, A., Paranthaman, M. P. & Manthiram, A. Role of Cation Ordering and Surface Segregation in High-Voltage Spinel LiMn_{1.5}Ni_{0.5}–xM_xO₄ (M = Cr, Fe, and Ga) Cathodes for Lithium-Ion Batteries. *Chemistry of Materials* **24**, 3720-3731, doi:10.1021/cm301844w (2012).
- 150 Čejka, J., Corma, A. & Zones, S. *Zeolites and catalysis: synthesis, reactions and applications*. (Wiley-VCH, 2010).
- 151 Baggetto, L., Unocic, R. R., Dudney, N. J. & Veith, G. M. Fabrication and characterization of Li–Mn–Ni–O sputtered thin film high voltage cathodes for Li-ion batteries. *Journal of Power Sources* **211**, 108-118, doi:10.1016/j.jpowsour.2012.03.076 (2012).
- 152 Arunkumar, T. A. & Manthiram, A. Influence of chromium doping on the electrochemical performance of the 5V spinel cathode LiMn_{1.5}Ni_{0.5}O₄. *Electrochimica Acta* **50**, 5568-5572, doi:<https://doi.org/10.1016/j.electacta.2005.03.033> (2005).

- 153 Park, M., Zhang, X., Chung, M., Less, G. B. & Sastry, A. M. A review of conduction phenomena in Li-ion batteries. *Journal of Power Sources* **195**, 7904-7929, doi:<https://doi.org/10.1016/j.jpowsour.2010.06.060> (2010).
- 154 Caballero, A. *et al.* LiNi_{0.5}Mn_{1.5}O₄ thick-film electrodes prepared by electrophoretic deposition for use in high voltage lithium-ion batteries. *Journal of Power Sources* **158**, 583-590, doi:<https://doi.org/10.1016/j.jpowsour.2005.09.018> (2006).
- 155 Yang, L., Ravdel, B. & Lucht, B. L. Electrolyte Reactions with the Surface of High Voltage LiNi_{0.5}Mn_{1.5}O₄ Cathodes for Lithium-Ion Batteries. *Electrochemical and Solid-State Letters* **13**, A95-A97, doi:10.1149/1.3428515 (2010).
- 156 Wu, Q. *et al.* Improved electrochemical performance of spinel LiMn_{1.5}Ni_{0.5}O₄ through MgF₂ nano-coating. *Nanoscale* **7**, 15609-15617, doi:10.1039/C5NR03564C (2015).
- 157 Cho, H.-M., Chen, M. V., MacRae, A. C. & Meng, Y. S. Effect of surface modification on nano-structured LiNi_{0.5}Mn_{1.5}O₄ spinel materials. *ACS applied materials & interfaces* **7**, 16231-16239 (2015).
- 158 Yi, T.-F. *et al.* Recent developments in the doping of LiNi_{0.5}Mn_{1.5}O₄ cathode material for 5 V lithium-ion batteries. *Ionics* **17**, 383-389, doi:10.1007/s11581-011-0550-6 (2011).
- 159 Li, J., Ma, C., Chi, M., Liang, C. & Dudney, N. J. Solid Electrolyte: the Key for High-Voltage Lithium Batteries. *Advanced Energy Materials* **5**, 1401408, doi:10.1002/aenm.201401408 (2015).
- 160 Macdonald, J. R. The Ngai coupling model of relaxation: Generalizations, alternatives, and their use in the analysis of non-Arrhenius conductivity in glassy, fast-ionic materials. *Journal of Applied Physics* **84**, 812-827, doi:10.1063/1.368142 (1998).
- 161 Cramer, C. *et al.* Ion Dynamics in Glass-Forming Systems .2. Conductivity Spectra Above the Glass Transformation Temperature. *Philosophical Magazine B-Physics of Condensed Matter Statistical Mechanics Electronic Optical and Magnetic Properties* **71**, 713-719, doi:10.1080/01418639508238561 (1995).
- 162 Cuervo-Reyes, E. Why the dipolar response in dielectrics and spin-glasses is unavoidably universal. *Scientific Reports* **6**, 29021 (2016).
- 163 Ngai, K. L., Greaves, G. N. & Moynihan, C. T. Correlation between the Activation Energies for Ionic Conductivity for Short and Long Time Scales and the Kohlrausch Stretching Parameter β for Ionically Conducting Solids and Melts. *Phys. Rev. Lett.* **80**, 1018-1021, doi:10.1103/PhysRevLett.80.1018 (1998).

7 Appendix

7.1 Chapter 3 Supporting Information

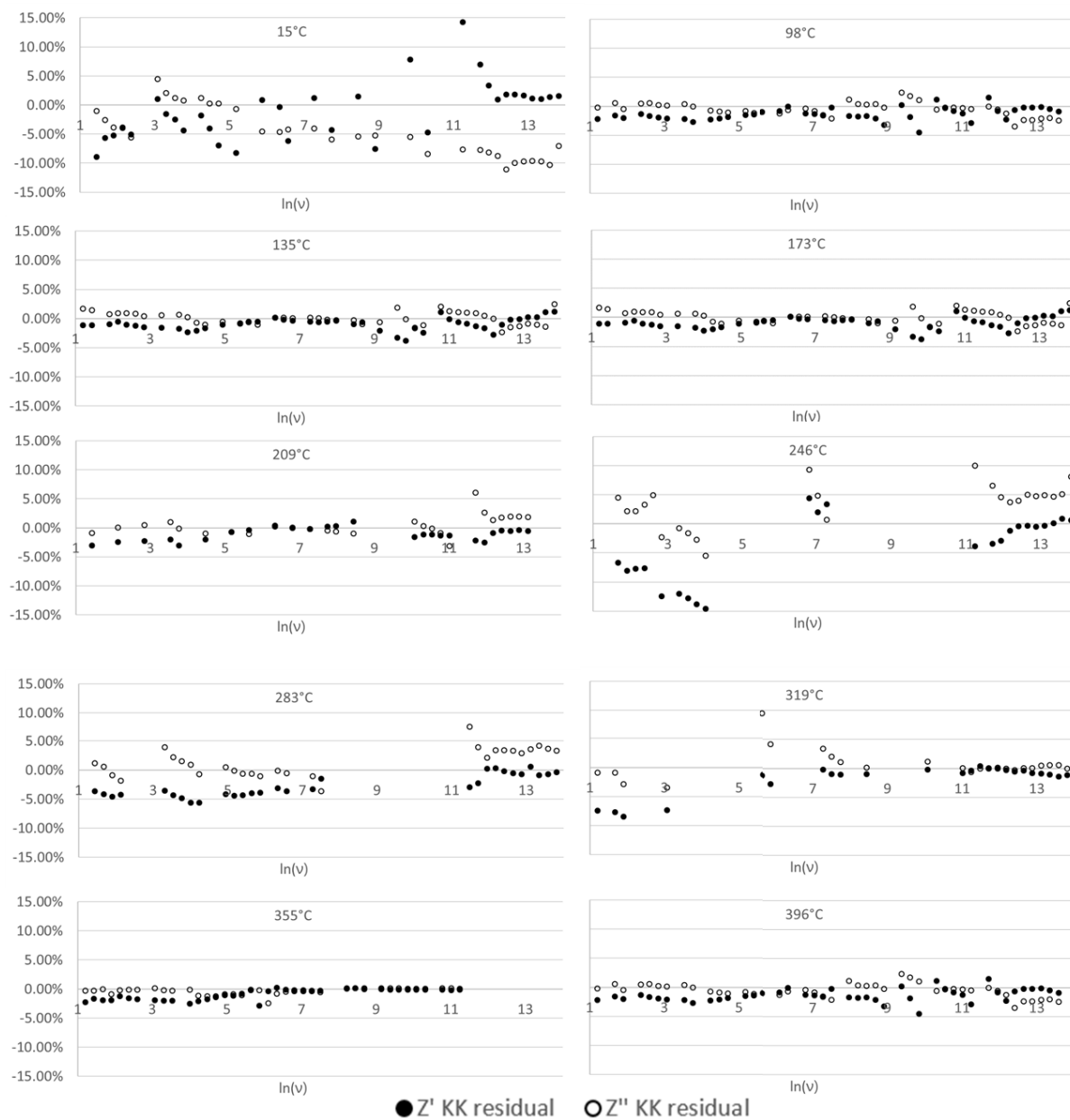


Fig. S 7.1 Kramers-Kronig test for all temperatures measured of the $x_{Ga} = 0.18$ film. Some data ranges were deleted as the measured impedance appeared to remain constant as frequency was changed.

Arrhenius Plot Fitting Methods

The general expression for the conductivity

$$\sigma = \epsilon_0 \epsilon_s / \int_0^\infty C(t) dt \quad (1)$$

The relaxation function $C(t)$ for the model with two activation energies is taken as a statistical average of two independent relaxation processes $C(t) = f \exp\left[-\left(\frac{t}{\tau_1}\right)\right] + (1 - f) \exp\left[-\left(\frac{t}{\tau_2}\right)\right]$. The relaxation times are $\tau_1 = \omega_{\infty 1}^{-1} \exp\left(\frac{E_1}{kT}\right)$ and $\tau_2 = \omega_{\infty 2}^{-1} \exp\left(\frac{E_2}{kT}\right)$, where f (and $1-f$) are the statistical weights proportional to the multiplicity of the site, or volume fraction, with the corresponding activation energy. $\omega_{\infty 1}$ and $\omega_{\infty 2}$ are the jump-attempt frequencies and must be both of the order of the lattice vibrations (normally $\sim 10^{15}$ Hz). ϵ_s is the lattice relative permittivity. The fit for the composition with 0.14 Ga gives us activation energies $E_1 = 0.66(3)$ eV and $E_2 = 0.38(3)$ eV but the ratio $\frac{f \omega_{\infty 2}}{(1-f) \omega_{\infty 1}} = 1.2(8) \times 10^4$ would result in an impossibly large value, far above the logical range of 1 order of magnitude difference. One can also verify that the temperature dependence of the two relaxation times does not agree with that of the impedance or electric modulus plot. Such inconsistencies have been discussed in the past and may be resolved if one takes ion-ion correlations into account. Therefore, we fit our data with a model which takes ion-ion correlation into account. The relaxation function takes a simple exponential form for $t < t_c$ with a decay time $\tau_0 = \omega_{\infty}^{-1} \exp(E_a/kT)$ and after the characteristic correlation time, t_c , $C(t)$ becomes a stretched exponential $C(t) = \exp\left[-\frac{t_c}{(1-n)\tau_0} \left(\left(\frac{t}{t_c}\right)^{1-n} - n\right)\right]$, with $0 \leq n < 1$. The effective activation energy resulting from the evaluation of equation (1) with $C(t)$ exhibits a crossover from its high-temperature value, E_a , determined by the lattice energy barriers to a larger low-temperature value, $E_a/(1 - n)$. This dependence reduces to a standard Arrhenius behavior when the correlation exponents vanishes $n = 0$ and its universality, and accuracy, has been demonstrated in the past *via* cross testing with experiments that do not involve impedance analysis.¹⁶⁰⁻¹⁶²

The model which considers ion-ion correlation gives $E_a = 0.35 \pm 0.02$ eV and a correlation exponent $n = 0.44 \pm 0.02$. For ionic conductors n has been generally found between 0.27 and 0.6.¹⁶³ The temperature dependence of the “effective” activation energy is shown in Fig. S7.2. The remaining important parameter from the fit, the product of the jump-attempt frequency and the correlation time, is $\omega_{\infty} t_c \approx 10^4$, also consistent with literature data for the correlation time of several picoseconds.

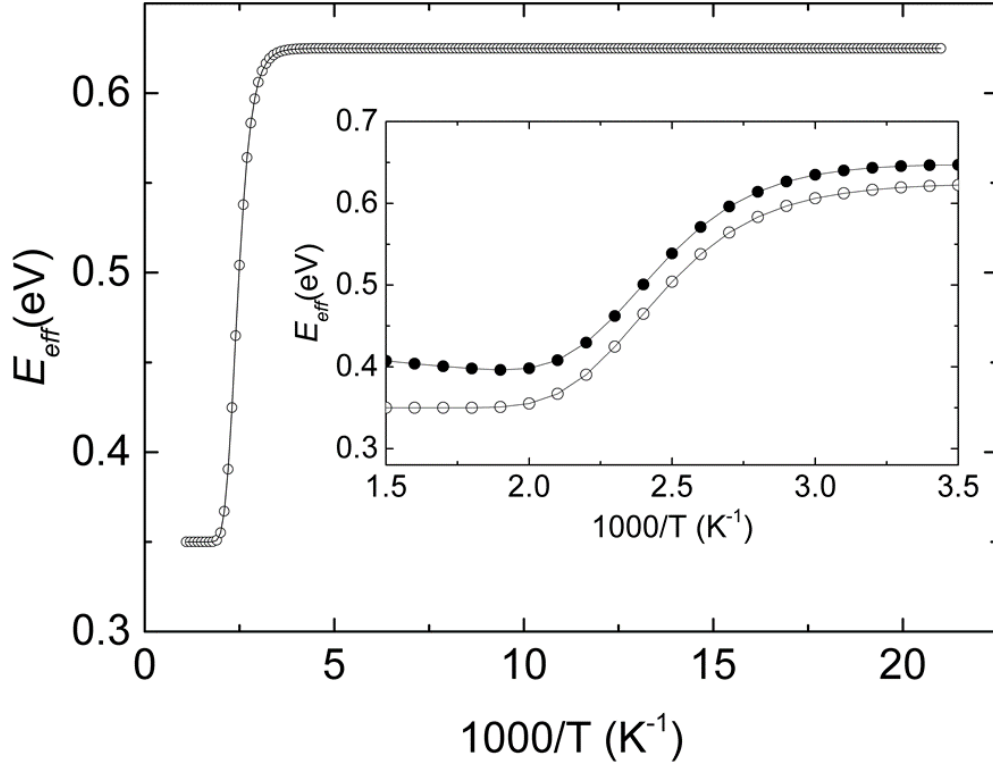


Fig. S 7.2 T-dependence of the effective activation energy, $E_{eff} = -k d \ln(\sigma) / d(1/T)$, calculated from the fit with Eq.1 for the film with 0.14 Ga. The plot has been extrapolated to low (50 K) and high (666 K) temperatures. The inset shows the range accessed in our measurements. The high temperature limit of $E_{eff} = E_a = 0.35$ eV is reached at about 530 K. The dotted line shows the apparent activation energy with the choice of y-axis in Figure 3.15.

7.2 Chapter 4 Supporting Information

N ₂ /Ar ratio	Element	Atomic. Number	Net	Mass (%)	Mass Norm. (%)	Atomic (%)	Abs. error (%)	Rel. error (%)
1.50	Nitrogen	7	42815	19.24	18.28	40.01	2.32	12.06
	Oxygen	8	15432	5.48	5.20	9.97	0.75	13.68
	Sodium	11	2789	0.61	0.57	0.77	0.07	10.75
	Silicon	14	26892	5.18	4.92	5.38	0.24	4.63
	Chromium	24	64405	73.51	69.84	41.17	2.78	3.78
	Carbon	6	2014	1.00	0.95	2.42	0.21	21.42
	Magnesium	12	1281	0.22	0.21	0.27	0.04	17.77
	Aluminium	13	138	0.02	0.02	0.02	0.00	11.21
			Sum	105.26	100.00	100.00		
1.35	Nitrogen	7	33793	18.34	17.79	39.65	2.26	12.31
	Oxygen	8	11318	4.84	4.69	9.16	0.69	14.28
	Sodium	11	1648	0.47	0.45	0.61	0.06	12.41
	Silicon	14	17464	4.60	4.46	4.96	0.22	4.74
	Chromium	24	53197	73.58	71.38	42.85	2.79	3.79
	Carbon	6	1605	0.95	0.92	2.40	0.22	22.61
	Magnesium	12	895	0.20	0.20	0.26	0.04	19.16
	Aluminium	13	460	0.10	0.09	0.11	0.03	33.38
			Sum	103.08	100.00	100.00		
1.22	Nitrogen	7	33415	16.88	16.44	37.82	2.08	12.34
	Oxygen	8	11383	4.41	4.30	8.65	0.63	14.32
	Sodium	11	1674	0.46	0.45	0.63	0.06	12.43
	Silicon	14	16509	4.12	4.02	4.61	0.20	4.81
	Chromium	24	58872	75.74	73.74	45.71	2.87	3.79
	Magnesium	12	748	0.16	0.16	0.21	0.04	22.79
	Carbon	6	1620	0.89	0.87	2.34	0.20	22.73
	Aluminium	13	156	0.03	0.03	0.04	0.00	10.72
			Sum	102.71	100.00	100.00		
1.11	Nitrogen	7	39105	16.20	15.61	36.60	1.97	12.18
	Oxygen	8	16235	5.12	4.93	10.12	0.70	13.63
	Sodium	11	2534	0.56	0.54	0.77	0.06	11.13
	Silicon	14	24053	4.87	4.69	5.48	0.23	4.68
	Chromium	24	71261	76.37	73.59	46.47	2.89	3.78
	Magnesium	12	1273	0.22	0.21	0.29	0.04	17.87
	Aluminium	13	510	0.08	0.08	0.10	0.03	38.01
	Copper	29	637	0.36	0.35	0.18	0.12	32.82
			Sum	103.78	100.00	100.00		
0.82	Nitrogen	7	36722	13.93	13.51	33.46	1.71	12.27
	Oxygen	8	14033	3.85	3.73	8.10	0.54	14.03
	Sodium	11	857	0.17	0.16	0.25	0.04	22.54
	Silicon	14	16707	3.19	3.09	3.82	0.16	4.99
	Chromium	24	83468	80.59	78.18	52.15	3.04	3.77
	Copper	29	975	0.51	0.49	0.27	0.14	27.75
	Magnesium	12	931	0.15	0.14	0.21	0.04	23.64
	Aluminium	13	903	0.14	0.14	0.17	0.03	24.23
	Carbon	6	1350	0.56	0.55	1.58	0.14	25.32

			Sum	103.09	100.00	100.00		
0.66	Nitrogen	7	29381	12.19	11.74	30.76	1.53	12.54
	Silicon	14	8880	1.64	1.58	2.06	0.10	5.85
	Chromium	24	80302	86.18	83.01	58.57	3.25	3.77
	Oxygen	8	11414	3.32	3.20	7.33	0.48	14.50
	Carbon	6	816	0.37	0.36	1.09	0.11	30.73
	Sodium	11	554	0.11	0.11	0.18	0.03	30.44
			Sum	103.82	100.00	100.00		
0.60	Nitrogen	7	30319	10.95	10.75	28.70	1.37	12.53
	Silicon	14	10259	1.73	1.70	2.26	0.10	5.74
	Chromium	24	92638	85.00	83.40	60.01	3.20	3.77
	Oxygen	8	13007	3.09	3.04	7.10	0.44	14.32
	Copper	29	1189	0.60	0.59	0.35	0.15	25.76
	Carbon	6	1253	0.50	0.49	1.52	0.13	26.34
	Aluminium	13	388	0.05	0.05	0.07	0.03	56.56
	Magnesium	12	0	0.00	0.00	0.00	0.00	3.05
			Sum	101.92	100.00	100.00		

Table S 7.1 Quantification values of the different Cr_xN samples from the EDX spectra. The penetration depth of the electrons is larger than the Cr_xN films, therefore we observe aluminum, sodium, magnesium and silicon signals which originate from the soda lime glass used as substrate.

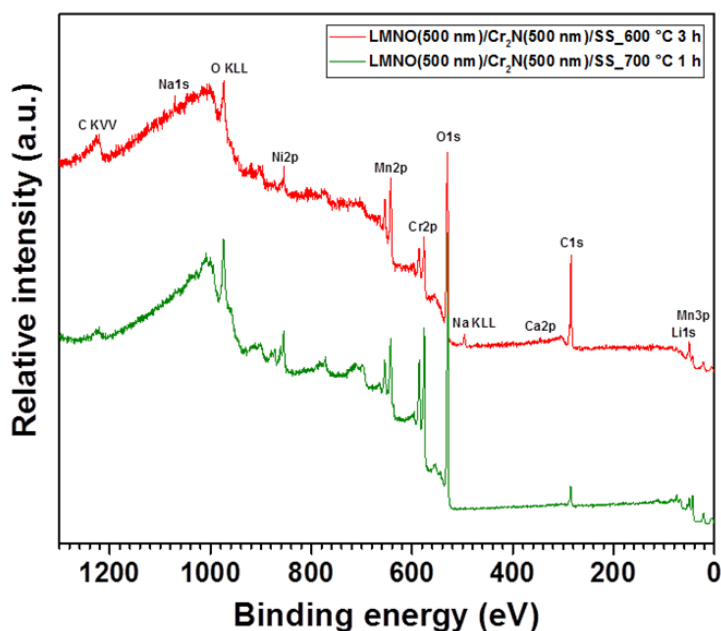


Fig. S 7.3 XPS surveys of the samples LMNO(500 nm)/ Cr_2N (500 nm)/SS annealed at 600 °C for 3 hours and annealed at 700 °C 1 hour. Note that the Na and Ca signals originally present in the survey of sample LMNO(500 nm)/ Cr_2N (500 nm)/Si at 600 °C are from to impurities in the sputtering target which decreased with target usage.

7.3 Financial Support

The research conducted in this PhD project was carried out at the Laboratory for Thin Films and Photovoltaics in EMPA within the framework of the project: Proposal 911 “SLIB – All Solid-state Li^+ Ion Batteries based on New Ceramic Li^+ Ion Electrolytes” funded by the Competence Centre for Energy and Mobility (CCEM) and Swiss Electric Research. Funding from the Swiss Federal Commission for Technology and Innovation (CTI) through the CTI Swiss Competence Centers for Energy Research (SCCER, “Heat and Electricity Storage”) is also kindly acknowledged

7.4 List of Figures

7.4.1 Key Figures

Fig. 1.1 Schematic of a typical battery with liquid electrolyte.....	11
Fig. 1.2 Schematic of an all-solid-state thin film cell with planar geometry	13
Fig. 1.3 Crystal structures of the 4 common crystal structures present in intercalation cathode materials. a) layered (LiCoO_2), b) spinel (LiMn_2O_4), c) olivine (LiFePO_4), and d) tavorite (LiFeSO_4F). Image reproduced from Islam et. al. ³³	14
Fig. 1.4 a comparison of solid Li^+ ion conductors in terms of a) ionic conductivity with groups determined by crystal structure from work by Bachman et. al. ⁸ and b) electrochemical stability with groups determined by anion reproduced from work by Richards et. al. ⁴⁸	16
Fig. 1.5 crystal structure of a) cubic $\text{Li}_7\text{La}_3\text{Zr}_2\text{O}_{12}$ and b) tetragonal $\text{Li}_7\text{La}_3\text{Zr}_2\text{O}_{12}$ including Li^+ site co-ordinations with O^{2-} ions colored in red. Blue octahedra represent Zr units and grey polyhedra represent La units. Diagrams taken from work by Awaka et. al. in ref. 7(left) and 8(right).....	17
Fig. 2.1 XRD pattern of the sol-gel synthesized pellet with reference data for cubic phase $\text{Li}_7\text{La}_3\text{Zr}_2\text{O}_{12}$: ICSD No. 422259. All thin films were deposited from this pellet via PLD.	23
Fig. 2.2 Schematic of thin film annealing setup. The Al_2O_3 capsule is shown partly transparent to reveal the Li source powder and thin film inside.	23
Fig. 2.3 An as-deposited $\text{Li}_7\text{La}_3\text{Zr}_2\text{O}_{12}$ based thin film deposited on a single crystal MgO substrate at 50 °C by PLD (a) top view SEM micrograph and (b) cross-sectional SEM micrograph. (c) XRD pattern of amorphous thin film structure and comparison to reference $\text{Li}_7\text{La}_3\text{Zr}_2\text{O}_{12}$ cubic structure.	25
Fig. 2.4 SEM micrographs of $\text{Li}_7\text{La}_3\text{Zr}_2\text{O}_{12}$ thin film series of increasing thickness (a) 90 nm (b) 110 nm (c) 130 nm (d) 380 nm. Accompanying schematics combine information from Fig. 3.3 and 3.4 to show the progression of phase and morphology as the thickness is increased. All films are deposited on MgO and post annealed with the lithium treatment.....	26
Fig. 2.5 XRD of $\text{Li}_7\text{La}_3\text{Zr}_2\text{O}_{12}$ film series of increasing thickness. Miller indices are of the c- $\text{Li}_7\text{La}_3\text{Zr}_2\text{O}_{12}$ phase. Other symbols denote impurity phases present in the films.	27

Fig. 2.6 (a) Electrochemical impedance spectroscopy measured at 240 °C and an inset at 450 °C for 380 nm lithium post treated film. (b) Arrhenius type plot of 380 nm films with activation energies included. References are provided for comparison. (c) Circuit model used to describe the trend seen in the Arrhenius plot. 2 RC elements which could represent the oxygen ion conductivity of the $\text{La}_2\text{Zr}_2\text{O}_7$ phase and the lithium ion conductivity in the $\text{Li}_7\text{La}_3\text{Zr}_2\text{O}_{12}$.	29
Fig. 3.1 Schematic of method for forming thin film gallium doped LLZO based on multilayer co-sputtering and a post-annealing process.	33
Fig. 3.2 Grazing incidence XRD of typical as-deposited thin films of LLZO and LLZO co-sputtered with Li_2O . Incidence angle $\omega = 1^\circ$. A broad reflection is observed between 2θ of 25° - 35° for both films.	35
Fig. 3.3 a) XRD of LLZO film with no additions after annealing at 700°C compared to film co-sputtered with Li_2O XRDs at 700°C in-situ and then post-annealing. Reference patterns for cubic and tetragonal LLZO are from the ICSD database, (ICSD 422259) and (ICSD 246817) respectively. b) Phase evolution of co-sputtered film LLZO + Li_2O showing transition from tetragonal LLZO to cubic LLZO at 600°C . To the right is the temperature-time profile of the annealing process with phase annotations. The ramp rate for heating/cooling was $5^\circ\text{C} / \text{min}$.	37
Fig. 3.4 XRD LLZO + Li_2O co-sputtered film at 300°C . Two possible matches are Zr_3O and $\text{Li}_4\text{Zr}_3\text{O}_8$, however there is a high degree of uncertainty.	38
Fig. 3.5 Phase evolution of films with Ga concentrations of a) 0.20 Ga b) 0.18 Ga c) 0.16 Ga d) 0.14 Ga with annotated temperature profiles to the right. All films crystallize into the cubic phase at $> 600^\circ\text{C}$. The star symbol is to label precursor phases with tentative assignment to ZrO_2 .	41
Fig. 3.6 XRD segments from intensity contour plot of film with 0.20 Ga showing the development of the LLZO phase over the course of the in-situ annealing.	41
Fig. 3.7 RT XRD of thin films after thermal treatment with varying contents of Ga and Li. Reference patterns for cubic and tetragonal LLZO are from the ICSD database, (ICSD 422259) and (ICSD 246817) respectively.	42
Fig. 3.8 top view and cross-section SEM of the films $x_{\text{Ga}} =$ a) 0.2 b) 0.81 c) 0.16 d) 0.14. Cross-sections are obtained from freshly cleaved edges.	43
Fig. 3.9 Depth profile of respective peak intensities for $x_{\text{Ga}} = 0.14 - 0.20$ films for each element from XPS measurements. Due to the low yield of $\text{Li}1s$ signal, the intensity has been increased by factor x10 for clearer observation. The dotted lines indicate at which point the detailed XPS analyses and quantification was carried out.	44
Fig. 3.10 XPS spectra of Ga 2p and Li 1s orbitals for gallium doped samples. Two bonding environments are observed for both elements indicating the presence of a second phase in the thin films. The outlier point in the $\text{Li}1s$ spectrum in a) is later removed for an improved fit as described in Table S7.1.	45
Fig. 3.11 XPS spectra of $\text{La}3d$, $\text{O}1s$ and $\text{Zr}3d$ orbitals for gallium doped samples. The bonding environments do not change significantly for these elements as the gallium	

concentration is altered. The La 3d peak was fitted by 3 doublets with fixed FWHM and distance. ⁷ However intensities of components were left free, as they vary depending on the hybridization of the orbitals ⁸ and chemical composition of the La compound. ^{9,10} The energy position of the first La3d doublet is 835.2 eV. Zr3d was fit with the doublet, peak at lower BE is at 182.7 eV.....	46
Fig. 3.12 Trends in atomic percent of 2 chemical states (violet - lower BE, blue - higher BE) of Li 1s and Ga 2p across 4 samples. A correlation is observed between both lower BE states and both higher BE states allowing these states to be assigned to the same phases.	47
Fig. 3.13 Conductivity measurements for film with 0.18 Ga over the course of three heating and cooling cycles. Conductivities were calculated via. R-CPE circuit fitting.....	48
Fig. 3.14 Arrhenius plot of $x_{\text{Ga}} = 0.18$ film ionic conductivity from impedance and electric modulus analysis presented in Fig. 3.13.	50
Fig. 3.15) Nyquist plot for electrochemical impedance spectroscopy (EIS) measured at 50°C for LLZO film with 0.14 Ga resulting in a conductivity of $1.6 \times 10^{-5} \text{ S cm}^{-1}$. An R-CPE equivalent circuit model is used to fit the data. b) Plot of the complex electric modulus of the same film with key variables for calculating ionic conductivity labelled.....	50
Fig. 3.16 Arrhenius type plot for LLZO films with 0.20, 0.18, 0.16 and 0.14 Ga concentrations. Initial high conductivity measurement of 0.14 Ga film shown in Fig. 6a plotted as a single point. Other reference data for thin film LLZO from literature were Kim et. al. ⁹⁶ , Rawlence et. al. ⁹⁸ , Park et. al. ⁹⁹ , Kalita et. al. ¹⁰¹ , Tadanaga et. al. ¹⁰³ and Chen et. al. ¹⁰⁴ . Howard et. al. ¹³⁵ shows data obtained from a pellet of LLZO doped with 0.5 Ga per unit cell.	51
Fig. 4.1 Scheme of the coin cells assembly used in this work	55
Fig. 4.2 Cr_xN thin film thickness determined by SEM (Fig. 4.4) as a function of the N_2/Ar ratio.....	56
Fig. 4.3 Approximate composition (x) and resistivity of Cr_xN films on soda lime glass as function of Ar/N_2 ratio in the sputtering gas.	56
Fig. 4.4 X-ray diffractograms of Cr_xN thin films exhibiting different estimated Cr/N ratios prepared at 300 °C by pulsed DC magnetron sputtering.....	57
Fig. 4.5 Relative peaks intensities of as-prepared $\text{Cr}_{2.1}\text{N}$ (top) and the Cr_2N pattern.....	58
Fig. 4.6 SEM cross sections of Cr_xN thin films on Si(100).	59
Fig. 4.7 SEM images of Cr_xN thin films with 3 different N_2 contents prepared at 300 °C by pulsed DC magnetron sputtering, showing the surface roughness of the as-prepared samples, normal views (a–c), and their columnar morphology, cross sections in (d).	59
Fig. 4.8 SEM normal views of Cr_xN thin films showing the change in surface microstructure for CrN - $\text{Cr}_{2.1}\text{N}$ (the scale is the same for all images).....	60
Fig. 4.9 a) Evolution of $\text{Cr}_{2.1}\text{N}$ sheet resistance with thickness. b)-d) SEM micrographs of a 45 nm thick $\text{Cr}_{2.1}\text{N}$ film.	61
Fig. 4.10 SEM cross sections of $\text{Cr}_{2.1}\text{N}$ with different thicknesses.....	61

Fig. 4.11 SEM normal views of $\text{Cr}_{2.1}\text{N}$ with different thicknesses showing the change in surface microstructure. A 260 nm thick CrN film has been included for comparison.....	62
Fig. 4.12 Electrochemical performance of $\text{Cr}_2\text{N}/\text{Al}$ ~500 nm thick CC in comparison with aluminum foil. (a) CVs of bare Al foil between 2–5 V vs. Li^+/Li . (b) CVs of $\text{Cr}_2\text{N}/\text{Al}$ CC between 2–5 V vs. Li^+/Li	64
Fig. 4.13 SEM normal view of as-prepared LMNO(500 nm) on $\text{Cr}_2\text{N}(500 \text{ nm})/\text{Si}$ (a) and its cross section (b). c) GIXRD of as-prepared LMNO(500 nm)/ $\text{Cr}_2\text{N}(500 \text{ nm})/\text{SS}$ at $\omega = 1^\circ$	65
Fig. 4.14 SEM normal views of LMNO(500 nm)/ $\text{Cr}_2\text{N}(500 \text{ nm})/\text{SS}$ for the as-prepared (top), 600 °C 3 h (middle) and 700 °C 1h (bottom left) cases. Upon annealing, the surface of the samples develop crystals. The size depends on the annealing temperature, observing the largest crystal for the 700 °C 1 hour treatment, which may be attributed to the large surface segregation of chromium (bottom right).	66
Fig. 4.15 (a) GIXRD of annealed LMNO(500 nm)/ $\text{Cr}_2\text{N}(500 \text{ nm})/\text{SS}$ at grazing angles (ω) 1° and 5° ; the green dashed lines indicate the Cr_2N peaks. (b) SEM cross section of LMNO(500 nm)/ $\text{Cr}_2\text{N}(500 \text{ nm})/\text{SS}$. (c) Atomic ratios calculated from XPS sputter-depth profiles for LMNO(500 nm)/ $\text{Cr}_2\text{N}(500 \text{ nm})/\text{SS}$, the dashed line represents the LMNO surface and the dashed rectangle depicts the interface region between LMNO cathode material and Cr_2N current collector. The thermal treatment was in all cases 600 °C for 3 hours.	68
Fig. 4.16 XPS peaks for several elements in the sputter-depth profile of LMNO(500 nm)/ $\text{Cr}_2\text{N}(500 \text{ nm})/\text{SS}$, annealed at 600 °C for 3 hours.	70
Fig. 4.17 XPS peaks for several elements in the sputter-depth profile of LMNO(500 nm)/ $\text{Cr}_2\text{N}(500 \text{ nm})/\text{SS}$, annealed at 700 °C for 1 hour.	71
Fig. 4.18 Mn/Cr, Mn/Ni and N/Cr atomic ratios for LMNO(500 nm)/ $\text{Cr}_2\text{N}(500 \text{ nm})/\text{SS}$ after annealing at 700 °C 1 hour.	71
Fig. 4.19a) Schematic of the multilayer and contacts used for EIS. b) Nyquist plot at room temperature of LMNO(500 nm)/ $\text{Cr}_2\text{N}(500 \text{ nm})/\text{Si}$ after annealing at 600°C 3 hours. Frequency range from 1MHz to 10 mHz. The fit of the data is shown in red. The inset depicts the equivalent circuit used to fit the data, consisting of resistors and constant phase elements.	72
Fig. 4.20 Electrochemical performance of LMNO on Cr_2N current collectors. (a) CV of LMNO annealed at 600 °C for 3 hours and then measured between 3–5 V vs. Li^+/Li . (b) Galvanostatic charge and discharge curves of LMNO annealed at 600 °C for 3 hours. (c) Cycling behavior of LMNO annealed at 600 °C for 3 hours and 700 °C for 1 hour measured at different C rates.	74

7.4.2 Supplementary Figures

Fig. S 7.1 Kramers-Kronig test for all temperatures measured of the $x_{\text{Ga}} = 0.18$ film. Some data ranges were deleted as the measured impedance appeared to remain constant as frequency was changed. 89

Fig. S 7.2 T-dependence of the effective activation energy, $E_{\text{eff}} = -k d \ln(\sigma) / d(1/T)$, calculated from the fit with Eq.1 for the film with 0.14 Ga. The plot has been extrapolated to low (50 K) and high (666 K) temperatures. The inset shows the range accessed in our measurements. The high temperature limit of $E_{\text{eff}} = E_a = 0.35 \text{ eV}$ is reached at about 530 K. The dotted line shows the apparent activation energy with the choice of y-axis in Figure 3.15. 91

Fig. S 7.3 XPS surveys of the samples LMNO(500 nm)/Cr₂N(500 nm)/SS annealed at 600 °C for 3 hours and annealed at 700 °C 1 hour. Note that the Na and Ca signals originally present in the survey of sample LMNO(500 nm)/Cr₂N(500 nm)/Si at 600 °C are from to impurities in the sputtering target which decreased with target usage. 93

7.5 List of Tables

Table 3.1 Relative elemental concentrations as calculated by XPS for each sample with nominal Ga contents between 0.20 - 0.14. Values are normalized around La content, which is set to 3 for each sample for comparison to the expected formula: Li₇La₃Zr₂O₁₂. *Removing the outlier over the Li1s peaks in Fig. 3.9a results in lower lithium values for both BEs. 45

Table S 7.1 Quantification values of the different Cr_xN samples from the EDX spectra. The penetration depth of the electrons is larger than the Cr_xN films, therefore we observe aluminum, sodium, magnesium and silicon signals which originate from the soda lime glass used as substrate. 93

7.6 Nomenclature

a:	cross-sectional area of thin film
BE:	binding energy
C:	battery discharge rate
C ₀ :	geometric capacitance
C(t):	relaxation function
CAS:	chemical abstracts service
CCEM:	competence center for energy and mobility
CPE:	constant phase element (in circuit model)
CTI:	Swiss federal commission for technology and innovation
CV:	cyclic voltammetry
D-MATL:	Department of Materials ETH Zürich
d:	distance between contacts

DC:	direct current
E _a :	activation energy
EDX:	energy dispersive x-ray spectroscopy
EIS:	electrochemical impedance spectroscopy
ERDA:	elastic recoil detection analysis
f:	statistical weight proportional to lattice site multiplicity
FWHM:	full width at half maximum
GIXRD:	grazing incidence X-ray diffraction
ICP-OES:	inductively coupled plasma - optical emission spectroscopy
ICSD:	inorganic crystal structures database
j:	$\sqrt{-1}$
JCPDS:	joint committee on powder diffraction standards
k:	Boltzmann constant
LCO:	LiCoO ₂
LCP:	LiCoPO ₄
LTO:	Li ₄ Ti ₅ O ₁₂
LLZO:	Li ₇ La ₃ Zr ₂ O ₁₂
c-LLZO:	cubic phase LLZO
t-LLZO:	tetragonal phase LLZO
Al:LLZO:	Al doped LLZO
Ga:LLZO:	Ga doped LLZO
LMNO:	LiMn _{1.5} Ni _{0.5} O ₄
LZO:	La ₂ Zr ₂ O ₇
M*:	complex electric modulus
M'	real component of electric modulus
M''	imaginary component of electric modulus
MOCVD:	metal-organic chemical vapour deposition
NCA:	LiNi _{0.8} Co _{0.15} Al _{0.05} O ₂
NMC:	LiNi _{0.33} Co _{0.33} Mn _{0.33} O ₂
NRA:	nuclear reaction analysis
PLD:	pulsed laser deposition
Raman:	Raman spectroscopy
R:	resistor (in circuit model)
RF:	radio frequency
RT:	room temperature
SCCER:	Swiss competence center for energy research
SEM:	scanning electron microscopy
sh:	sheet resistance
SS:	stainless steel
t:	time
t _c :	characteristic correlation time
th:	film thickness
XPS:	X-ray photoelectron spectroscopy
XRD:	X-ray diffraction

Z^* :	complex impedance
Z' :	real component of impedance
Z'' :	imaginary component of impedance
ϵ^* :	complex permittivity
ϵ/ϵ' :	real component of permittivity
ϵ'' :	imaginary component of permittivity
ϵ_0 :	permittivity of free space
ϵ_s :	lattice relative permittivity
ν :	frequency
σ :	electrical conductivity
τ :	relaxation time
ω :	angular frequency
ω_∞ :	jump attempt frequency for Li ion

7.7 Publications

1. Rawlence, M.; Garbayo, I.; Buecheler S.; Rupp, J.L.M. “On the chemical stability of post lithiated garnet Al-stabilized $\text{Li}_7\text{La}_3\text{Zr}_2\text{O}_{12}$ solid-state electrolyte thin film”, *Nanoscale*, **8**, 14746-14753 (2016) DOI: [10.1039/c6nr04162k](https://doi.org/10.1039/c6nr04162k)
2. Rawlence, M.; Filippin, A. N.; Wäckerlin, A.; Ling, T.-Y.; Cuervo-Reyes, E.; Remhof, A.; Battaglia, C.; Rupp, J.L.M., Buecheler S. “The Effect of Gallium Substitution on Lithium Ion Conductivity and Phase Evolution in Sputtered $\text{Li}_{7-3x}\text{Ga}_x\text{La}_3\text{Zr}_2\text{O}_{12}$ Thin Films”, *ACS Applied Materials & Interfaces*, **10**, (16), 13720-13728 (2018) DOI: [10.1021/acsami.8b03163](https://doi.org/10.1021/acsami.8b03163)
3. Filippin, A. N.‡; Rawlence, M.‡; Wäckerlin, A.; Feurer, T.; Zünd, T.; Kravchyk, K.; Kovalenko, M. V.; Romanyuk, Y. E.; Tiwari, A. N.; Buecheler S., “Chromium nitride as a stable cathode current collector for all-solid-state thin film Li-ion batteries” *RSC Advances*, **7**, 26960-26967 (2016) DOI: [10.1039/c7ra03580b](https://doi.org/10.1039/c7ra03580b)

‡ signifies co-first author

7.8 Patents

- Rawlence, M.; Filippin, A.; Buecheler, S., “Li-ion based electrochemical energy storage cell”, Patent application EP16200316 (pending)

7.9 Conference Contributions

- Nicolas Filippin, M. Rawlence, A. Wäckerlin, Y. E. Romanyuk, S. Buecheler
"On the interface and role of interlayers between high voltage cathode LMNO and solid-state electrolyte LLZO"
Oral Presentation at Materials Research Society (MRS), Phoenix, USA, April 2017
- M. Rawlence, A. Nicolas Filippin, A. Remhof, J. L. M. Rupp, S. Buecheler
"The Effect of Lithium and Gallium Concentration on Phase Evolution in Lithium Ion Conducting Garnet $\text{Li}_{7-3x}\text{La}_3\text{Zr}_2\text{Ga}_x\text{O}_{12}$ Thin Films"
Poster Presentation at Bunsen Colloquium, Frankfurt, Germany, Nov 26th 2016.
- N. Filippin, M. Rawlence, T. Zünd, K. Kravchyk, M. Kovalenko Y. E. Romanyuk, S. Buecheler
"Highly stable current collector for Li-ion thin film batteries based on a Ni-Al superalloy"
Oral Presentation at Bunsen Colloquium, Frankfurt, Germany, Nov 26th 2016.
- M. Rawlence, M. Kubicek, J.L.M Rupp, S. Buecheler,
"Effect of Al Substitution on the Performance of $\text{Li}_7\text{La}_3\text{Zr}_2\text{O}_{12}$ Ceramic Electrolyte"
Poster Presentation at European Materials Research Society (E-MRS), Lille, France, May 26th 2014.
- M. Rawlence, M. Struzik, J.L.M Rupp, S. Buecheler
"Physical and Electronic characterization of $\text{Li}_7\text{La}_3\text{Zr}_2\text{O}_{12}$ Thin Films vs. Bulk"
Poster Presentation at Bunsen Colloquium, Frankfurt, Germany, Nov 26th 2014.
- J.L.M. Rupp, S. Afyon, I. Garbayo, M. Struzik, M. Rawlence, R. Pfenninger,
"All Solid-state Li-Garnet-based Batteries: From Materials Development to Thin Film Microstructures"
Poster Presentation at 20th International Conference on Solid-state Ionics (SSI), Colorado, U.S.A., June 15th 2015.
- M. Rawlence, I. Garbayo, J.L.M. Rupp, S. Buecheler,
"Solid-state $\text{Li}_7\text{La}_3\text{Zr}_2\text{O}_{12}$ Thin Film Electrolyte by Pulsed Laser Deposition: Deposition, Crystallization, and Near Order Characteristics vs. Lithiation"
Poster Presentation at 7th Lithium Battery Discussions, Arcachon, France, 21st June 2015.